えんが衛星によるブラックホール候補天体のエネルギースペクトルの研究

Spectral Study of Black Hole Candidates Observed with Ginga

Ken Ebisawa

Spectral study of black hole candidates observed with Ginga

Ken Ebisawa

A thesis submitted in partial fulfilment of
the requirements for the degree of
DOCTOR OF PHILOSOPHY (Astronomy)
at the
UNIVERSITY OF TOKYO
December 1990

Abstract

Energy spectra of five black hole candidates Cyg X-1, LMC X-3, LMC X-1, GX339–4 and GS2000+25 have been studied with the Large Area Proportional Counters (LAC) on board the *Ginga* satellite. It was found that all the observed energy spectra of these sources can be represented by a unified two component model, which is composed of a soft component and a hard component. The soft component is represented by a model spectrum expected from optically thick accretion disks which have a radially dependent multicolor structure. The derived maximum color temperature of the accretion disks was in the range of 0.4 – 1.2 keV. The hard component is represented by a power-law with a photon index of 1.7 – 2.5, modified by a broad edge-like structure over 7 – 20 keV. The ratio of the two spectral components was significantly variable; in some cases, the soft component disappeared, while in other cases, the hard component became too weak to be detected.

The intensity of the soft component is considered to reflect the mass accretion rate. The inner radius of the accretion disk determined by the fitting of the model spectrum was nearly constant for each source regardless of the mass accretion rate. It is proposed that the constant inner radius corresponds to the inner most radius of stable Keplerian orbits around a black hole, i.e., three times the Schwarzschild radius of the black hole. In this context, the derived inner radii of the accretion disks can be related to the masses of the compact objects of the sources. The mass of the compact object in LMC X-3 thus derived is consistent with the lower limit of the mass determined from the optical observations; for LMC X-1, GS2000+25 and GX339–4, the estimated masses are systematically greater than those of neutron star sources obtained with the same method.

The broad edge-like structure in the hard component was commonly found in all the sources. The lower end of this structure is always between 7 – 8 keV, which strongly suggests that the structure is related to the K-edge absorption of iron. A partial absorption model can reproduce the spectral shape of the broad edge-like structure, but this model is physically unrealistic since the resultant scattering optical depth of the absorbing matter significantly exceeds unity. Reflection of X-rays by optically thick matter is likely to explain the observed structure. However, for GS2000+25, lack of the expected fluorescence iron emission line still remains as a problem to be solved.

In the wide time scales from seconds to months, the hard component exhibited larger variations than the soft component did. A clear correlation was not found between the variations of the two components. Absence of a correlation suggests the existence of hidden parameters which control the variation of the hard component independently of the mass accretion rate.

To Mika

Contents

Chapter 1

Introduction

Most of the bright X-ray sources in our Galaxy are close binary systems consisting of normal stars and compact stars. The X-ray emission originates in gravitational potential energy released in the process of mass accretion from the normal stars onto the compact stars. Today, it is unquestionable that the compact stars in X-ray pulsars, X-ray bursters, and most low mass X-ray binaries are neutron stars. As a matter of fact, X-ray pulsars are rotating neutron stars with strong magnetic field, X-ray bursts are explosive thermonuclear reactions on the surfaces of neutron stars, and most low mass X-ray binaries are binaries consisting of weakly magnetized neutron stars and low mass companions.

It is well-known that there is a definite upper limit for the masses of neutron stars which are supported by neutron degenerate pressure and nuclear force. Nothing can sustain the strong self-gravitation of the compact objects whose masses are larger than the upper limit, so that such massive, compact objects have to keep gravitationally collapsing forever. They are called black holes. Since nothing, not even light can escape from the strong gravitational field of black holes, black holes can not be observed with electromagnetic waves. The only way to recognize black holes is through their gravitational interactions with their environments.

It has been shown from optical spectroscopic observations that the masses of the compact stars in Cyg X-1, LMC X-3 and A0620–00 are significantly larger than the upper limit for the mass of a neutron star. Therefore these compact stars are very likely to be black holes. It is very probable the mass of the compact

object in LMC X-1 also exceeds the upper limit.

Among these X-ray sources, Cyg X-1 has been extensively studied and its peculiar characteristics have been evident since the early days of X-ray astronomy. Although these peculiar characteristics may be directly related to the presence of a black hole, it is a controversial issue as to what are the unique X-ray properties peculiar to black holes. In any case, X-ray sources whose phenomenological characteristics are similar to those of Cyg X-1, including Cyg X-1 itself, are generally designated as black hole *candidates*. The above four sources with the mass evidence should be considered as convincing black hole candidates. Besides, there are several black hole candidates with less convincing evidence, represented by GX339–4, the masses of whose compact objects are unknown.

Black hole candidates have been prime targets in X-ray astronomy since its birth in 1962. A lot of workers have been tackling enigmas of black hole candidates by launching sounding rockets, balloons, and more than a dozen X-ray satellites. However, thus far, the X-ray properties of LMC X-3 and LMC X-1 have been poorly understood because of the large distance to these sources. Even for the bright sources, Cyg X-1 and GX339–4, instruments prior to those aboard *Ginga* were inadequate to investigate detailed spectral features and rapid spectral variations.

In this thesis, I present results of observations of five black hole candidates, Cyg X-1, LMC X-3, LMC X-1, GX339–4 and GS2000+25, with the Large Area Counter (LAC) on board the *Ginga* satellite. GS2000+25 is a transient source discovered by the All Sky Monitor (ASM) on board *Ginga*. I included it in the category of black hole candidates since its X-ray characteristics have been shown to be very similar to A0620–00. The main point of the thesis is to study the energy spectra and spectral variations of the black hole candidates, which I have been able to investigate in detail than ever before owing to the large area and the wide energy coverage of the LAC.

In chapter 2, I present a review of the current understanding of galactic binary X-ray sources with emphasis on black hole candidates, together with a brief historical review of X-ray astronomy. The *Ginga* satellite and the LAC are described in chapter 3. The observations of the black hole candidates with *Ginga* are explained in chapter 4. The method of data analysis and the results are presented in chapter 5. Finally in chapter 6, I discuss the present results in the context of mass accretion onto black holes.

Chapter 2

Reviews

In this chapter, after a brief historical review of X-ray astronomy, I present a general overview of galactic binary X-ray sources. Next, bright low mass X-ray binaries are briefly reviewed with emphasis on their energy spectra, since their X-ray properties are often similar to those of black hole candidates. Then I review the spectral characteristics of the black hole candidates, Cyg X-1, LMC X-3, LMC X-1, GX339–4 and GS2000+25, which are featured in this thesis, and A0620–00, which is a transient and has strong mass evidence for a black hole.

An outline of the relevant physics of neutron star models and the maximum mass of neutron stars is found in appendix A. Methods of determining the mass of the compact objects in X-ray binaries are explained in appendix B.

2.1 A Brief History of X-ray Astronomy

On June 18, 1962, with the launching of the Aerobee rocket carrying three Geiger counters, Giacconi *et al.* (1962) accidentally made the momentous discovery of the cosmic X-ray source Sco X-1. This was the birth of X-ray astronomy. With subsequent X-ray observations using sounding rockets and balloons, more than 30 X-ray sources, including the peculiar source Cyg X-1, were discovered by the end of the 1960's. The distribution of the sources along the Milky Way strongly suggested that they are situated in our Galaxy. A prescient model was proposed by Shklovskii (1967) for Sco X-1 that the X-ray emission originates in high temperature gas

flowing onto a neutron star from a close binary companion, though the reality of neutron stars was still uncertain at that time.

On December 12, 1970, the first X-ray astronomy satellite *Uhuru* (Swahili for *freedom*) was launched by NASA off the coast of Kenya. This satellite revolutionized our understanding of cosmic X-ray sources and compact objects. Among Uhuru's uncountable achievements, the discovery of X-ray pulsars was particularly crucial to understanding cosmic X-ray sources. The periodicities in X-rays were originally detected from Cen X-3 and soon after another X-ray pulsar, Her X-1, was discovered. The short periods, 4.8 sec for Cen X-3 and 1.24 sec for Her X-1, were interpreted as evidence that rotating neutron stars were the origin of the periodicity. The existence of neutron stars had been generally accepted by that time due to the discovery of a radio pulsar by Hewish *et al.* (1968) and the successful elucidation by Gold (1968) that radio pulsars are spinning neutron stars with strong magnetic fields not aligned with the spin axes. The doppler modulations of the pulse periods and the eclipses of X-rays by the companions was direct evidence that the neutron stars of the X-ray pulsars are part of binary systems. Thereby, the origins of major galactic X-ray sources are identified to be mass accreting neutron stars in binary systems.

After the triumph of the Uhuru experiment, approximately 10 satellites were entirely or partially devoted to X-ray astronomy during the 1970's. Precise positions of X-ray sources were determined during systematic surveys with the modulation collimators on board SAS-3 (Bradt *et al.* 1977) and HEAO-1 (Gursky *et al.* 1978). X-ray sources of an entirely new class, "X-ray bursters", were discovered by the ANS satellite (Grindlay *et al.* 1976). Soon after, X-ray bursts were identified as explosive thermonuclear reactions on the surfaces of neutron stars by extensive studies with subsequent satellites such as SAS-3 and *Hakucho*. From these studies during the decade, it became clear that there are several different classes of luminous galactic binary X-ray sources; X-ray pulsars, X-ray bursters, and non-pulsating, non-bursting X-ray sources. Some of the non-pulsating, non-bursting sources have been considered to be black hole candidates, the rest of them turned out to be binaries of weakly magnetized neutron stars and low mass companions; the latter are what we today call low mass X-ray binaries (LMXB). It also became clear that the X-ray properties of binary X-ray sources are closely related to the

properties of their optical companions.

The peculiar characters of Cyg X-1 have been evident since the early days in X-ray astronomy. The first suggestion that the compact object in Cyg X-1 could be a black hole was made by Oda *et al.* (1971) on the basis of its unusual rapid variability. Cyg X-1 was the first source found to be located in an optical binary system. The optical counter part was a 5.6-day single-line spectroscopic binary known as HDE226868, a 9th magnitude super giant star (Webster and Murdin 1972). Later, the mass of the compact object in Cyg X-1 was shown ($\gtrsim 9.5\ M_\odot$; Paczinskii 1974) to be conservatively larger than the upper limit for the masses of neutron stars ($\sim 2.5\ M_\odot$; see appendix A). Thereby the hypothesis that the compact object in Cyg X-1 was a black hole gained firm ground. Today, besides Cyg X-1, the compact objects in LMC X-3 ($M > 9.0 M_\odot$; Cowley *et al.* 1983; Paczyński 1983), A0620–00 ($M > 3.2 M_\odot$; McClintook and Remillard 1986), and LMC X-1 ($M > 2.5 M_\odot$; Hutchings *et al.* 1983) are confidently considered to be black holes on the basis of their large masses.

Most luminous galactic binary X-ray sources had been discovered by the end of 1970's. Since then, X-ray astronomy has matured and developed greatly owing to the great activities of *Einstein*, *Tenma*, *EXOSAT* and *Ginga*. The understanding of X-ray pulsars, X-ray bursters and bright low mass X-ray binaries has enormously advanced, as well as X-ray studies of dim galactic sources and extra galactic sources flourishing.

However, the enigma of black holes still remains unresolved. Besides the mass evidence of the compact objects, which is rather circumstantial, the direct observational evidence for the existence of black holes in X-ray binaries is still lacking. Thus they have been commonly designated as black hole *candidates*. It has not been elucidated yet why Cyg X-1 exhibits such unusual X-ray properties, or whether such properties are inherent to black holes or not. It has not been possible yet to diagnose GX339–4, whose X-ray characteristics are very similar to those of Cyg X-1, to be a black hole from its X-ray properties alone. It is required of X-ray astronomy to ascertain indisputable observational evidence of black holes, and to confirm the very existence of black holes in the black hole candidates.

2.2 An Overview of Binary X-ray Sources

2.2.1 Massive X-ray Binaries and Low Mass X-ray Binaries

Thus far, more than one hundred compact galactic X-ray sources have been optically identified. Except for compact sources in supernova remnants and binaries containing white dwarfs or non-degenerate stars, they are commonly classified into two categories; massive X-ray binaries (MXRBs or Class I) and low mass X-ray binaries (LMXBs or Class II), according to whether masses of the companion stars are larger, or smaller than about 2 $M_\odot$ (Bradt and McClintook 1983). In MXRBs, ratios of X-ray luminosities to optical luminosities ($L_X[2-11\,\mathrm{keV}]\,/\,L_{opt}[3000-7000\,\text{Å}]$) are in the range from 10^{-5} to 10, which arise from the high luminosity of the massive early-type companion stars; on the other hand in LMXBs, the ratios are primarily large ($10-10^4$), since sources of the optical lights are reprocessed X-rays by the accretion disks or surfaces of the companion stars. In three X-ray/optical novae, A0620-00 (Oke 1977), Cen X-4 (van Paradijs *et al.* 1980) and Aql X-1 (Thorstensen *et al.* 1978), the companion stars were directly observed when the X-ray emissions became quiet and identified as G7 - K3V stars.

MXRBs are widely distributed in the Galaxy (figure 2.1) and this fact together with the association of early-type stars indicate that the massive systems belong to the extreme Population I which consists of stars with ages younger than 10^8 years. The majority of MXRBs contain X-ray pulsars.

LMXBs are concentrated more towards the central region of the Galaxies than MXRBs (figure 2.1). Twelve low mass X-ray binaries are located in globular clusters. The spatial distribution, the late type companions, and the association with globular clusters suggest that LMXBs belong to Population II. However, there are some LMXBs whose companion stars are earlier than G type, and located in the galactic plane. Hence LMXBs are a mixture of old Population I and Population II objects. LMXBs are primarily associated with X-ray bursters and non-pulsating, non-bursting X-ray sources; only a few LMXBs are X-ray pulsars.

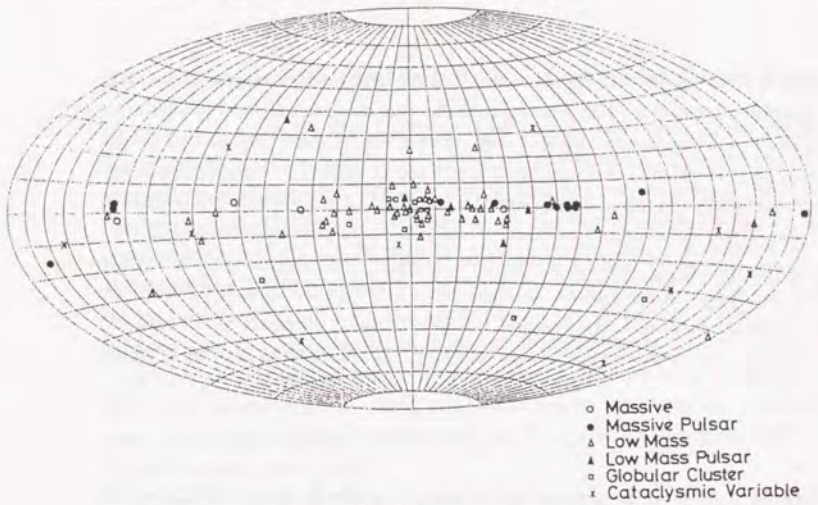

Figure 2.1: Distribution of bright galactic X-ray sources over the sky map in the galactic coordinate system. The figure is adopted from Hayakawa (1985).

The luminosity of a binary X-ray source is given by

$$L = \frac{G M \dot{M}}{R} = 1.3 \times 10^{37} \left(\frac{\dot{M}}{10^{17}\,\mathrm{g\,s^{-1}}}\right) \left(\frac{M}{M_\odot}\right) \left(\frac{R}{10\,\mathrm{km}}\right) \mathrm{erg\,s^{-1}}, \qquad (2.1)$$

where G is the gravitational constant, M and R are respectively the mass and the radius of the accreting star and $\dot{M}$ is the accretion rate. The upper limit of the luminosity is given by the Eddington limit

$$L_E = \frac{4\pi G M c}{\kappa} = 1.2 \times 10^{38} \left(\frac{M}{M_\odot}\right) \left(\frac{\kappa_T}{\kappa}\right) \left(\frac{2}{1+X}\right) \mathrm{erg\,s^{-1}}, \qquad (2.2)$$

where κ is the opacity of the stellar envelope, $\kappa_T = 0.4\,\mathrm{cm^2 g^{-1}}$ is the Thomson opacity, and X is the hydrogen mass fraction.

2.2.2 X-ray Pulsars

Thus far, 30 X-ray binary pulsars have been identified (see Nagase 1989 for a review). They are classified into three categories according to the nature of the

companion stars (Blair and Candy 1985; Nagase 1989); (A) binaries with early-type massive companions, (B) binaries with Be-star companions, and (C) binaries with low-mass companions. Most X-ray pulsars are in class (A) and (B), only Her X-1, 4U1626–67, GX1+4 and 4U2259+59 are in class (C). Some of the X-ray pulsars, especially those in class (B) are of a transient nature. The X-ray pulsars in the class (A) are divided into subclasses; (A-i) the short-period systems with very large X-ray luminosity and (A-ii) the long pulse-period systems with moderate X-ray luminosity. X-ray pulsars in class (A-i) and (C) are mostly powered by mass accretion via Roche-lobe overflow, whereas those in classes in (A-ii) and (B) are considered to be powered by mass accretion via stellar wind capture (Nagase 1989).

Neutron stars in X-ray pulsars have strong magnetic fields ($\sim 10^{12}$ G) at the surfaces, which guide the inflowing matter toward hot spots at the magnetic poles. The observed pulsations in X-rays are due to the non-alignment of the magnetic fields with the rotation axes of neutron stars. Since the magnetic fields of neutron stars are considered to decay with time scales of about 10^7 years (Lyne *et al.* 1985), it is reasonable that most X-ray pulsars are in MXRBs, which are young systems. The magnetic fields of X-ray pulsars are directly measured through cyclotron absorption features, which have been detected from Her X-1 (Trümper *et al.* 1978; Mihara *et al.* 1990), 4U0115+63 (Wheaton *et al.* 1979; Nagase *et al.* 1991), 4U1538–52(Clerk *et al.* 1990) and X0331+53 (V0332+53) (Makishima *et al.* 1990a). The values of the magnetic fields are all in the range $(1-3) \times 10^{12}$G.

The orbital parameters of eleven X-ray pulsars have been determined (Nagase 1989) thus far. Among them, masses of six neutron stars were estimated (Rappaport and Joss 1983), and later re-examined (Nagase 1989) with improved orbital parameters. Nagase (1989) concluded that the masses of individual neutron stars are likely to be in the range of from 1 $M_\odot$ to 1.8 $M_\odot$, and the most probable value of neutron star masses is close to 1.4 $M_\odot$(see appendix B and figure B.1).

2.2.3 X-ray Bursters and Bright Low Mass X-ray Binaries

In LMXBs [1], since the first Lagrange points are located close to the companion stars because of their small masses, matter is transferred via Roche-lobe overflow to neutron stars. Accretion disks will form around neutron stars since the inflowing matter posses sufficient angular momentum. In the accretion disks, the matter loses angular momentum by viscosity, thus gradually infalls inward, at last onto the neutron stars from the inner edges of the accretion disks. If the magnetic fields of the neutron stars are small enough, the accretion disks extend near to the neutron stars without being disrupted by the magnetic fields. The accreting matter is not collimated as in the case of X-ray pulsars, but rather lands uniformly on the surface of neutron stars so that X-ray pulsations are not observed. Gravitational potential energy is released and turned into X-rays in the accretion disks and on the surfaces of neutron stars.

There are about 35 X-ray sources which are known to exhibit X-ray bursts and all burst sources are LMXBs.[2] There are two kinds of X-ray bursts; type I, which show significant spectral softening during the decay, and type II, which do not (Hoffman, Marshall and Lewin 1978). Type II bursts have been observed only from the Rapid Burster (X1730–335), though it occasionally emits type I bursts. The X-ray spectrum of the decay phase of type I bursts are well fitted with a black body spectrum (Swank *et al.* 1977), with the effective radius being about 10 km for almost all the bursts regardless of the sources (van Paradijs 1978; Ohashi *et al.* 1982). The size coincides with a radius of a neutron star so that type I bursts have been considered to be phenomena on the surfaces of neutron stars.

Type I bursts are currently considered in terms of nuclear shell flashes on the surfaces of neutron stars (e.g. Joss and Rappaport 1984 for a review). The matter

[1] According to the original definition of LMXBs, X-ray pulsars and black hole candidates with low mass companions are included in the category of LMXBs. However, the term LMXBs is occasionally used to denote binaries of neutron stars and low mass companions. Hereafter, I use the term LMXBs in this sense.

[2] The extraordinary source Cir X-1, which exhibits X-ray bursts (Tennant *et al.* 1986), was originally considered to be a massive binary with an early-type supergiant companion (Whelan *et al.* 1977). However, the optical identification has been thrown into doubt (Argue and Sullivan 1982; Argue *et al.* 1984).

accreted onto neutron stars of X-ray bursters will be rich in hydrogen and/or helium. However, at depths greater than $\sim 10^4$ cm beneath the surface of the neutron star, the density is sufficiently high that nuclear statistical equilibrium will be swiftly achieved. Hence the accreting matter must pass through a series of nuclear burning shells as it is gradually compressed by the accretion of still more material. These burning shells tend to be unstable to thermal runaway (Hansen and van Horn 1975). The existence and strength of the instability are related to the strong temperature dependence of the thermonuclear reactions and the partial degeneracy of the burning material. Runaway in the outermost hydrogen burning shell is usually unable to release large amounts of energy on the time scale of an X-ray burst. The next shell inward, the helium-burning shell, generates rapid and energetic thermonuclear flashes over a wide range of conditions.

Observationally, the ratio of the persistent luminosity $L_{per}(t)$ and the burst luminosity $L_{bst}(t)$ are estimated using the α-value,

$$\alpha = \frac{\int L_{per}(t)\,dt}{\int L_{bst}(t)\,dt}, \tag{2.3}$$

where the range of integration should be wide enough to include a lot of bursts. Since the origin of the persistent luminosity and the burst luminosity is gravitational energy and nuclear energy respectively, the α-value is rewritten as,

$$\alpha = \frac{G\,M\,\triangle M/R}{E_n\,\triangle M}, \tag{2.4}$$

where M and R are the mass and the radius of the neutron star respectively, $\triangle M$ is the mass of the accreted matter and E_n is the nuclear energy generated per unit mass. The observed value of $\alpha \sim 100$ (Lewin *et al.* 1987), together with $GM/R \sim 10^{20}\,\mathrm{erg\,g^{-1}}$, which is a canonical value for a neutron star, gives $E_n \sim 10^{18}\,\mathrm{erg\,g^{-1}}$. This value is consistent with the energy generation rate of helium burning.

If the accretion rates in LMXBs are sufficiently high, the X-ray bursts do not occur since the surface layers on neutron stars become sufficiently hot to consume the nuclear fuel virtually as fast as it accumulates. The critical luminosity discriminating the burst sources and the persistently bright sources is $\sim 0.1\,L_E$ (van Paradijs *et al.* 1979). Bright LMXBs, whose luminosity is near to L_E, therefore do not exhibit X-ray bursts. Some LMXBs, such as X1608-522 and

XB1820–30, show X-ray bursts when their luminosities are small, but do not when they are bright.

The persistent energy spectra of low luminosity LMXBs, which are almost equivalent to X-ray bursters, are power-law with the photon indexes between 0.0 and 2.0, which are in some cases attenuated at high energies by an exponential cut-off with a characteristic temperature from 3 keV up to grater than 20 keV (White, Stella and Parmar 1988). The spectra are commonly explained via Comptonization by hot plasmas around the neutron stars (White, Stella and Parmar 1988, Mitsuda *et al.* 1989). On the other hand, bright LMXBs show thermal spectra roughly expressed by an exponential spectrum with an e-folding energy from 3 to 15 keV. Two different models have been proposed for the energy spectra of bright LMXBs (Mitsuda *et al.* 1984; White *et al.* 1986). While both of these models describe the spectra in terms of the superposition of two components, the physical meanings are considerably different for the two models (see the next section).

2.2.4 Black Hole Candidates

Binary X-ray sources which do not show X-ray pulsations nor X-ray bursts, and whose compact objects are likely to be black holes on certain bases are generally designated as black hole candidates. The X-ray sources which provide the best evidence for black holes, based on mass estimates are, Cyg X-1 ($M > 9.5\,M_\odot$; Paczynski 1974), LMC X-3 ($M > 9.0\,M_\odot$; Cowley *et al.* 1983) and A0620–00 ($M > 3.2\,M_\odot$; McClintook and Remillard 1986).

The case of LMC X-1 is slightly controversial. From the measurement of radial velocities of star 32, one of two candidate stars for the optical counterpart of LMC X-1, Hutchings *et al.* (1983) determined the lower limit of the mass of the compact star as $2.5M_\odot$. The supposition that star 32 is the real counterpart was strengthened by the discovery of the X-ray ionized nebula around star 32 (Pakull and Angebault 1986). The lower limit is much larger than observed neutron star masses (see appendix B), but still, some equations of state allow neutron stars of $2.5M_\odot$(see appendix A). Therefore, the black hole candidacy of LMC X-1 is strong, but not definite.

According to Leibowitz (1984), the mass of the compact star in SS433 is greater

than 4.3 $M_\odot$ on the basis of photometric evidence. However, Kawai *et al.* (1989) concluded that the mass can lie between 1.2 $M_\odot$ and 4 $M_\odot$ from analysis of *Ginga* eclipse data; thus the mass evidence of a black hole in SS433 is still uncertain.

Besides the mass evidence, the similarity in X-ray properties to those of Cyg X-1 is commonly adopted as the criterion to identify black hole candidates. The properties commonly referred to are, definite bimodal behavior (high/low state according to the luminosity in 2 – 10 keV), an "ultra-soft" spectrum (with a hard tail) in the high state, a power-law like spectrum in the low state and rapid time variability in the low state (see section 2.4.1).

GX339–4 is very similar to Cyg X-1 in X-ray properties. It exhibits almost all the X-ray characteristics Cyg X-1 has. However, the recent discovery of $\sim$ 6 Hz quasi periodic oscillations (QPO) from GX339–4 (Makishima and Miyamoto 1988; Dotani 1988; Kitamoto 1989; Miyamoto, Kitamoto and Kimura 1989), suggests strong similarity to bright LMXBs.

Cir X-1 used to be designated as a black hole candidate due to its resemblance to Cyg X-1. Cir X-1 shows fast flickering and bimodal states like Cyg X-1. However, discovery of type I bursts from Cir X-1 (Tennant *et al.* 1986) evidenced the existence of a neutron star in Cir X-1. The X-ray pulsar X0331+52 also shows fast flickering similar to that in Cyg X-1 (Stella *et al.* 1985; Makishima *et al.* 1990b). Thus, fast flickering cannot be taken as a peculiar signature to a black hole source.

White and Marshall (1984) found that the X-ray spectrum of LMC X-3 is extremely soft relative to the vast majority of binary X-ray sources, but similar to that of Cyg X-1 in the high state (figure 2.2). They also pointed out the extreme softness of the spectra of LMC X-1 and A0620–00, which later turned out to have massive compact objects. These three sources all exhibit high energy tails above $\sim$ 10 keV (see figure 2.6 and 2.8), although the cases of LMC X-3 and LMC X-1 are still marginal. Other binary X-ray sources which have ultra-soft spectra and thus could be counted as potential black hole candidates, some of which are transient sources, are 4U0142+61, 4U1524–62, 4U1543–47, 4U1543–62, 4U1630–47, H1705–250 (Nova Ophiuchi), H1743–32, 4U1755–33 and 4U1957+11 (White and Marshall 1984; White, Kaluzienski and Swank 1984). Among them, Nova Ophiuchi and H1743–32 are both transients which show clear high energy tails above $\sim$ 10 keV (White, Kaluzienski and Swank 1984).

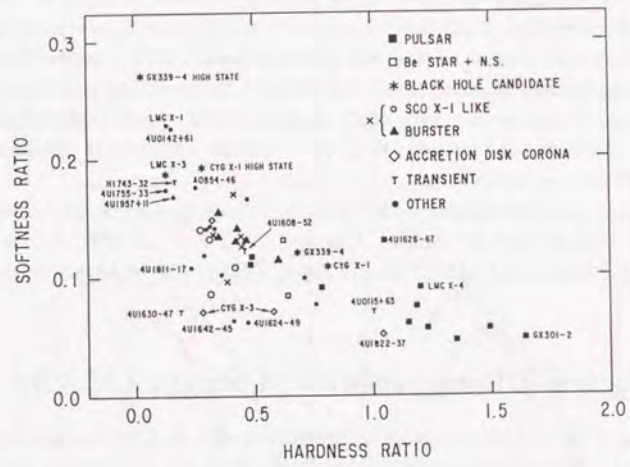

Figure 2.2: A color-color diagram of bright galactic X-ray sources. Sources in the left, upper region have softer energy spectra than those in the right, lower region. The figure was adopted from White and Marshall (1984).

Fabian (1988) and Tanaka (1989) considered a power-law like spectrum extending over ~ 10 keV to be a signature of black hole sources. They noticed the hard-tails in high states rather than the ultra softness, as well as the power-law like spectra in low states. As Fabian (1988) pointed out, in black hole binaries, the temperature can be much higher than in neutron star binaries since the accreted gas loses its gravitational energy at much lower densities owing to the absence of a hard surface. Black hole sources then tend to show harder spectra with $kT > 10\,\mathrm{keV}$ than those of neutron star sources. Tanaka (1989) counted those transient sources GS1826–24, GS2023+33 and GS2000+25, discovered with *Ginga*, as black hole candidates on the basis of the power-law like spectra (GS1826–24 and GS2023+33) or the hard-tail extending over ~ 100 keV (GS2000+25; Sunyaev *et al.* 1988; Efremov *et al.* 1989).

It seems that there is no tendency for black hole candidates to be associated preferentially with MXRBs or LMXBs. Cyg X-1, LMC X-1 and LMC X-3 are MXRBs, on the other hand, A0620–00, GX339–4, GS2000+25 and GS2023+33 are LMXBs.

2.3 Spectral Characteristics of Bright LMXBs

In this section, I give a brief review of energy spectra and spectral variations of bright LMXBs. In X-ray binaries, accreting matter from the companions does not know whether the central objects are black holes or neutron stars; thus the physical situations around weakly magnetized neutron stars and black holes should be similar to each other. Therefore, it is expected that studies of bright LMXBs will throw light on the understanding of black hole candidates.

2.3.1 Persistent Energy Spectra

Mitsuda *et al.* (1984) observed four bright LMXBs, Sco X–1, X1608–522, GX5–1 and GX349+2 with the gas scintillation proportional counters on board *Tenma*. Utilizing the spectral variations of the sources, they successfully resolved the observed energy spectra into two components, a hard component and a soft component (figure 2.3). The hard component has a blackbody spectrum with $kT \simeq 2$

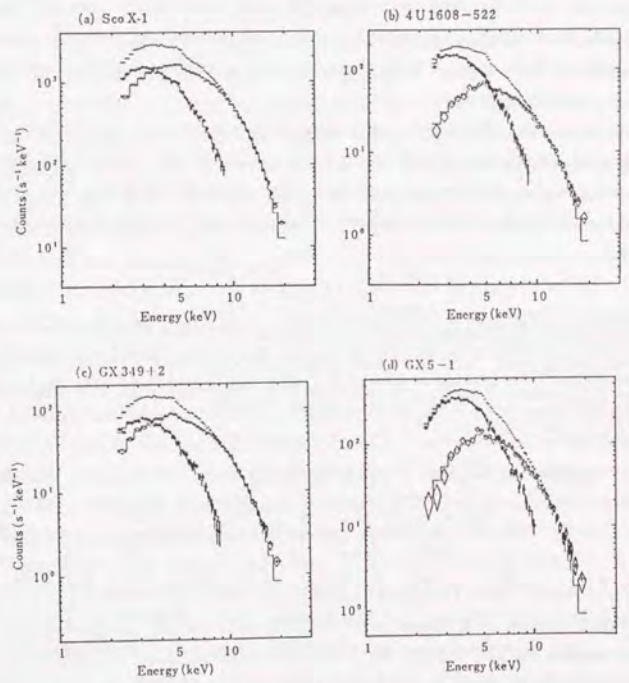

Figure 2.3: Examples of the decomposition of the energy spectra of LMXBs observed with *Tenma* into the two components. The figure was adopted from Mitsuda *et al.* (1984).

keV and its intensity varies considerably with time. On the other hand, the soft component is represented by a superposition of multicolor blackbody spectrum expected from an optically-thick accretion disk and its intensity remains fairly stable. Mitsuda *et al.* (1984) attributed the hard component and the soft component respectively to the emission from the neutron star surface and that from the optically thick accretion disk.

The model spectrum of the soft component they adopted to express optically thick accretion disk emission, which below I call *multicolor disk model*[3] for convenience, is reproduced as follows. According to the standard accretion disk model (e.g., Shakura and Sunyaev 1973), the local temperature of the disk $T(r)$ at radius r is given by,

$$T(r) = \left\{ \frac{3GM\dot{M}}{8\pi\sigma r^3} \left(1 - \sqrt{\frac{r_{in}}{r}}\right) \right\}^{1/4}, \tag{2.5}$$

where, σ is the Stefan-Boltzmann constant and r_{in} is the radius of the inner boundary of the accretion disk. The observed spectrum from the optically thick disk $f_d(E)$ for an inclination θ and at a distance d is, together with the Planckian function $B(E,T)$ and equation (2.5),

$$f_d(E) = \frac{\cos\theta}{d^2} \int_{r_{in}}^{r_{out}} 2\pi r\, B\Big(E, T(r)\Big)\, dr \tag{2.6}$$

$$\simeq \frac{8\,\pi\, r_{in}^2 \cos\theta}{3\,d^2} \int_{T_{out}}^{T_{in}} \left(\frac{T}{T_{in}}\right)^{-3/11} B(E,T)\, \frac{dT}{T_{in}}, \tag{2.7}$$

where $T_{in} = T(r_{in})$ and $T_{out} = T(r_{out})$. This is the multicolor disk spectrum. In the above equation, the term $\sqrt{r_{in}/r}$ in equation (2.5) is neglected. This is not correct near r_{in} and therefore r_{in} in equation (2.6) should not be regarded as the exact radius of the inner edge of the disk; r_{in} but should be taken as a measure of the size of the disk. Since almost all the X-rays emerge from the inner region of the accretion disk, the multicolor disk spectrum in the X-ray band has only a weak dependence on T_{out} so is effectively determined by the two parameters, $r_{in}^2 \cos\theta/d^2$ and T_{in}. The bolometric luminosity of the disk L_{bol} and the observed bolometric flux f_{bol} are respectively given by

$$L_{bol} = \int_{r_{in}}^{r_{out}} 4\pi\, r\, \sigma\, T^4(r)\, dr \simeq 4\pi\, r_{in}^2\, \sigma\, {T_{in}}^4, \tag{2.8}$$

[3]This model is often called as *disk blackbody model* (e.g. Makishima *et al.* 1986).

and

$$f_{bol} = \frac{\cos\theta}{2\,\pi\, d^2}\, L_{bol} = \frac{2\cos\theta}{d^2}\, r_{in}^2\, \sigma\, {T_{in}}^4, \tag{2.9}$$

where $r_{out} \gg r_{in}$ ($T_{out} \ll T_{in}$) is assumed.

Mitsuda *et al.* (1984) had noticed systematic excesses of observed flux at $\gtrsim 10$ keV in comparison with their two component model. The problem disappeared when a small amount of Comptonization by a thin hot plasma is applied to the hard component (Mitsuda and Tanaka 1985). The modified two component model, consisting of the multicolor disk plus the Comptonized blackbody (Nishimura, Mitsuda and Itoh 1986) model could successfully fit energy spectra of thirteen LMXBs (including the four sources in Mitsuda *et al.* 1984) observed with *Tenma* (Mitsuda and Tanaka 1985). Below I call this two component model the "Eastern model" for convenience.

White, Peacock and Taylor (1985) and White *et al.* (1986) proposed an alternative two component model for the spectra of LMXBs. Their two component model consists of a blackbody plus what they call *unsaturated Comptonized spectrum*. The unsaturated Comptonized spectrum, which is sometimes approximated with the function of the form $E^{-\Gamma}\exp(-E/kT)$, is expected as a solution of the Kompaneets equation for the Comptonization of low-energy photons on high-energy electrons (Sunyaev and Titarchuk 1980). This two component model could also produce acceptable fits to the energy spectra of Sco X–1 (White, Peacock and Taylor 1985) and GX9+1, X1705–44, GX17+2, Sco X-2, Sco X-1, XB1728-34 and Ser X-1 (White *et al.* 1986), all taken with the *EXOSAT* satellite. The characteristic flarings of Sco X-1 and Sco X-2 were ascribed to increases in the luminosity of the blackbody components (White *et al.* 1986). The unsaturated Comptonized component is identified as coming from the inner disc region, while the blackbody component is from the heated surface of a neutron star. Below I call this two component model the "Western model" for convenience.

The role of the blackbody component is different for the Eastern model and Western model. In the Eastern model, its temperature is $\sim$ 2 keV so that it is dominant at higher energies than in the Western model in which the blackbody temperature is typically $\sim$ 1.5 keV. The two models are compared to each other by Makishima and Mitsuda (1985). They pointed out that the two models can be made almost identical over the 2 – 10 keV energy range, so that it is difficult to dis-

tinguish one from the other by conventional spectral fitting. They concluded that, on several physical considerations, the Eastern model gives a better explanation of observations of bright ($L_X \gtrsim 10^{37}$erg s^{-1}) LMXBs than the Western model.

White, Stella and Parmar (1988) pointed out that inner part of accretion disks cannot radiate as a blackbody because electron scattering will tend to increase the mean photon energy. They criticized the Eastern model on the grounds that it yields too high a temperature of the accretion disk when applied to bright LMXBs, which results in a mass accretion rate larger than that corresponding to the Eddington limit. They concluded that the Western model is the proper model to describe the energy spectra of not only bright LMXBs, but also low luminosity LMXBs with a small contribution of the blackbody component and black hole candidates with no contributions from such.

Mitsuda *et al.* (1989) examined the two models by applying them to the spectra of X1608–522, observed with *Tenma* over a wide range of luminosity. They found all the ten spectra could be fitted with the Eastern model satisfactorily. The result indicated that the ratio of the energy flux emitted from the accretion disk and that emitted from the neutron star surface is constant, independent of the total flux, which seems physically reasonable. On the other hand, the Western model could not fit two of the ten spectra, and the best-fit N_H values of the rest of them showed a systematic decrease with decrease of intensity. Mitsuda *et al.* (1989) argued against White, Stella and Parmar (1988) that the shape of the local spectrum emerging from an accretion disk can be approximated with the blackbody spectrum even when electron opacity is dominant and the resultant color temperature becomes considerably higher than the effective temperature of the emission (cf. appendix D).

2.3.2 Short Time Spectral Variation

On the time scale from seconds to minutes, fractional variations (see equation [5.1]) of bright LMXBs generally increase toward higher energies (figure 2.4; Stella, Kahn and Grindlay 1984; Makishima 1988). Due to the self-similarity of the time variations of LMXBs (Makishima 1988), this property depends little on the frequency range. On longer time scales, such a tendency was first pointed out by

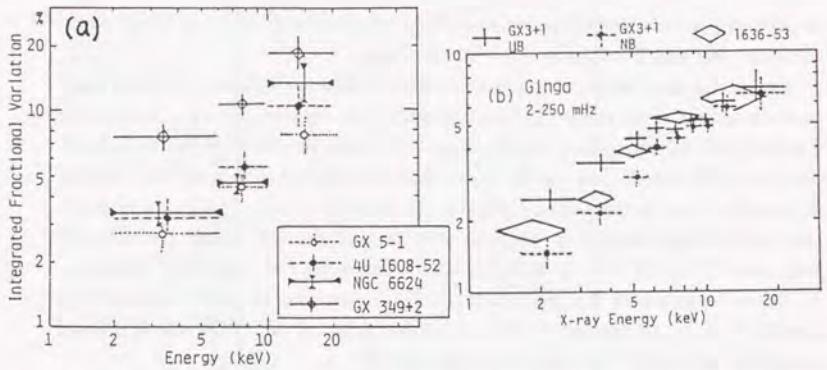

Figure 2.4: Dependence of the fractional variations of bright LMXBs on the X-ray photon energy. (a) *Tenma* results, calcurated over 2 – 250 mHz. (b) *Ginga* results, calcurated over 2 – 250 mHz. The figure was adopted from Makishima (1988).

Mitsuda *et al.* (1984) and ascribed to the variation of the hard, $\sim$ 2 keV black body component (see the previous section).

Makishima *et al.* (1989) studied random variations of GX 3+1 in detail over 2 – 20 keV on time scales from seconds to minutes. During the observation, the source exhibited two spectral branches in the intensity-hardness diagram; the "normal branch", on which the intensity and the spectral hardness are possitively correlated and the "uncorrelated branch", on which they are not correlated. On both branches, the fractional variations of the source increased toward higher energies (figure 2.4). Making use of intensity-sorted spectroscopy, they successfully extracted varying spectral components on each branch. On the normal branch, overall variations can be described as intensity changes in a single component that can be represented by a $\sim$ 2 keV blackbody. They interpreted, in the framework of the Eastern model (see the previous section), this variable component as due to variation of the emission from the neutron star surface. On the other hand, variations on the uncorrelated branch were described as superposition of independent intensity variations of two blackbody emissions; the temperatures of the two emissions were 1.3 keV and 2.3 keV, respectively. They interpreted these two

components as variation of the emission from the inner edge of the optically thick accretion disk and from the neutron star surface.

On shorter time scales than a second, Quasi Periodic Oscillations (QPO) have been discovered from about ten bright LMXBs (for reviews, see e.g., Lewin, van Paradijs and van der Klis 1988; Hasinger 1988; van der Klis 1989). The rapid time variabilities including the QPO have a close relationship to spectral branches in intensity-color or color-color diagrams. In general, on the "horizontal branch" (the spectral hardness is kept constant over the intensity variations), the centroid frequency of the QPO is 20 – 50 Hz, and it increases with the X-ray intensity. On the other hand on the "normal branch" (the spectral hardness is possitively correlated with the intensity), the centroid frequency of the QPO, which is little correlated with the X-ray intensity, is about 6 Hz.

Dotani (1988) investigated normal branch QPO of six sources (including GX339–4) observed with *Ginga*. He found that, for all the sources, fractional amplitudes of the QPO increase toward higher energies. In the framework of the Eastern model, he ascribed the QPO to the oscillations of the hard components. He concluded that instablility in the inner region of the optically thick accretion disks is the cause of the QPO; the instability modulates mass accretion rate onto the neutron star with the frequency of the QPO and then induces oscillations in the hard components on the neutron star surfaces.

2.4 Energy Spectra of Black Hole Candidates

In this section, I review previous observations of black hole candidates, Cyg X-1, LMC X-3, LMC X-1, GX339–4, A0620–00 and GS2000+25, mainly focusing on their energy spectra and spectral variations.

2.4.1 Cyg X-1

It is well known that Cyg X-1 has distinct bimodal spectral states, the high state and the low state, according to the X-ray flux in 2 – 10 keV (see Oda 1977; Liang and Nolan 1984 for reviews). Most of time, Cyg X-1 is in the low state. As a matter of fact, the high state has been observed only three times so far; from 1970

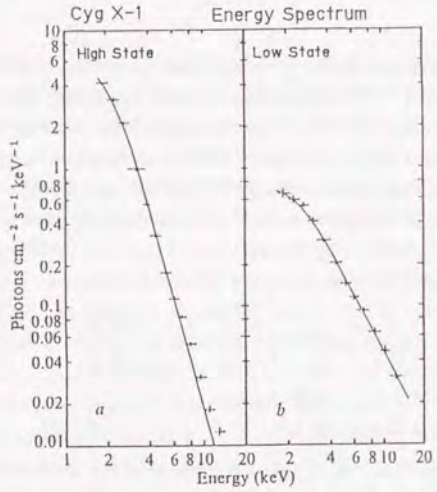

Figure 2.5: Energy spectra of Cyg X-1 in the high and low state taken by the Ariel-V satellite. This figure was adopted from Sanford *et al.* (1975)

to 1971, in 1975 and 1980 (see Oda 1977; Liang and Nolan 1984 and references therein) [4].

In the low state, the spectrum is characterized by a simple power-law over 1 – 100 keV range with a photon index [5] of ~ 1.7. The spectrum begins to fall off steeply between 100 keV and 1 MeV.

The high state sets in on a time-scale of days and lasts for about a month. A new, intense, much softer spectral component appears below 10 keV, which corresponds to a power-law with a photon index of 3 – 4 or a blackbody of a temperature lower than 1 keV. The spectral intensity above 10 keV, contrary to that below 10 keV, decreases somewhat more than in the low state retaining the power-law form with slight steepening of the slope ($\alpha \sim 2$). An example of energy spectra of Cyg X-1 in the high and the low state is shown in figure 2.5.

[4] Since the launch of *Ginga*, Cyg X-1 has been monitored by the ASM and has been shown to be in the low state up to December, 1990.

[5] In this thesis, when I refer to the index of a power-law, it is the photon index α in dN/dE (photons s^{-1} cm^{-2} keV^{-1}) $\propto E^{-\alpha}$.

A thermal Comptonization model is widely accepted to explain the hard power-law spectrum of Cyg X-1. This model can explain the power-law shape of the spectrum together with the fall off at higher energies. The anticorrelated spectral variation between the two luminosity states is also considered to be a confirmation of the thermal Comptonization model (e.g., Coe, Engel and Quenby 1976).

An analytical form of the Comptonized spectrum of low energy photons by high energy electrons is derived by Sunyaev and Titarchuk (1980), as a solution of the Kampaneets equation. That is,

$$f(E) = N \left(\frac{E}{kT_e}\right)^2 e^{-E/kT_e} \int_0^\infty \xi^{n-1} \left(1 + \xi \frac{kT_e}{E}\right)^{n+3} e^{-\xi}\, d\xi, \qquad (2.10)$$

$$\text{where } n = -\frac{3}{2} + \sqrt{\gamma + \frac{9}{4}};\ \gamma = \frac{\pi^2}{3} \frac{m_e c^2}{(\tau_e + 2/3)^2 kT_e}.$$

Here, N is the normalization, kT_e is the temperature of the electron cloud and τ_e is the Thomson optical thickness of the cloud. This formula is valid for $h\nu_{soft} \ll E \ll kT_e$ ($h\nu_{soft}$ is the energy of the low energy photons). In this energy range, the emergent spectrum depends little on $h\nu_{soft}$. This formula was applied to the spectrum of Cyg X-1 (Sunyaev and Trümper 1979; Sunyaev and Titarchuk 1980) and then the parameters of $kT_e \sim 27$ and $\tau_e \sim 5$ were obtained. Fits of the Comptonization model to spectral data obtained independently by various groups uniformly give $kT_e \sim 27 - 60$ keV and $\tau_e \sim 1 - 5$ (Liang and Nolan 1984 and references therein).

In the standard accretion disk model (Shakura and Sunyaev 1973; Novikov and Thorne 1973), such a high temperature cannot be attained in accretion disks. Thorne and Price (1975) argued that the secular instability present in the inner region of the standard "cool" disk could swell the optically thick radiation-pressure dominated region into a hotter, gas-pressure dominated, optically thin region. A self consistent "hot disk" model with these properties has been constructed by Shapiro, Lightman and Eardley (1976). In this "two-temperature" disk model, the electrons are at 10^9 K throughout the inner region while the ions are 3 – 300 times hotter. Copious soft photons for the Comptonization are provided by thermal emissions in outer optically thick portions of the disk or by cyclotron emissions in the inner region (Apparao 1984).

The "hot corona" model has been proposed as another hot disk model (Liang and Price 1977; Bisnovatyi-Kogan and Blinnikov 1977; Galeev, Rosner and Vaiana 1979). This model consists of a hot corona sandwiching an optically thick disk. The high temperature of the corona is produced by acoustic and Alfv́en waves and magnetic dissipation in the upper disk atmosphere. Hard X-rays are emitted from the corona via the Comptonization of those soft photons provided in the optically thick cool disk.

In the low state spectrum taken with the gas scintillation proportional counter on board *EXOSAT*, Barr *et al.* (1985) advocated the discovery of a broad emission feature at 6.2 keV as a significant deviation from a power-law. The typical equivalent width and FWHM of the line were 120 eV and 1.2 keV respectively. They proposed the line as a Compton-redshifted iron K-line and suggest that it comes from recombination in an optically thick photoionized corona above and below the accretion disk. On the other hand, from *Tenma* observations, Kitamoto *et al.* (1990) derived contradicted results concerning the emission line. They found a emission line around 6.5 keV, not 6.2 keV. Furthermore, the equivalent width of 60 – 80 eV and the FWHM of 0.36 – 1.18 keV (with large errors of typically ~ 0.6 keV) were significantly smaller than those by Barr *et al.* (1985) [6].

Cyg X-1 exhibits large fluctuation on all time scales including bursts of seconds to milliseconds durations (Oda 1977). For the high state, the spiky variations are more prominent for higher energy bands compared to lower energy bands; whereas in the low state, the profile of the variation is similar over the energy range up to 10 keV or higher (Oda *et al.* 1976). It appears that the variations are the characteristic feature of the hard component and are buried in the enhanced soft component when Cyg X-1 is in the high state.

2.4.2 LMC X-3 and LMC X-1

White and Marshall (1984) pointed out that the X-ray spectrum of LMC X-3 and LMC X-1 are very soft compared to the vast majority of galactic binary X-ray sources (figure 2.2). They reproduced the energy spectra of the two sources from the observations of HEAO-1 A-2 Medium Energy and High Energy Detectors and

[6] This probable iron emission line is examined on the *Ginga* data in section 5.1.1 and 6.3.

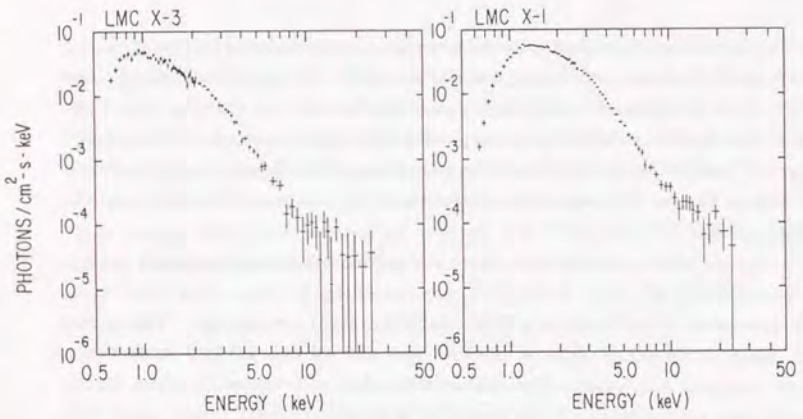

Figure 2.6: The incident energy spectra of LMC X-3 and LMC X-1; they are combination of the spectra taken by the *Einstein* and *HEAO-1* experiments. The figure was adopted from White and Marshall (1984).

Einstein Solid State Spectrometer (figure 2.6). Over the 3 – 10 keV range, these spectra can be fitted with a power-law with the indices 3.1 ± 0.2 (LMC X-3) and 2.8 ± 0.2 (LMC X-1). These values are comparable to that of Cyg X-1 in the high state. Both sources showed evidence of high energy excesses above 10 keV, although their statistical significance is low.

LMC X-3 had been monitored in 1977 – 1979 by the *HEAO-1* satellite. The source was variable by a factor of three on time scales of 50 days; however, systematic change of the spectral hardness ratio was not detected (White and Marshall 1984). Rapid $\sim$ 1 sec flickering comparable to that seen from Cyg X-1 in its low state was not detected from LMC X-3 (White and Marshall 1984).

LMC X-3 was observed on seven occasions in 1983 and 1984 with *EXOSAT*, covering various orbital phases (Treves *et al.* 1988b). No phase related variability was detected. An acceptable fit to the spectrum of LMC X-3 was obtained using the model of the Comptonization spectrum by Sunyaev and Titarchuck (1980) (equation [2.10]; Treves *et al.* 1988b; White, Stella and Parmar 1988). The best fit values of the parameters are, $kT_e \sim 1$ keV and $\tau_e \sim 20$. Treves *et al.* (1988b) and

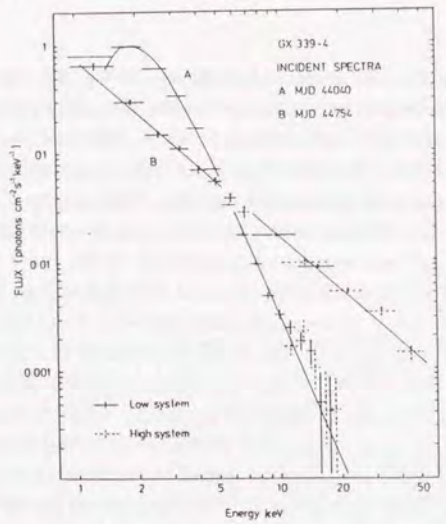

Figure 2.7: Examples of energy spectra of GX339–4 taken by Ariel-V in the high and low state. The figure was adopted from Ricketts (1983).

White, Stella and Parmar (1988) pointed out that the Comptonization parameter, $y = (4\,kT_e/m_ec^2)\,\tau_e^2$, takes comparable values ($3 \sim 5$) in the both cases of Cyg X-1 and LMC X-3.

2.4.3 GX339–4

GX339–4 varies greatly in X-rays on a wide range of time scale. It shows three distinct intensity states; the high state ($\sim$ 500 mCrab), the low state ($\sim$ 100 – 200 mCrab) and the off state ($<$ 20 mCrab) (Market *et al.* 1973). Spectral and timing behaviours of GX339–4 are very similar to those of Cyg X-1.

In the high state, the energy spectrum is very soft; a typical photon index of the spectrum in 1 – 20 keV is $\sim$ 4 (figure 2.7; Market *et al.* 1973; Jones 1977; Doxsey *et al.* 1979; Ricketts 1983; Maejima *et al.* 1984; Makishima *et al.* 1986).

In the high state of GX339–4, Makishima *et al.* (1986) detected a distinct hard-tail which is dominant above $\sim$ 10 keV. They fitted the overall spectrum

with the two component model composed of the multicolor disk model (for the soft component; see section 2.3.1) and a power-law (for the hard-tail). They noticed that the temperature of the multicolor disk ($\sim$ 0.77 keV) is significantly lower than the typical value for LMXBs (1 – 1.4 keV) and claimed that these temperatures reflect masses of the central objects. They suggested the central object in GX339–4 is more massive than neutron stars and very likely to be a blackhole. The hard-tail was interpreted to originate in the inner most region of the accretion disk, which is optically thin and very hot ($kT \sim 60$ keV), via Comptonization of soft X-ray photons from outer portions of the disk.

On the other hand in the low state, the energy spectrum is, in most cases, hard, with a typical photon index of ~ 1.7 (figure 2.7; Samimi *et al.* 1979; Ricketts 1983; Motch *et al.* 1983; Maejima *et al.* 1984). Exceptionally, a soft spectrum (with a hard-tail) similar to that in the high state was observed (designated as the soft state by Ilovaisky *et al.* 1986) even with the typical intensity of the low state ($\sim$ 83 mCrab; Ilovaisky *et al.* 1986) Ilovaisky *et al.* (1986) interpreted the soft component as an unsaturated Comptonized spectrum (see section 2.3.1).

GX339–4 in the off state was first detected by the *EXOSAT* satellite (Ilovaisky *et al.* 1986). The X-ray energy spectrum was hard and represented by a power-law with the photon index of ~ 1.7.

In the low state, GX339–4 shows rapid, aperiodic variations with minimum time scales of several tens of milliseconds (Samimi *et al.* 1979; Motch *et al.* 1983; Maijima *et al.* 1984). The r.m.s. amplitude of the variation is as much as $\sim$ 35 % on time scales of a fraction of a second to tens of seconds (Maejima *et al.* 1984). In the 1 – 22 keV range, the characteristics of the fluctuation were independent of X-ray energy (Maejima *et al.* 1984). In the high state, the short-term (less than several minutes) variation disappears; intrinsic variation in excess of the Poisson noise level has not been detected (Maejima *et al.* 1984; Makishima *et al.* 1986).

The optical faintness during the X-ray off state and a large range of optical variation (V = 15.4 – 21) imply a low-mass optical counterpart, and the optical emission seems a direct consequence of mass accretion onto the compact object. In the X-ray low state, peculiar, rapid ($\lesssim$ 20 msec) optical activity was detected (Motch, Ilovaisky and Chevalier 1982). Simultaneous optical/X-ray observations on the same occasion revealed an intensity anticorrelation between optical wavelength and 1 – 13 keV X-rays on time scales in 15 – 96 sec (Motch *et al.* 1983). On longer time scales, over the low state, soft state and off state, Ilovaisky *et al.* (1986) found a good correlation between the optical luminosity and the luminosity of the power-law spectrum, including the hard-tail in the soft spectrum. These facts led to suggestions of cyclotron radiation as the origin of the optical photons (Fabian *et al.* 1982; Motch *et al.* 1983; Apparao 1984)

2.4.4 A0620–00

A0620-00 is the X-ray nova discovered with *Ariel-V* on August 3, 1975 (Elvis *et al.* 1975). For two months in 1975, it was the brightest celestial X-ray source. The light curve of A0620-00, which will be compared to that of GS2000+25 in the following section, is shown in figure 2.9.

An Inverse correlation between the soft and the hard X-ray flux similar to that of Cyg X-1 was observed from A0620-00, both during the initial turn-on (Ricketts *et al.* 1975) and the decay phase (Coe, Engel and Quenby 1976).

The X-ray spectrum of A0620–00 was hard ($\alpha \sim 1.7$) when first detected and then the overall intensity rose to the precursor peak holding the spectral shape. Secondly, a subsequent rise to the maximum intensity, which was attained after $\sim$ 10 days after the discovery, was entirely due to a strong enhancement of X-rays below 10 keV, giving a marked softening in the overall spectrum. In fact, the observed flux above 10 keV actually fell during this period (figure 2.8a). Near the maximum, the spectrum up to 60 keV was approximated with a power-law of index $\sim$ 5, with an indication of hardening at $>$ 30 keV to a slope of $\sim$ 2. In mid-October, about two months after the maximum, the soft X-ray intensity had decreased by a factor of over five, whereas the 20 – 200 keV intensity had increased at least by a factor 2 (figure 2.8b). A spectral break with two power-laws was definitely required at around 15 keV to satisfy the totality of the October data.

2.4.5 GS2000+25

The bright transient X-ray source in the constellation Vulpecula, GS2000+25 was discovered on April 23, 1988 with the ASM on board *Ginga* (Makino 1988; Tsunemi

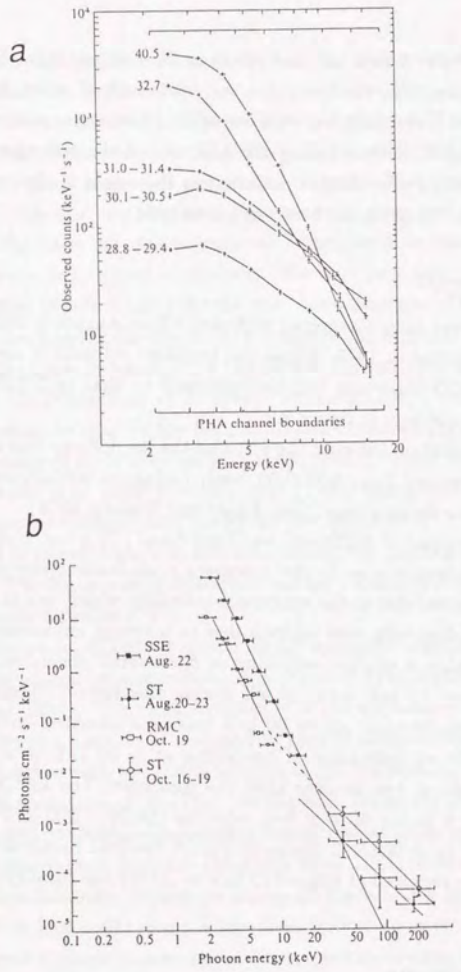

Figure 2.8: Energy spectra of A0620–00 (a) during the rise to the maximum brightness and (b) in mid-August 1975 (near the maximum) and in mid-October 1975. The figures (a) and (b) were adopted from Ricketts *et al.* (1975) and from Coe, Engel and Quenby (1976), respectively.

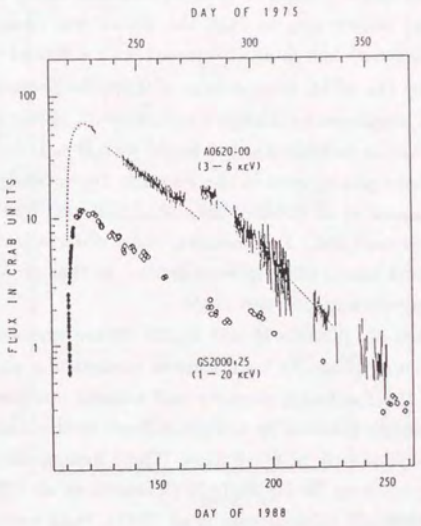

Figure 2.9: The X-ray light curve of GS2000+25 obtained with the ASM (open and filled circles [Tsunemi *et al.* 1989b]) and of A0620–00 (dots [Elves *et al.* 1975] and vertical bars [Kaluzienski *et al.* 1977]).

et al. 1988a). The X-ray light curve of GS200+25 by ASM is shown in figure 2.9. From the first detection on April 23 until maximum light on April 28, GS2000+25 increased linearly to a maximum intensity of 12 Crab in the energy range 1 – 6 keV. After this time, the source decreased in an exponential decay until the end of June. During a 5 day observation in July, the source was observed to have brightened by 50 %. Afterward, the source decreased with a similar decay curve.

After the discovery by the ASM, observations of GS2000+25 were carried out to search for the optical counterpart (Okamura and Noguchi 1988). On April 27, 1988, in the X-ray error box, a variable star was found with $B \sim 17.5$; this star was totally invisible in previous plates, even in the Palomar Observatory Sky Survey prints (> 21 mag). Tsunemi *et al.* (1989b) concluded this star had increased at least 3.5 mag during this outburst. Furthermore, radio observations were made for this candidate star and then radio emission similar to that of A0620–00 was detected (Hjellming, Calovini and Córdova 1988).

The X-ray light curves of GS2000+25 and A0620–00 are very similar to each other (figure 2.9). The rising phase for both sources consists of a short precursor event 6 – 7 days before the maximum intensity and a linear increase in intensity until 3 days before maximum followed by a slight rollover to the maximum. Both sources reached the peak intensity in 6 – 8 days. The e-folding decay time after the maximum is 30.8 ± 0.7 days for GS2000+25 (Tsunemi *et al.* 1989b), while it is 28.9 ± 1.8 days for A0620-00 (Kaluzienski *et al.* 1977). Both sources exhibited enhanced brightening during the declining phase (50 - 75 days after the maximum intensity).

The international Röntgen observatory on the *Kvant* orbiting module observed GS2000+25 in May, June and October, 1988 (Sunyaev *et al.* 1988; Efremov *et al.* 1989). The observations in May and June showed the energy spectrum of GS2000+25 comprised two components similar to those of A0620-00; a soft component and a hard component (figure 2.10). The soft component was dominant in 4 – 15 keV and contributed 90 % of the luminosity. The hard component extended to energies 200 – 300 keV and was approximated with a power-law with a photon index of 1.81 ± 0.01 (Sunyaev *et al.* 1988). During the second set of observations in October 2 – 6, 1988, the energy spectrum was taken only above ~ 20 keV. The flux of the hard component had decreased by 20 times in comparison with that in

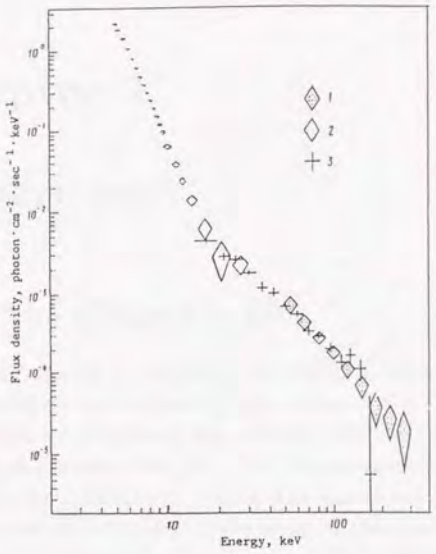

Figure 2.10: An energy spectrum of GS2000+25 determined by data from three instruments of the Röntgen observatory on the *Kvant* orbiting module. The data taken in May 15 – 17 and June 4 – 8 were combined together. This figure was adopted from Sunyaev *et al.* (1988).

June. However, the slope of the hard component was still constant (photon index = 2.0±0.2).

Chapter 3

Experiment

3.1 The Ginga Satellite

Ginga (Makino and the ASTRO-C team 1987) is the third Japanese X-ray astronomy satellite. It was launched by the Institute of Space and Astronautical Science (ISAS) from the Kagoshima Space Center (KSC) on February 5th 1987, then put into a roughly circular orbit ($e \sim 0.01$) with an apogee of 670 km, a perigee of 510 km and an inclination of 31 degrees. The orbital period is about 96 minutes and the argument of the perigee rotates in the orbital plane with a 37-day period.

Figure 3.1 shows the schematic view of the *Ginga* satellite. The dimensions of *Ginga* are 1000 ×1000 × 1550 mm and the weight is approximately 420 kg.

The *Ginga* satellite carries three instruments for high energy astrophysics; the large area proportional counter (LAC; Turner *et al.* 1989), the all sky monitor (ASM; Tsunemi *et al.* 1989a) and the gamma-ray burst detector (GBD; Murakami *et al.* 1989).

The LAC is the main instrument of *Ginga*. With the large effective area and the low internal background, the LAC is the most sensitive instrument in the medium X-ray energy band yet placed in orbit. The details of the LAC are described in the next section.

The ASM is an X-ray sky monitor system with a wide field of view. It consists of two proportional counters with six different fields of view, each of which is 1° × 45° (FWHM). The ASM scans about 70 % of the sky during a rotation of

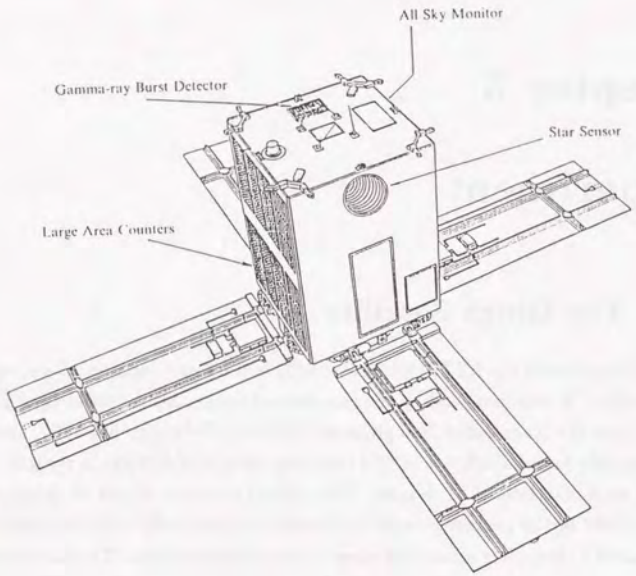

Figure 3.1: The schematic view of the *Ginga* satellite. The three instruments, LAC, ASM and GBD are indicated in the figure. One of the two star trackers (STT) is also shown. The figure was adopted from Turner *et al.* (1989).

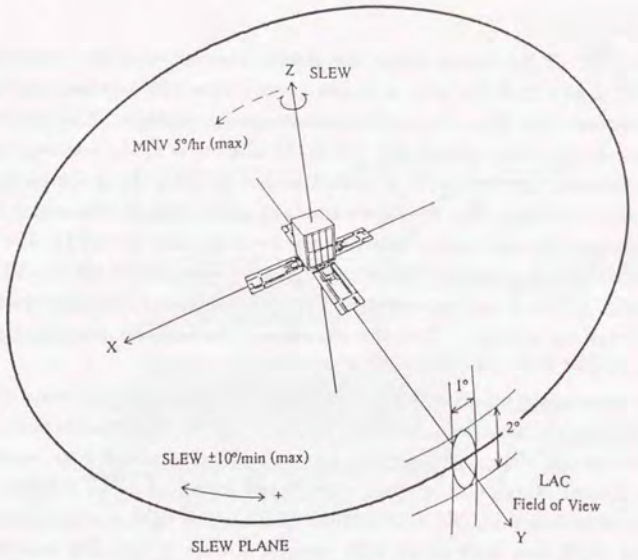

Figure 3.2: The collimator field of view (FWHM) and the satellite three axes. The stability of the attitude is better in the Y direction than in the Z direction and hence the field of view has an elliptical shape. The Y direction is in the slew plane of the spacecraft. The figure was adopted from Turner *et al.* (1989).

the satellite around the spin axis (Z-axis). The detection limit is 50 mCrab in the scanning observations.

The main purpose of the GBD is to detect gamma-ray bursts in a wide energy range (1 – 384 keV) with high time and energy resolution. The GBD is also used as a real-time alarm for high particle background in the orbit in order to protect the LAC and the ASM. The GBD is so designed that it can perform observations in parallel with the LAC or the ASM.

The satellite attitude is controlled by a momentum wheel whose rotation axis is aligned to the Z-axis, and three magneto-torquers. Exchanging angular momentum with the momentum wheel, the satellite moves around the Z-axis with relatively high speed (14°/minute; figure 3.2). The magneto-torquers move the Z-axis

relatively slowly (5°/hour) and adjust the angular momentum of the momentum wheel. The Z-axis must be held at angles greater than 135 degrees away from the Sun in order that the solar paddles receive enough sunlight. This condition constraints the direction of the LAC. When the satellite is in the pointing mode (usual operation), the attitude is stabilized within 0.1°/day using the on-board gyroscopes for reference. The absolute attitude of the satellite is determined later on ground using the star images taken by the two star trackers (STT). The sun sensors and/or the geomagnetic sensors are also used when one of the two STT is not available. Attitude is extrapolated according to the gyroscope data to the time when STT are not available. Typically, the error of the attitude determination is less than 0.1°.

An on-board data processor (DP) accumulates all the data (LAC data, ASM data, GBD data, attitude data, housekeeping data and so on) and edits them into a telemetry format. The data processor has three bit rate modes; high, medium and low. Except during contacts with the ground station at KSC, the data are stored in the on-board bubble data recorder (BDR). The BDR has a capacity of 41.9 Mbits which can store about 1366 minutes of data in low, 341 minutes in medium and 43 minutes in high bit rate.

3.2 The Large Area Counter

The LAC consists of eight identical proportional counters with a total effective area of 4000 cm^2. An exploded view of the LAC detector is shown in figure 3.3a. The LAC has a multicell structure and the signal cells are covered with guard cells from five sides, which reduces background via anti-coincidence techniques. The configuration of the cells is schematically shown in figure 3.3b. The signal wires are L1, R1 and S23 and the guard wires are V1 and V2. At the ends of these wires, there is an end guard cathode (EV) to detect charged particles passing through the ends of the cells. Since charged particles ionize the gas along their path, they usually produce signals in two or more cells. Hence the anti-coincidence reduces charged particle event significantly. The X-ray events selection criterion is

(L1 *xor* R1 *xor* S23) *not* (V1 *or* V2 *or* EV).

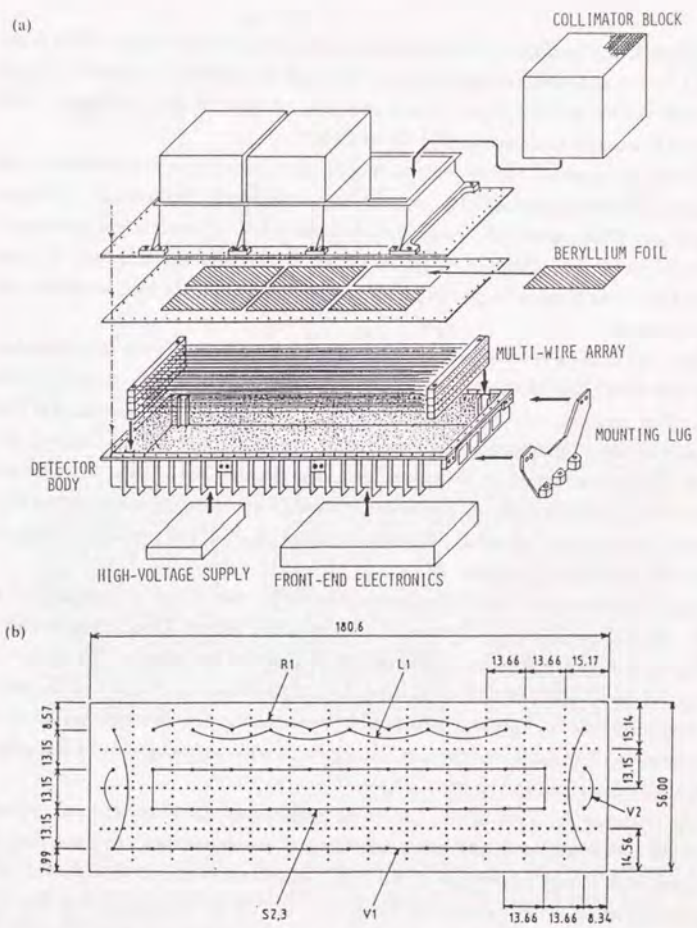

Figure 3.3: (a) An exploded view of a LAC detector, showing the components. (b) Cross section of the proportional counter gas cell showing the anode connections. Dimensions are in units of mm. The figure was adopted from Turner *et al.* (1989)

The diffuse X-ray background coming from outside the field of view, which is not rejected by the anti-coincidence system, is reduced by shielding the LAC with 0.2 mm thick tin for all directions except the field of view of the collimator. The thickness is enough to reject X-rays up to 60 keV.

The gas mixture of the counter is determined from three requirements; low background, moderate sensitivity to hard X-rays and long life in orbit. The mixture is argon 70 %, xenon 25 % and carbon dioxide 5 %. The total gas pressure is 2 atom at 20 °C. Beryllium of 62 μm thickness is used for the entrance window; the thickness was chosen to give reasonable freedom from leaks and adequate soft X-ray response.

The LAC field of view is restricted to $1.1° \times 2.0°$ (FWHM) by a stainless steel collimator which has hexagonal structure to give an elliptical field of view (figure 3.4a). The angular response of the collimator and its energy dependence was checked on-board by scanning the Crab nebula at various elevations (figure3.4b). A part of the inside surface of the collimator is painted with silver to eliminate the possible production of iron fluorescence lines. Raw energy spectra of the LAC therefore contains the silver K_α fluorescence line at 22.1 keV, which is used for calibration of the energy scale.

Typical background of the LAC is $\sim$ 50 c/s for non X-ray events and $\sim$ 18 c/s for the diffuse X-ray background. Although the diffuse X-ray background is constant, the non X-ray background varies by a factor of two through the observing day and by 25 % with a period of 37-days due to the slight eccentricity of the orbit. Hence appropriate background subtraction is needed for detailed spectral study of X-ray sources. The origins of the LAC background and the background subtraction method are described in the next section.

The response function of the LAC was constructed based on ground calibrations and observations of the Crab nebula and the supernova remnant Cas A. Linearity and energy resolution of the LAC, which are required to construct the response function, were determined before the launch by irradiating the detector with monochromatic X-rays of various energies. The linearity is approximated by a quadratic formula,

$$P = A + BE + CE^2,$$

where P is the pulse amplitude, E is the X-ray energy and A, B and C are con-

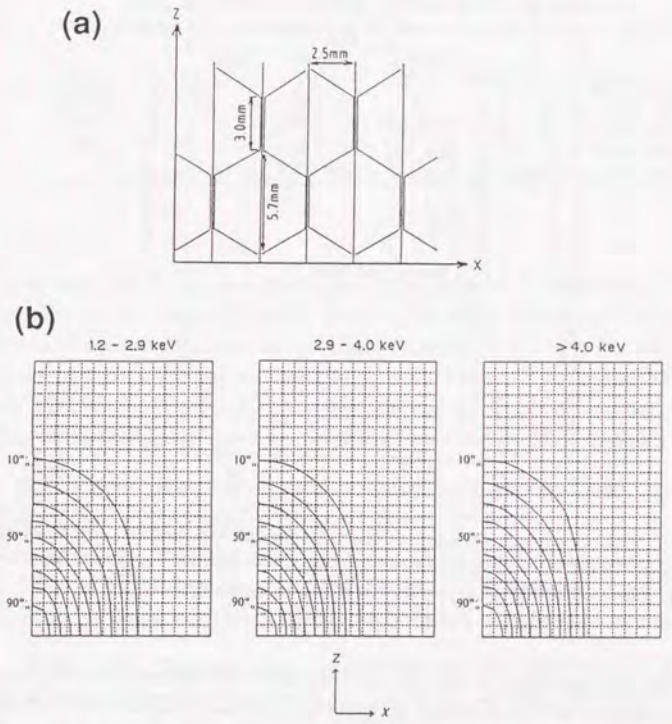

Figure 3.4: (a) Cross section of the collimator showing the shaped and flat plates. (b) The collimator angular response function. The grid size with dotted line is 0.1°, and three different energy bands are shown. The figures were adopted from Turner *et al.* (1989).

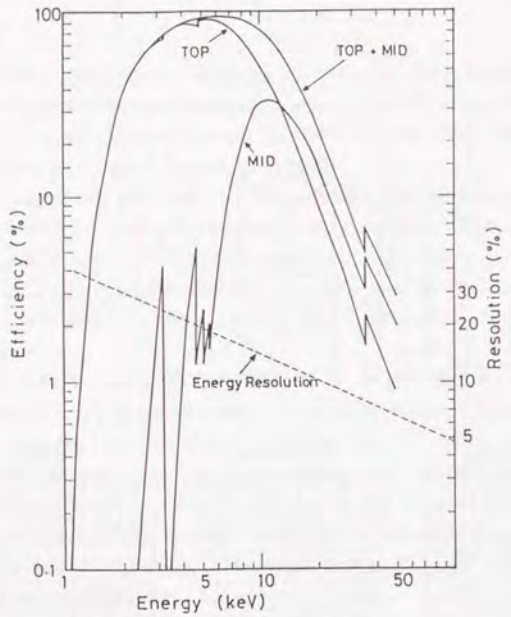

Figure 3.5: The photopeak efficiency of the LAC for the top, middle, and top plus middle layers (solid curves) and the energy resolution (dashed line) as a function of energy. The measured energy resolution follows closely the function form $E^{-0.5}$. The figure was adopted from Turner *et al.* (1989).

stants with different values below and above 4.8 keV. The efficiency as a function of energy was derived from technical data and the observations of the Crab nebula. Reduction of the efficiency by the anti-coincidence was also taken into account. The efficiency of L1 + R1 (top layer), S23 (mid layer) and the sum of both are shown in figure 3.5.

Each LAC detector has its own high voltage (HV) supply; the output voltage is variable to be 16 fine levels between 1660 and 1960 V. The HV level is usually fixed to the level which sets the energy range to 1.2 – 37 keV. The energy range can be extended up to 60 keV by setting the HV level down slightly.

The whole energy range is divided into 64 energy channels with equal width

Table 3.1: Data mode and time resolution of the LAC

Mode	PH	Bit rate			Note
		High	Medium	Low	
MPC1	48	500 ms	4 s	16 s	8 detectors by 2 layers
MPC2	48	62.5 ms	500 ms	2 s	4 detectors combined
MPC3	12	7.8 ms	62.5 ms	250 ms	8 detectors combined
PC-H		1.9 ms	15.6 ms	62.5 ms	4 detectors combined
-L		0.98 ms	7.8 ms	31.3 ms	4 detectors combined

by an analog to digital converter (ADC). The upper 32 channels are combined in pairs for storage and transmission. Signals from each counter and each layer are processed separately producing 16 spectra (8 counters × 2 layers) of 48 channels. These data are combined according to the data modes, which are MPC1, MPC2 and MPC3. Besides the MPC modes, there is a PC mode for timing studies. Characteristics of each mode are described below and listed in table 3.1.

MPC1 mode. This mode is mainly used for spectral study of faint sources. The 16 spectra of the 48 energy channels are output separately.

MPC2 mode. The two layers, both four of the eight counters are combined, thus the 16 spectra are summed up to two spectra. In exchange, time resolution improves by a factor of eight compared with MPC1 mode.

MPC3 mode. The two layers, the eight counters are combined and moreover, the 48 energy channels are combined to 12 channels. This improves time resolution by a factor of eight compared with MPC2 mode.

PC mode. The ADC is by-passed, thus dead time is reduced from 206 μsec to 16.5 μsec. The two layers, both four of the eight counters are combined into two detector groups. Signals are divided into two energy bands by three discriminators. Since the discriminator levels can be set for each of the two groups independently, four overlapping energy bands are available. The lower band of both groups is sampled twice as often as the upper one is, thus the maximum time resolution (0.98 msec) is attained in the band with greater signal to noise ratio.

3.3 Background in the LAC

Besides the diffuse X-ray background, background in the LAC is caused by cosmic rays, geometrically trapped charged particles, fluorescence of X-rays, radioactive decays, solar contamination and contamination from the bright limb of the Earth (Hayashida *et al.* 1989). The last two of these can be overcome by using only the data without the contaminations. The background caused by the geometrically trapped particles can be also eliminated by rejecting objectionable data with appropriate orbital criteria.

After the proper data selections, the background in the LAC is reproduced satisfactorily from the housekeeping or environmental parameters through a simple formula. The following formula was assumed and its coefficients were determined by independently fitting each energy channel to source free sky data (Hayashida *et al.* 1989);

$$C(E,t) = F_1(E) + \sum_{n=2}^{N} P_n(t) \times F_n(E), \tag{3.1}$$

where

$C(E,t)$ = LAC count rate (as a function of energy and time),
n = label of the component being fitted,
$P_n(t)$ = parameter (as a function of time) being fitted to the data,
$F_n(E)$ = the coefficients (as a function of energy) derived from the fit.

The time-independent component, $F_1(E)$, mainly corresponds to the diffuse X-ray background. As for the time-dependent parameters, the following four parameters are frequently used; the SUD rate, the COR related component, the MID rate and a component including the argument of perigee of the satellite orbit (Method II in Hayashida *et al.* 1989). The SUD rate is the count rate of X-ray-like events above the highest spectral channel (37 keV) of the LAC. It can be used as a measure of the internal background. The COR, which is the cutoff rigidity of charged particles, is an estimate of the momentum per elementary unit charge which a particle must have to penetrate from infinity to any given point in the Earth's magnetosphere. The MID rate is the middle layer count rate of the LAC in the 1– 5 keV range, which is an important measure of those background components which are not related to the instantaneous radiation environment. The

forth component describes variation of the altitude at which *Ginga* passes through the South Atlantic Anomaly. The altitude precesses in the 37-day period with the orbit.

The coefficients in the equation (3.1) were determined from frequent observations of the fixed part of the source-free sky near the Large Magellanic Cloud. The average of the time-independent component was determined from observations of high galactic sky positions (Hayashida *et al.* 1989).

Since the launch of *Ginga*, its altitude has been decreasing secularly and this affects the internal background in the LAC. Taking account of the secular change of the orbit, the background reproduction formula (3.1) was modified by Hayashida (1990). In the new formula, the time after the launch was adopted as the fifth parameter to describe the change of the orbit as well as the above four parameters. Hereafter in this thesis, I call the method of the background reproduction in Hayashida (1990) as the "Hayashida's method" for convenience.

The SUD and MID rate is almost uniquely determined as a function of orbital parameters of the satellite. Thus it is possible to estimate these values empirically from the orbital parameters alone. The MID rate is not available in MPC2 or MPC3 observations (see the previous section); the SUD rate can no longer be a measure of the internal background when the spectrum of the observing source is so hard that the hard X-rays come into it. In these situations, empirically estimated values for the SUD and MID rate are used in the formula (3.1) then Hayashida's method can be applied, although the reproduction of the background becomes less accurate than when real MID and SUD rates are used.

For the HV down observations, Hayashida's method cannot be applied at all since the accumulation of HV down data is very poor. In this case, background data should be taken with HV down mode with the same orbital conditions as the on-source observations.

3.4 Operations of Ginga

A command list for *Ginga* is created daily by duty scientists at ISAS in Sagamihara and sent to the ground station in KSC. The operations are performed at KSC according to the command list. *Ginga* can be contacted from KSC in 5 consecutive

revolutions out of 15 per day. During each contact, which is about 10 minutes, the necessary commands are sent to *Ginga* and at the same time real time data and stored data in BDR are transmitted from *Ginga*. Some of the commands (program commands, PC) are written in an on-board program timer. When the satellite is out of contact with KSC, it carries out observations according to the PC. Usually the ASM is operated once a day to monitor the sky by rotating the satellite. Data from *Ginga* are immediately transferred from KSC to ISAS through a digital line and stored in the ISAS computer system. The attitude of the satellite is determined at ISAS using STT and sun sensor data and then recorded in the computer system together with the original data.

Chapter 4

Observations

In table 4.1 – 4.10, the dates and modes of observations of all the X-ray sources involved in this thesis are listed. In order to investigate the energy spectra of the sources, I mainly use MPC1 and MPC2 data from the observations; PC or MPC3 observations I do not use are not listed in the tables. The following are comments on the individual observations.

4.1 Cyg X-1

Cyg X-1 was observed with the LAC in August 1987 and in May 1990; it was in the low state in both periods. In August 1987, major parts of the observations were performed with MPC3 and PC mode. Results of fast timing analyses of these MPC3 and PC observations have been published by Miyamoto *et al.* (1988) and Miyamoto and Kitamoto (1989). During the observation period, the intensity

Table 4.1: Cyg X–1: Observations in 1987

No.	Start m/d/y h:m	End m/d/y h:m	Exposure (sec)	Mode	Bit Rate
1	08/05/87 11:41	08/05/88 13:25	2620	MPC1/MPC2	H
2	08/05/87 18:31	08/05/87 18:41	580	MPC1	H
3	08/06/87 11:48	08/05/87 11:49	80	MPC1	H
4	08/08/87 12:04	08/08/87 12:43	1540	MPC2	H / M

Table 4.2: Cyg X-1: Observations in 1990[a]

No.	Start m/d/y h:m	End m/d/y h:m	Exposure (sec)	Mode	Bit Rate
1	05/10/90 10:18	05/10/90 10:30	736	MPC1	M
2	05/10/90 15:03	05/10/90 16:58	2048	MPC1	M
3	05/11/90 11:32	05/11/90 13:21	1824	MPC2	M

[a] HV down observations.

dips which are related to the orbital motion (see, e.g., Li and Clark 1974) were observed. I do not study the spectra during the dips; I select only MPC1 and MPC2 data avoiding apparent dips.

In May 1990, the source was observed with HV-low mode (see section 3.2), thereby the energy range was extended to 2 – 60 keV. Background data was taken at an adjacent sky position during the observation period. I selected only those on-source data which have corresponding background data with the same orbital conditions.

4.2 LMC X-3

Pointing observations of LMC X-3 were carried out once in January 1988 and about a dozen times from September 1989 to March 1990. Results of the observation in January 1988 were published by Treves *et al.* (1990) together with simultaneous UV and optical observations; in this thesis, results of reanalysis of these data are presented.

Besides these pointing observations, LMC X-3 was observed by scans and during attitude maneuvers of the satellite. The LMC region was frequently monitored in 1987 by scanning with the LAC in order to detect X-ray emissions from SN1987A. From March to May in 1987, LMC X-3 was scanned 9 times by chance. Among them, on 1 April 1987, the source was observed for about 1000 seconds with pointing mode at an extreme point of the scan. On 3 August in 1989 too, LMC X-3 was scanned four times with short intervals between scans. The scanning speed was normally 1°/minute and the typical exposure time per scan was

Table 4.3: LMC X-3: Pointing Observations

No.	Start m/d/y h:m	End m/d/y h:m	Exposure (sec)	Mode	Bit Rate
1	04/01/87 03:09	04/01/87 04:58	1076	MPC1	H
2	01/08/88 05:02	01/08/88 07:48	2604	MPC1	L
3	01/08/88 08:24	01/08/88 14:36	7292	MPC3	H
4	01/08/88 17:48	01/09/88 00:33	11456	MPC1	L
5	01/09/88 08:00	01/09/88 09:10	2382	MPC3	H
6	09/15/89 21:36	09/15/89 23:38	4012	MPC1	H / M
7	09/15/89 23:38	09/16/89 03:02	5656	MPC2	H
8	10/20/89 13:22	10/20/89 18:11	3712	MPC1	M / L
9	12/09/89 02:10	12/09/89 02:18	569	MPC3	H
10	12/09/89 03:44	12/09/89 06:19	2192	MPC1	H / M
11	12/14/89 04:29	12/14/89 05:27	960	MPC1	H / M
12	12/19/89 21:49	12/19/89 22:00	704	MPC1	M
13	12/21/89 00:06	12/21/89 01:04	800	MPC1	M
14	12/21/89 01:41	12/21/89 01:48	423	MPC3	H
15	12/26/89 18:53	12/26/89 20:39	952	MPC3	H / M
16	12/27/89 00:38	12/27/89 17:29	7056	MPC1	L
17	01/12/90 12:50	01/12/90 15:51	5508	MPC1	H / M
18	01/28/90 01:46	01/28/90 03:34	1612	MPC1	H
19	02/16/90 19:59	02/16/90 21:41	1241	MPC3	H
20	02/16/90 23:13	02/17/90 21:30	8576	MPC1	L
21	02/26/90 12:07	02/26/90 14:01	2480	MPC2	H / M
22	02/26/90 14:36	02/26/90 17:06	2420	MPC1	H / M
23	03/12/90 05:57	03/12/90 07:37	2348	MPC1	H / M
24	03/15/90 10:19	03/15/90 12:08	2790	MPC1	L
25	03/18/90 03:03	03/18/90 07:54	4544	MPC3	H
26	03/18/90 07:54	03/19/90 11:10	14316	MPC1	L

Table 4.4: LMC X-3: Scan Observations

No.	Start (UT) m/d/y h:m	End (UT) m/d/y h:m	Number of Scans	Transmission (maximum)	Mode
27	03/21/87 08:47	03/21/87 10:08	2	0.45	MPC1
28	03/26/87 09:02	03/26/87 09:04	1	0.66	MPC1
29	03/27/87 04:05	03/27/87 04:07	1	0.68	MPC1
30	04/01/87 03:16	04/01/87 05:27	4	0.85	MPC1
31	04/09/87 02:50	04/09/87 02:52	1	0.86	MPC1
32	04/10/87 02:44	04/10/87 02:46	1	0.91	MPC1
33	04/10/87 23:41	04/11/87 01:13	2	0.80	MPC1
34	05/01/87 12:39	05/01/87 13:22	2	1.00	MPC1
35	05/09/87 09:14	05/09/87 09:16	1	0.39	MPC1
36	08/03/89 17:13	08/03/89 20:37	4	0.53	MPC2

Table 4.5: LMC X-3: Maneuvering Observations

No.	Start m/d/y h:m	End m/d/y h:m	Exposure (sec)	Mode	Bit Rate
37[a]	03/12/88 01:45	03/12/88 03:32	1056	MPC1	H / M
38	07/07/88 13:11	07/07/88 13:12	64	MPC1	L
39	12/12/88 21:29	12/12/88 22:48	3008	MPC1	L

[a] Aproximately 500 sec is pointing.

Table 4.6: GS2000+25: Observations

No.	Start m/d/y h:m	End m/d/y h:m	Exposure (sec)	Mode	Bit Rates
1[a]	05/03/88 01:33	05/07/88 02:09	6912	MPC1/MPC2	H/M
2[a]	06/01/88 09:46	06/01/88 13:13	896	MPC1/MPC2	H
3[a]	06/26/88 22:28	06/27/88 00:13	256	MPC2	H
4	09/08/88 15:46	09/08/88 17:20	2560	MPC2	H
5	10/18/88 21:55	10/19/88 10:52	10752	MPC2	M / L
6	11/05/88 13:17	11/06/88 18:33	33280	MPC2	L
7[a]	12/07/88 21:57	12/09/88 10:56	5376	MPC2	M
8	12/16/88 11:09	12/16/88 22:34	4480	MPC1	H/M/L

[a] Data are fragmentary.

about 120 seconds.

On 12 March, 7 July and 12 Dec in 1988, LMC X-3 was in the LAC field of view during maneuvers of the satellite attitude. The speeds of the maneuvers were so slow that these data were treated as well as the pointing data for the spectral study.

4.3 GS2000+25

After the discovery by the ASM (section 2.4.5), GS2000+25 was observed by the LAC on eight occasions intermittently from 1988 May to 1988 December. In the meantime, the intensity of the source decreased by more than three orders of magnitude and therefore it was possible to study spectral evolutions over a large range of mass accretion rate.

The observations were performed using all the observational modes, but I adopt only MPC1 and MPC2 data for spectral study. Those MPC1 and MPC2 data scattered among other observations are combined in table 4.6.

A further observation was carried out on 15 May 1989, but the source was below the *Ginga* detection limit ($\sim$ 0.3 mCrab).

4.4 LMC X-1

Table 4.7: LMC X-1: Observations

No.	Start m/d/y h:m	End m/d/y h:m	Exposure (sec)	Mode	Bit Rate
1	04/22/87 22:56	04/23/87 12:48	9984	MPC1	L
2	07/16/87 04:18	07/16/87 11:22	12128	MPC2	M
3	09/30/87 15:17	10/01/87 06:28	12288	MPC1	L

Table 4.8: GX339–4: Observations in 1988

No.	Start m/d/y h:m	End m/d/y h:m	Exposure (sec)	Mode	Bit Rate
1	09/03/88 22:42	09/04/88 08:48	7808	MPC2	M
2	09/05/88 19:59	09/06/88 10:23	13184	MPC2	M
3	09/06/88 17:42	09/07/88 10:26	13792	MPC2	M

LMC X-1 was observed in April 1987, July 1987 and September 1987, each for about a day. In April 1987, before the MPC1 mode observation, a PC mode observation was carried out during which a QPO with a central frequency of 0.08 Hz was discovered (Ebisawa, Mitsuda and Inoue 1989). The energy spectra from April and July were published in Ebisawa, Mitsuda and Inoue (1989), but in this thesis I present results of reanalysis of these data.

4.5 GX339–4

GX339–4 was observed in September 1988, September 1989 and April 1990.

In September 1988, the source was in the high state. The intensity was $\sim$ 800 mCrab; this is the highest ever observed. The observation was carried out with

Table 4.9: GX339–4: Observations in 1989

No.	Start m/d/y h:m	End m/d/y h:m	Exposure (sec)	Mode	Bit Rate
1	09/28/89 15:23	09/28/90 20:23	4000	MPC2	H

Table 4.10: GX339–4: Observations in 1990[a]

No.	Start m/d/y h:m	End m/d/y h:m	Exposure (sec)	Mode	Bit Rate
1	04/07/90 16:25	04/07/90 18:16	3744	MPC1	M

[a] During an attitude maneurver.

MPC2, MPC3 and PC mode. I use only MPC2 data among them for spectral study. A $\sim$ 6 Hz QPO was discovered in the MPC3 and PC data (Makishima and Miyamoto 1988; Dotani 1988; Kitamoto 1989; Miyamoto, Kitamoto and Kimura 1989).

In September 1989, the intensity of the source was $\sim$ 15 mCrab, which corresponds to the low or off state. The observation was carried out with MPC2 and MPC3 mode. I adopt only those MPC2 data with the high bit rate. In April 1990, the source was observed by chance during slow maneuvering of the satellite. Since the speed of the maneuver is slow and the transmission is large enough ($\sim$ 40 %), these data can be used as well as the pointing data. The intensity was $\sim$ 100 mCrab; this corresponds to the low state.

Chapter 5

Analysis and Results

In this chapter, I present the analysis and results for the energy spectra of the black hole candidates Cyg X-1, LMC X-3, GS2000+25, LMC X-1 and GX339–4. In the analyses, I attempt to construct a unified spectral model to represent the energy spectra of all the sources. From previous studies by various authors, it is suggested that the energy spectrum of Cyg X-1 in its low state is approximated by a power-law function. On the other hand, that of ultra-soft sources is suggested to be represented by a two component model; i.e. a sum of an ultra-soft spectrum and a power-law like hard tail. I firstly study Cyg X-1 because the source was in the low state during the present observations when its spectrum is expected to be represented by a single component model. Then I proceed to the other sources, which turn out to have more complicated energy spectra. Among them, I firstly study LMC X-3; since the hard component of this source is weak and further it sometimes almost disappears, I can investigate the spectral shape of the soft component in detail. Then I analyze GS2000+25, whose hard component is strong compared to that of the other sources. Using this source, I study the spectral shape of the hard component in detail. From the analyses of these two sources, I construct a two component spectral model. Then this model is applied to the energy spectra of the remaining two sources.

5.1 Cyg X-1

5.1.1 Energy Spectra

From the observation in 1987, an energy spectrum was produced combining all the data in table 4.1. The background was subtracted using Hayashida's method (section 3.3) and the intensity reduction due to off-set of the pointing direction was corrected with the collimator response function of the LAC (section 3.2; see figure 3.4) [1]. For the observation in 1990, Hayashida's method cannot be used for the background subtraction since the observation was performed with HV-down mode (section 3.3). Therefore the background data taken at an adjacent sky position with the HV-down mode was directly subtracted from the on-source data. In this procedure, I selected on-source data and background data so that the net time and the orbital conditions of both data should be equivalent. All the data in table 4.2 are combined. The energy spectra of Cyg X-1 thus obtained are shown in figure 5.1.

Previous observations with *EXOSAT*, *Tenma* and other experiments suggested that the energy spectrum of Cyg X-1 in its low state is represented with a power-law plus an iron emission line (section 2.4.1). Therefore, firstly I tried fitting these two spectra with a power-law model. In the spectral fitting procedure, the interstellar photoelectric absorption model by Morrison and McCammon (1982) was adopted and the column density of neutral hydrogen to the source was allowed to be a free parameter. In the calculation of χ^2 values of the fits, systematic errors of one percent, which mainly originate in random errors of the ADC, are included for each energy channel [2]. The results with a power-law fit are shown in figure 5.2 and table 5.1. It is obvious that the model does not fit the spectra at all. In the residuals of the fits, a broad edge-like structure above ~ 7 keV is noticeable. Note that a similar structure has been found in the spectra of Seyfert 1 galaxies observed with *Ginga* (e.g., Pounds *et al.* 1989; Matsuoka *et al.* 1990; Piro *et al.* 1990).

[1] These procedures for the background subtraction and the aspect correction are adopted hereafter in this thesis except when noted otherwise.

[2] The same absorption model and the systematic errors are adopted in all the spectral fitting analyses in this thesis.

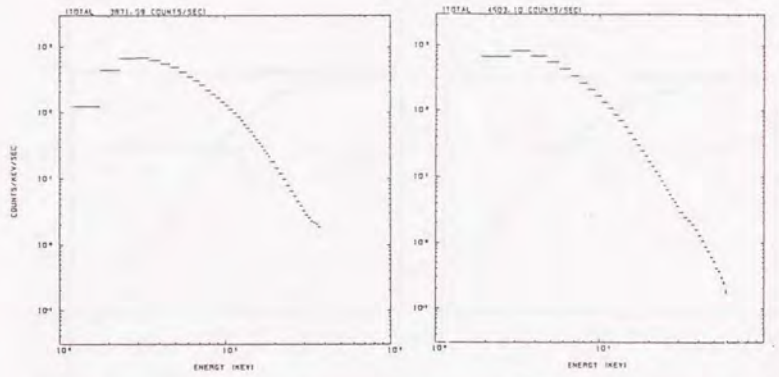

Figure 5.1: Energy spectra of Cyg X-1 in August 1987 (left) and in May 1990 (right). In the observation in May 1990, data was taken with HV-down mode so that the upper limit of the energy range is extended to 60 keV. The structure in the right panel at around 35 keV is due to K-edge of xenon in the counter gas.

Table 5.1: Cyg X-1: Spectral fitting with a power-law model[a]

Parameter	1987	1989
$N_{\rm power}$ [b]	1.29	1.62
photon index	1.50	1.52
$\log N_H(\rm cm^{-2})$	< 20	< 20
Reduced χ^2	17.1[c]	11.5[d]

[b] Photons $\rm s^{-1}\,cm^{-2}\,keV^{-1}$ at 1 keV.
[c] For 43 degrees of freedom.
[d] For 26 degrees of freedom.

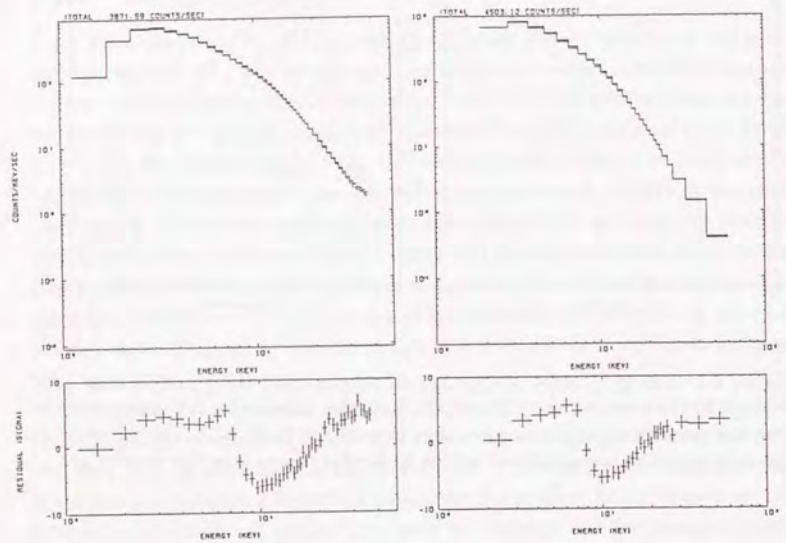

Figure 5.2: Fit with a power-law model to the spectra of Cyg X-1 in August 1987 (left) and in May 1990 (right). A broad edge-like structure above $\sim$ 7 keV is noticeable in both panels.

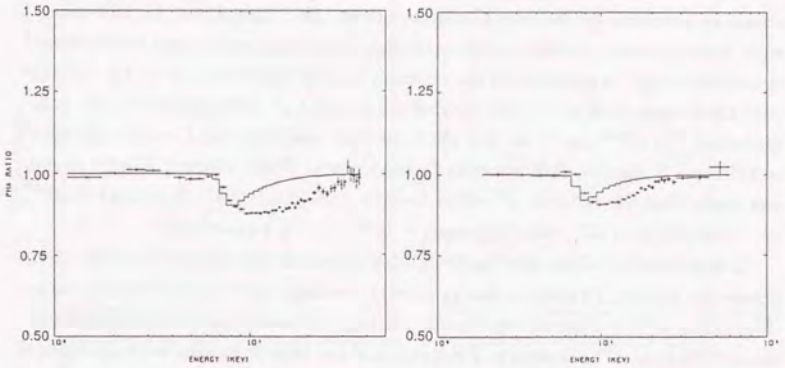

Figure 5.3: PHA ratios of the observed spectra of Cyg X-1 in August 1987 (left) and in May 1990 (right) to the power-law spectra (crosses with marks). The slopes of the power-law spectra were determined from the data by masking the 7 – 20 keV energy range. For comparison, the best-fit iron K-edge structures at 7.1 keV are shown together with histograms.

The broad edge-like structure extends from $\sim$ 7 keV to $\sim$ 20 keV and the residuals flatten above $\sim$ 20 keV. In the previous observations, the data above $\sim$ 20 keV were not available and therefore this structure could not be recognized. Since this structure was not taken into account in the previous spectral fitting analyses, the physical parameters of Cyg X-1 thus obtained are very doubtful. For a trial, I performed fitting of the spectrum in 1987 over 1.2 – 11.6 keV with a power-law plus an emission line; the central energy and the intrinsic width of the emission line were allowed to be free. I then found that the fit became acceptable ($\chi^2/12 = 0.60$); the best-fit photon index is 1.62, the central energy and FWHM of the emission line are 6.2 keV and 1.3 keV, respectively. These parameters of the emission line are comparable to those of the *EXOSAT* result by Barr *et al.* (1985). Therefore, I conclude that the broad emission line at 6.2 keV advocated by Barr *et al.* (1985) is an artifact due to the narrow energy range of their observation and missing the broad edge-like structure in 7 – 20 keV.

The fact that the K-edge of neutral iron is at 7.1 keV suggests that the observed

structure is related to the iron K-edge structure. So I then fitted the two spectra with a power-law including the iron K-edge absorption and found the observed structure cannot be modeled by the ordinary iron K-edge structure at all. The fits with the K-edge fixed at 7.1 keV yielded the reduced χ^2 values of 9.51 (d.o.f. = 42; N_H(edge) [3] = $10^{23.0}$ cm^{-2}) for the 1987 spectrum and 6.80 (d.o.f. = 25; N_H(edge) = $10^{22.9}$ cm^{-2}) for the 1990 spectrum, respectively. When the iron K-edge energy was made free, the reduced χ^2 values became 5.36 (d.o.f. =41; N_H(edge) = $10^{23.3}$ cm^{-2}) and 2.74 (d.o.f. =24; N_H(edge) = $10^{23.2}$ cm^{-2}), respectively.

In figure 5.3, I show the fractional deviations of the observed spectra from power-law models; I fitted the energy spectra masking the 7 – 20 keV energy range, then ratios of the observed spectra to the best fit power-law models (commonly called "PHA ratio") are shown. PHA ratios of the best-fit models with the neutral iron K-absorption to the power-law spectra are shown together for comparison; these clearly demonstrate that the observed edge-like structure is broader and/or shallower than usual K-absorption feature of iron.

The observed structure may be represented by several different model functions and may be interpreted by different physical models. In this chapter, however, I will attempt to construct a mathematical model to fit the broad edge-like structure by modifying the iron K-edge absorption structure. Possible physical mechanisms for yielding the broad edge-like structure will be discussed in the next chapter. In figure 5.3, it can be seen that the observed structure exhibits no absorption below about $\sim$ 7 keV. This means that absorption by electrons of the L-level or above is not necessary. Comparing the observed structure with the ordinary K-absorption by iron, the observed structure is found to be much broader. With these characteristics of the structure in mind, I construct a mathematical model, which hereafter is designated as "the smeared edge model" (appendix C). The free parameters of the smeared edge model are the energy of the edge ($E_{\rm edge}$), the hydrogen column density converted from that of iron assuming cosmic abundance (N_H(edge)) and the parameter which describes the degree of the smearing or how much the absorption is extended (E_W; see equation [C.4]). It should be remembered that values of these parameters obtained from spectral fitting are not necessarily related to any physical properties.

[3]The hydrogen column density converted from that of iron assuming cosmic abundance. The assumed cosmic Fe:H ratio is $10^{-4.4}$.

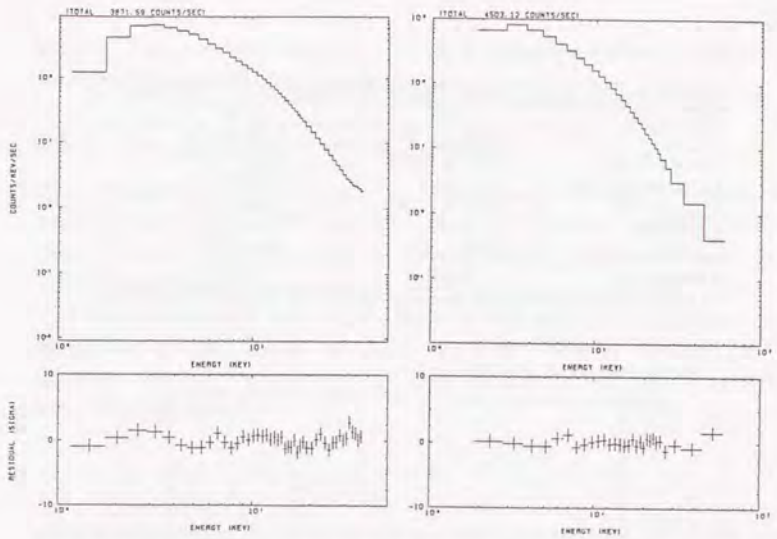

Figure 5.4: Fit with a power-law plus the smeared edge model to the spectra of Cyg X-1 in August 1987 (left) and in May 1990 (right).

The results of the fits with a power-law plus the smeared edge model are shown in figure 5.4 and table 5.2. For the spectrum in 1987, only the lower limits of the depth and the width of the smeared edge model are obtained, since these parameters are strongly correlated and the energy range is limited. In figure 5.5, the correlation of these two parameters are shown by a contour map. For the 1989 spectrum, the parameters are well determined because the energy range of this data extends up to 60 keV whereas that of 1987 spectrum extends only to 37 keV.

Adopting the smeared edge model, emission lines are not necessary to fit either spectra of Cyg X-1. However, this does not necessarily mean emission lines are not present at all in the spectra of Cyg X-1, since the parameters of emission lines strongly depend on modelling of the broad edge-like structure.

The origin of the broad edge-like structure in Cyg X-1, together with a possible

Table 5.2: Cyg X-1: Spectral fitting with the smeared edge model[a]

Parameter	1987	1989
$N_{\rm power}$ [b]	1.29 ± 0.02	1.76 ± 0.03
photon index	1.464 ± 0.006	1.530 ± 0.006
$\log N_H$(edge) ($\rm cm^{-2}$)	> 24.4	23.7 ± 0.2
$E_{\rm edge}$ (keV)	6.70 ± 0.16	7.04 ± 0.35
E_W (keV)	> 35	8^{+10}_{-4}
$\log N_H(\rm cm^{-2})$	20.4 ± 0.4	21.3 ± 0.2
Reduced χ^2	0.86[c]	0.47[d]

[a] Quoted uncertainties are single-parameter 90 % confidence limit.
[b] Photons $\rm s^{-1}\,cm^{-2}\,keV^{-1}$ at 1 keV.
[c] For 40 degrees of freedom.
[d] For 23 degrees of freedom.

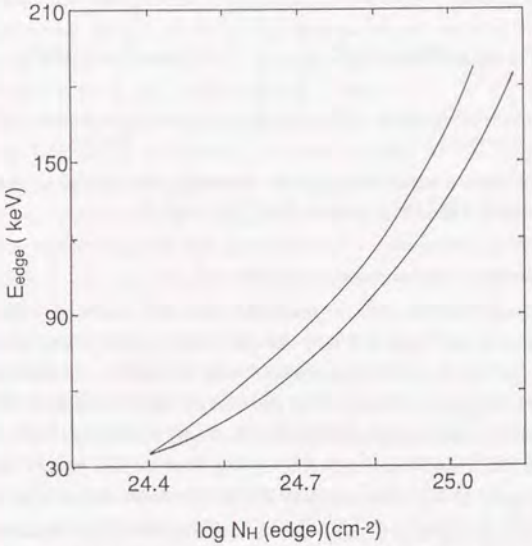

Figure 5.5: The contour map indicating the correlation between N_H(edge) and E_W, when the smeared edge model is applied to the spectrum of Cyg X-1 in 1987. The best fit is attained when N_H(edge) and E_W are effectively infinity. The contour indicates the 90 % confidence limit for the two parameters.

iron emission line, will be discussed in section 6.3 in terms of reflection and partial absorption by optically thick material.

5.1.2 Short Time Spectral Variation

Spectral variations of Cyg X-1 on a time scale of hours have been investigated for both the observations in 1987 and 1990. The source exhibited intensity variation of as much as $\sim$ 40 %, but significant spectral changes did not accompany these intensity variation.

I have studied short time spectral variation of Cyg X-1 on a time scale from seconds to minutes. To this end, I calculated the "fractional variation" of the spectrum. The fractional variation, F.V., of N bins of sequential data for a specified energy band is defined as [4],

$$\text{F.V.} \equiv \left\{ \frac{1}{N-1} \sum_{i=1}^{N} (x_i - \overline{x})^2 - \overline{x} \right\}^{1/2} \Big/ (\overline{x} - b)\,, \tag{5.1}$$

where x_i is counts in the i-th bin including the background, $\overline{x}\left(\equiv \sum_{i=1}^{N} x_i/N\right)$ is the average of the counts and b is the mean background counts per bin. The fractional variation represents the r.m.s. amplitude of intrinsic source variation normalized to the mean source intensity in the specified energy and frequency range.

In practice, in the calculation of the fractional variation of the time series, firstly the squares of the fractional variations are calculated every N bins, then the square root of their ensemble average is taken as the averaged fractional variation of the data. The errors of the resultant fractional variation are estimated by propagating Poisson errors of the data. The fractional variation itself shows time variations; however, I do not include these variations in the errors. The bin width τ and Nτ, determine the shortest and longest timescales respectively of variations included in the F.V.

[4] In the literature, F.V. is often defined as,

$$\text{F.V.} \equiv \left\{ \frac{1}{N} \sum_{i=1}^{N} (x_i - \overline{x})^2 - \overline{x} \right\}^{1/2} \Big/ (\overline{x} - b)\,.$$

This formula is not correct except when $(N-1)/N \approx 1$, since the F.V. thus defined does not become zero for the data which obey Poisson statistics.

For the data in 1987, the fractional variation was calculated over 0.5 – 256 sec (0.5 sec is the minimum time resolution of MPC 1 data. An N of 512 is used). Also for the data in 1990, the fractional variation was calculated over the same time interval for comparison by using only MPC2 data (No.3 in table 4.2).

The fractional variations in the whole energy ranges were 26.77 ± 0.04 % (1.2 – 37 keV) for 1987 and 20.13 ± 0.04 % (1.9 – 60 keV) for 1990. This large amplitude of the fluctuations is a characteristic of the low state of Cyg X-1 (section 2.4.1).

The energy dependence of the fractional variations is shown in figure 5.6 for 1987 and 1989 respectively. In both panels, it can be noticed that there is a minimum at an energy about 10 – 20 keV. The difference of the fractional variations on energies is at most ~ 4 % except for the lowest bin (1.2 – 1.8 keV) in 1987 data. The large variation in the lowest energy channel might be due to variations of the column density of the absorbing matter or another soft excess component (e.g., Balucinska and Hasinger 1989). I also notice that the F.V. value is larger for the 1987 data than for the 1990 data at any energy range. This indicates the long-term variation of the variation amplitude on 0.5 – 256 sec timescales.

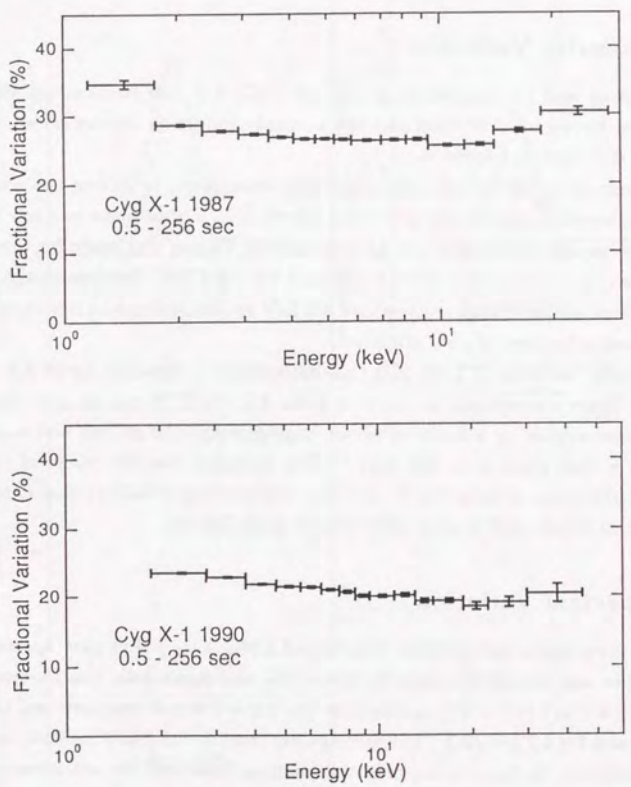

Figure 5.6: The fractional variations of Cyg X-1 in August 1987 and May in 1990.

5.2 LMC X-3

5.2.1 Intensity Variation

For the pointing and the maneuvering data of LMC X-3, the background was subtracted by Hayashida's method and the intensity reduction due to off-set of the pointing direction was corrected.

For the scan data, the source intensities were determined by fitting the scan profiles with the collimator response function (figure 5.7). Plural scans in a row in table 4.4 were superposed to give a single scan profile. Fitting was made for three energy bands (1.2 – 18.6 keV, 1.2 – 4.8 keV and 4.8 – 9.3 keV) independently. I tried fitting even in the energy range above 9.3 keV as well, but could not obtain significant results because of poor statistics.

The intensity variation of LMC X-3 thus determined is shown in figure 5.8; a point in the figure corresponds to a row in table 4.3 – 4.5. It can be seen that the source was variable by a factor of about four between ~10 mCrab and ~ 40 mCrab with a time scale of ~ 100 days [5]. The intensity and the range of the intensity variation are comparable to previous observations (Markert and Clark 1975; Johnston, Bradt and Doxsey 1979; Treves *et al.* 1988b).

5.2.2 Spectral Variation

In order to investigate the spectral variation of LMC X-3, I first plot spectral hardness ratios against the intensity. In figure 5.9a and figure 5.9b, the hardness ratio of 1.2 – 4.7 keV/4.7 – 9.3 keV against the 1.2 – 9.3 keV intensity and the hardness ratio 4.7 – 9.3 keV/9.3 – 18.6 keV against the 1.2 – 18.6 keV intensity are shown respectively. In figure 5.9b, only the pointing data and the maneuvering data with good statistics (No.37 and 39 in table 4.5) are adopted.

In figure 5.9a, a positive correlation between the intensity and the hardness ratio is clearly seen. One possible explanation for such a correlation is an optically thick emission whose emission temperature varies with the intensity. In fact in terms of the multicolor disk model (section 2.3.1; equation [2.7]), the correlation

[5] In the LAC, 1 count s^{-1} in 1.2 – 10 keV approximately corresponds to 0.1 mCrab.

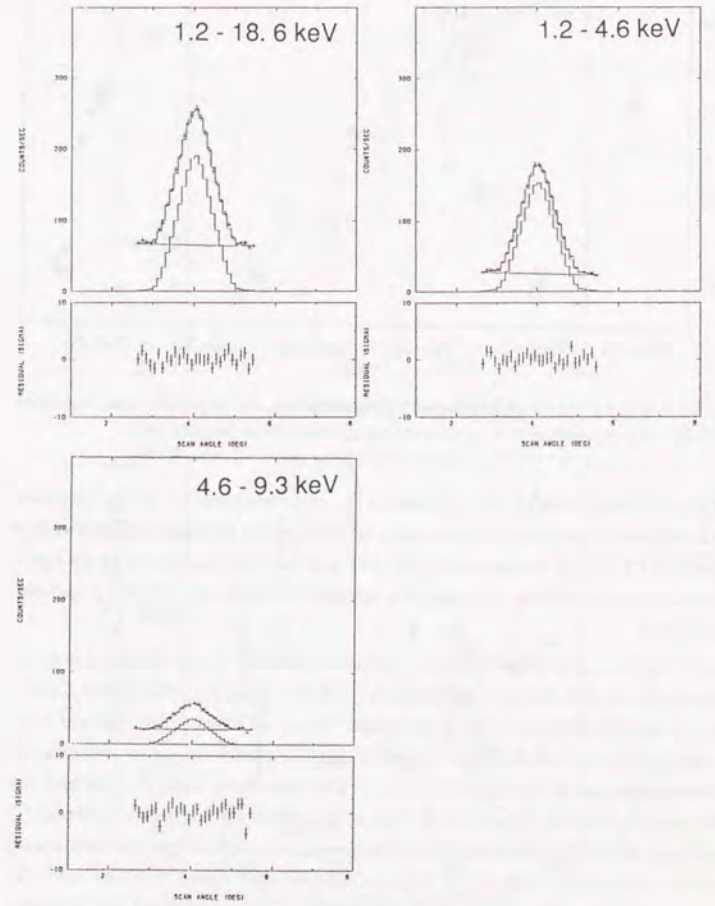

Figure 5.7: An example of the scan fitting for three energy bands; two scans are superposed (No.34 in table 4.4). The origin of the abscissa is arbitrary.

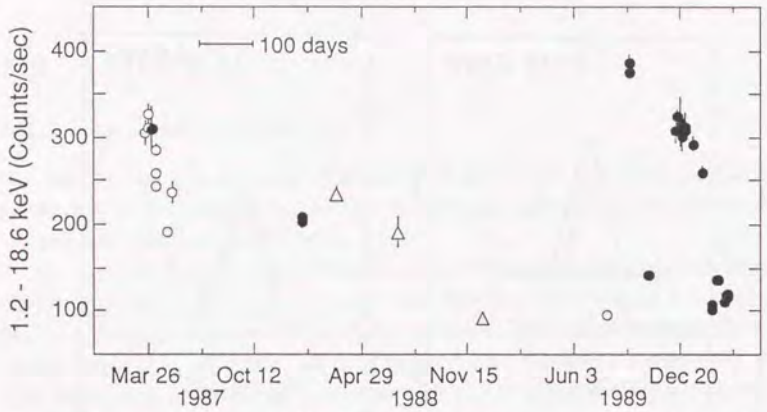

Figure 5.8: A light curve of LMC X-3. Filled circles, open circles and triangles denote pointing, scanning and maneuvering observations respectively.

can be interpreted as due to the variation in the color temperature of the accretion disk. I have shown the trace of the multicolor disk spectra with a fixed inner radius ($r_{in}\sqrt{\cos\theta}$=23.2 km at a distance of 50 kpc) and various temperatures in figure 5.9a; the curve successfully explains the relation between the intensity and the hardness ratio.

On the other hand in figure 5.9b, a clear correlation is not observed but the hardness ratio seems to vary independently of the intensity. In figure 5.9b, I plotted the hard hardness of the same model shown in figure 5.9a. Several data points are consistent with the model curve within 2 σ statistical errors, whereas all other data points are above the model curve. The correlation in figure 5.9a and the absence of a correlation in figure 5.9b lead to the following suggestive picture; (i) the spectrum of LMC X-3 consists of two components; *a soft component* and *a hard component*, which are respectively dominant below and above $\sim$ 9 keV and (ii) the spectrum of the soft component hardens with intensity whereas the intensity of the hard component is independent of that of the soft component. Note that the high energy excess in the spectrum of LMC X-3 has already been suggested by HEAO-1 A-2 results (White and Marshall 1984; see figure 2.6), though the statistics were not sufficiently good to ascertain it.

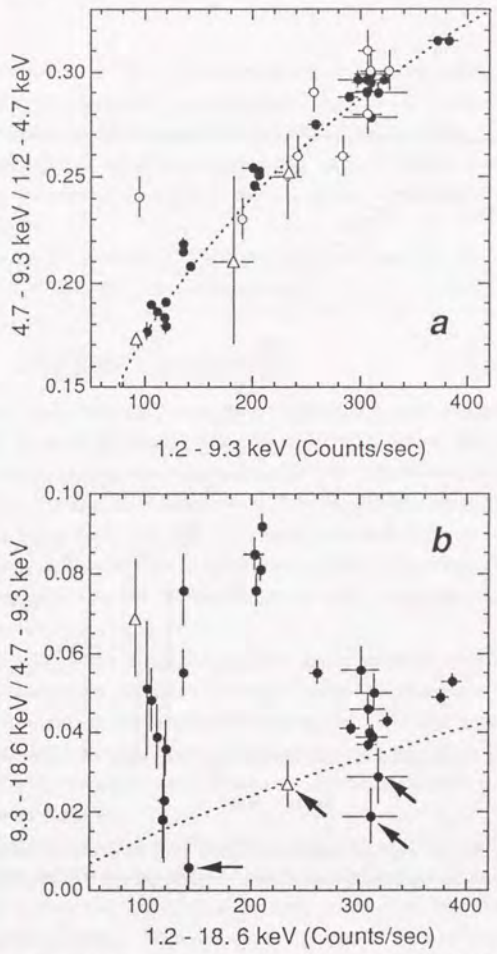

Figure 5.9: Intensity hardness diagrams of LMC X-3. Filled circles, open circles and triangles denote pointing, scanning and maneuvering data respectively. In figure (b), only the pointing data and the maneuvering data with good statistics (No.37 and 39 in table 4.5) are adopted. The error bars denote the 1 σ confidence limit. In both figures, the trace of multicolor disk spectra with variable temperature and a fixed inner radius ($r_{in}\sqrt{\cos\theta}$=23.2 km at a distance of 50 kpc) is indicated (dotted line). Data with arrows in (b) are used for the single component model fitting in section 5.2.3.

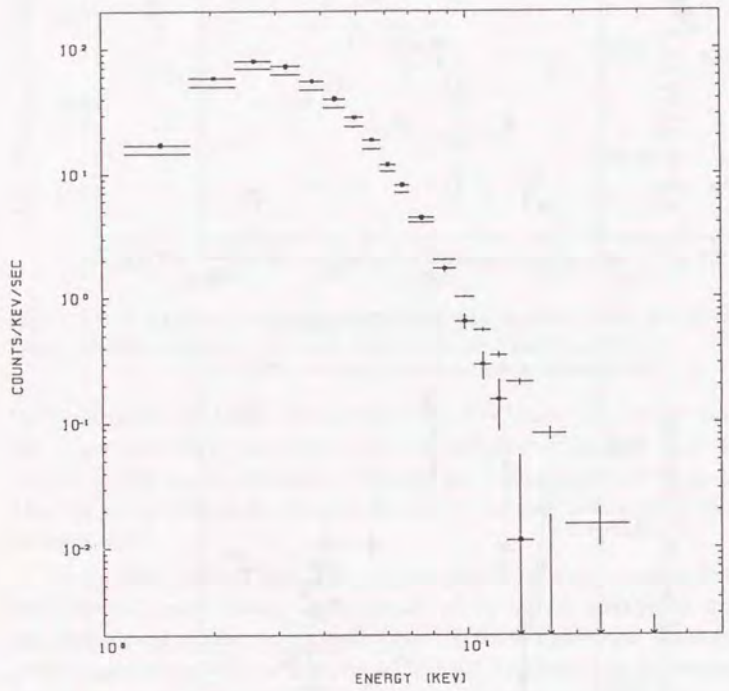

Figure 5.10: Pulse height energy spectra of LMC X-3 in January 1988 (crosses without marks; No. 4 in table 4.3) and in March 1988 (marked with dots; No. 37 in table 4.5).

The existence of the hard component and its independence of the soft component is directly recognized in the energy spectra. In figure 5.10, the spectra for January 1988 and for March 1988 are shown for contrast. The former spectrum clearly exhibits the hard excess extending up to $\sim$ 30 keV while on the other hand the latter does not show any hard excess, though the flux at lower energies is larger for the latter.

Below in this section, I investigate the spectrum of LMC X-3 with a working hypothesis of the two component model.

5.2.3 The Soft Component

If it were not for the hard component, the data points in figure 5.9b would be on the same trace of the multicolor disk spectra on which the data points in figure 5.9a are situated. Upward excursions of the data from the curve should be ascribed to variations of the hard component. The data with arrows in figure 5.9b (No. 1, 8, 12 and 27 in table 4.3 and 4.5) are considered to have very weak or no hard components since they are situated on or below the curve. Therefore, I adopted these four data sets for investigating the soft component and performed model fitting on them.

Suggested by the result in the previous subsection, which strongly hints that the soft component can be represented with the multicolor disk model, I fitted the four spectra by the multicolor disk model. The fits were performed over 1.2 – 18.6 keV and the results are tabulated in table 5.3. Note that the inner radius of the disk is virtually constant whereas the temperature varies according to the intensity, as expected.

For comparison, the results of fits with conventional models, namely a blackbody, a power-law and a thermal bremmstrahlung model are shown in table 5.4 to 5.6. It is seen that the multicolor disk model gives much better fits than these conventional models. However, three fits out of four still provide unacceptable values of reduced χ^2, larger than 1.44 which corresponds to a 90 % confidence level.

One might suppose that the deviations of the observed spectra from the multicolor disk model could be due to the hard component, which is very weak and

Table 5.3: LMC X-3: Spectral fitting with the multicolor disk model[a]

Parameter	1987 Apr. (No.1)	1988 Mar. (No.27)	1989 Oct. (No.8)	1989 Dec. 19 (No.12)
Scale[b]	24.6 ± 0.5	23.7 ± 0.4	22.2 ± 0.5	24.0 ± 0.5
T_{in} (keV)	1.191 ± 0.009	1.143 ± 0.008	1.066 ± 0.008	1.213 ± 0.010
$\log N_H(\mathrm{cm}^{-2})$	< 20.7	< 20.3	< 20.7	< 20.5
Reduced $\chi^{2\,c}$	2.36	3.74	1.76	1.35

[a] Quoted uncertainties are single-parameter 90 % confidence limit.
[b] $r_{in}(\cos\theta)^{1/2}$ in units of km at an assumed distance of 50 kpc.
[c] For 18 degrees of freedom.

Table 5.4: LMC X-3: Spectral fitting with a blackbody model[a]

Parameter	1987 Apr. (No.1)	1988 Mar. (No.27)	1989 Oct. (No.8)	1989 Dec. 19 (No.12)
Scale[b]	64.1	59.5	51.9	63.2
Temp. (keV)	0.810	0.789	0.760	0.821
$\log N_H(\mathrm{cm}^{-2})$	< 20.0	< 19.8	< 19.7	< 20.1
Reduced $\chi^{2\,c}$	47.86	64.57	76.00	35.85

[a] Quoted uncertainties are single-parameter 90 % confidence limit.
[b] An effective blackbody radius in units of km at an assumed distance of 50 kpc.
[c] For 18 degrees of freedom.

Table 5.5: LMC X-3: Spectral fitting with a power-law model[a]

Parameter	1987 Apr. (No.1)	1988 Mar. (No.27)	1989 Oct. (No.8)	1989 Dec. 19 (No.12)
Scale[b]	4.33	3.55	4.55	4.53
Photon index	3.88	3.95	4.44	3.87
$\log N_H(\mathrm{cm}^{-2})$	22.490	22.469	22.565	22.510
Reduced $\chi^{2\,c}$	33.56	41.95	67.22	30.85

[a] Quoted uncertainties are single-parameter 90 % confidence limit.
[b] In units of photons $\mathrm{s}^{-1}\,\mathrm{cm}^{-2}\,\mathrm{keV}^{-1}$ at 1 keV.
[c] For 18 degrees of freedom.

Table 5.6: LMC X-3: Spectral fitting with a thermal bremmstrahlung model[a]

Parameter	1987 Apr. (No.1)	1988 Mar. (No.27)	1989 Oct. (No.8)	1989 Dec.19 (No.12)
Scale[b]	81.6	63.8	56.2	83.4
Temp. (keV)	2.26	2.18	1.84	2.29
$\log N_H(\mathrm{cm}^{-2})$	21.96	21.87	22.04	21.99
Reduced $\chi^{2\,c}$	4.40	5.31	4.27	4.96

[a] Quoted uncertainties are single-parameter90 % confidence limit.
[b] Emission measure in units of $10^{60}\mathrm{cm}^{-3}$ at an assumed distance of 50 kpc.
[c] For 18 degrees of freedom.

not conspicuous above $\sim$ 9 keV but still affects the spectral shape significantly. In order to examine this possibility, I tried to include the hard component in the fits. As will be discussed in section 5.2.5, the hard component of LMC X-3 can be represented by a power-law function for the first approximation; therefore I tried two component fitting with the multicolor disk plus a power-law to those four spectra. The two component model actually yielded acceptable fits; however, the photon-index of the power-law component became as large as 3 – 4. As will be shown in the later sections, variation in the slope of the hard component of various sources is not large; it is held, for example for GS2000+25, between 1.7 – 2.5 over the wide range of intensity change. The photon index of the hard component of LMC X-3 is determined to be 2.21 when it is strong (section 5.2.5). If the stability in the photon index holds also for LMC X-3, the value of 3 – 4 is not expected for the hard component. If then the photon-index was fixed to 2.21, the spectra were fitted well below $\sim$ 9 keV, but the hard component yielded significantly larger flux than observed above $\sim$ 9 keV. Therefore the deviations from the multicolor disk model are not likely to be ascribed to the other components, but they probably mean that the multicolor disk model is not adequate enough for the soft component.

Hence I next tried fitting those four spectra with more sophisticated models of accretion disks; the General Relativistic Accretion Disk model (hereafter abbreviated to the GRAD model; see appendix D; Hanawa 1989; Ebisawa, Mitsuda and Hanawa 1991) and the Comptonization model by Sunyaev and Titarchuk (1980)

(section 2.4.1, equation [2.10]).

The GRAD model is a model of X-ray emission from geometrically thin and optically thick accretion disks around compact objects taking account of general relativity. In other words, it is a multicolor disk model modified by corrections due to general relativity. In the GRAD model, the inclination angle of the disk to the line of sight, i, is one of the free parameters. When the inclination angle is small enough, $i \sim 0°$, the spectral shape of the GRAD model differs little from that of the multicolor disk model. However, as the inclination angle becomes larger ($i \gtrsim 30°$), the deviation between the GRAD model and the multicolor disk model becomes noticeable (Ebisawa, Mitsuda and Hanawa 1991; see figure D.2) owing to relativistic effects such as Doppler boosting and gravitational bending of the light (cf. Luminet 1979; Fukue and Yokoyama 1988).

In the GRAD model, five unknown parameters are included; the mass of the compact object, M, the mass accretion rate, $\dot{M}$, the distance to the source, d, the inclination angle of the disk to the line of sight, i, and the ratio of the color to the effective temperature of the optically thick emission at the disk surface, T_{col}/T_{eff}. In the present fits with the GRAD model, I fixed the distance to the source to 50 kpc (Stothers 1983, 1987). The inclination angle cannot be determined uniquely from the spectral fitting because of the strong interdependence among the parameters, so that I tentatively assumed it to be 60°. This value is plausible since it is close to the value obtained by Treves *et al.* (1988a) from UV observations ($\sim$ 55°) and also near to the average of the inclination angles of randomly distributed accretion disks (57.3°) [6].

In the GRAD model, it is assumed that the radius of the inner edge of the accretion disk is three times the Schwarzschild radius. Hence the inner radius of the accretion disk, $r_{in}\,(\cos\theta)^{1/2}$, is determined by M (equation [D.6]) and the maximum color temperature of the disk is determined by both M and $\dot{M}$ with the aid of the color to effective temperature ratio. I fixed the ratio to 1.5 (see appendix D). The free parameters of the fits are thus reduced to M and $\dot{M}$. The mass accretion rate is related to the multicolor disk parameters by $\dot{M} \propto {r_{in}}^2 {T_{in}}^4$ (see equation [2.9] and [D.2]).

[6] This is derived as, $\langle\,\theta\,\rangle = \int_0^{\frac{\pi}{2}} \theta\,\sin\theta\,d\theta / \int_0^{\frac{\pi}{2}} \sin\theta\,d\theta = 1(radian) = 57.3°$.

Table 5.7: LMC X-3: Spectral fitting with the GRAD model[a]

Parameter	1987 Apr. (No.1)	1988 Mar. (No.27)	1989 Oct. (No.8)	1989 Dec. 19 (No.12)
$M\,(M_\odot)$	4.95 ± 0.18	4.65 ± 0.09	4.91 ± 0.12	4.90 ± 0.20
$\dot{M}\,(10^{18}\mathrm{g\,s^{-1}})$	6.57 ± 0.14	5.07 ± 0.05	3.65 ± 0.08	6.78 ± 0.16
$\log N_H(\mathrm{cm^{-2}})$	21.0 ± 0.3	< 20.5	21.4 ± 0.1	21.1 ± 0.3
Reduced χ^2 [b]	1.45	1.01	0.35	1.30

[a] Quoted uncertainties are single-parameter 90 % confidence limit.
[b] For 18 degrees of freedom.

Table 5.8: LMC X-3: Spectral fitting with the Comptonization model[a]

Parameter	1987 Apr. (No.1)	1988 Mar. (No.27)	1989 Oct. (No.8)	1989 Dec. 19 (No.12)
Scale[b]	12.1 ± 1.7	11.0 ± 1.4	6.8 ± 0.8	15.5 ± 2.9
T_e (keV)	1.15 ± 0.03	1.10 ± 0.03	1.04 ± 0.02	1.11 ± 0.04
τ_e	26.0 ± 2.0	28.5 ± 2.5	24.0 ± 1.2	30.5 ± 4.9
$\log N_H(\mathrm{cm^{-2}})$	21.8 ± 0.1	21.5 ± 0.2	21.95 ± 0.05	21.6 ± 0.2
Reduced χ^2 [c]	1.33	0.67	0.45	1.22

[a] Quoted uncertainties are single-parameter 90 % confidence limit.
[b] In a unit of 10^{-3} photons $\mathrm{s^{-1}\,cm^{-2}\,keV^{-1}}$.
[c] For 17 degrees of freedom.

The GRAD model could fit all the four spectra satisfactorily (table 5.7). In figure 5.11, an example of the fit with the GRAD model is shown together with the fit with the multicolor disk model for comparison; significant improvement in the former fit can be seen. The success of the GRAD model, together with the failure of the multicolor disk model, suggests that the edge-on configuration is preferred to the face-on one and that the relativistic effects are essential in understanding the X-ray spectrum of LMC X-3 in this context.

The Comptonization model of the form of equation (2.10) was used by Treves *et al.* (1988b) to fit the spectrum of LMC X-3 taken by *EXOSAT* (section 2.4.2). It was also used for Cyg X-1 in its low state (section 2.4.1) and has been widely used for LMXBs (section 2.3.1).

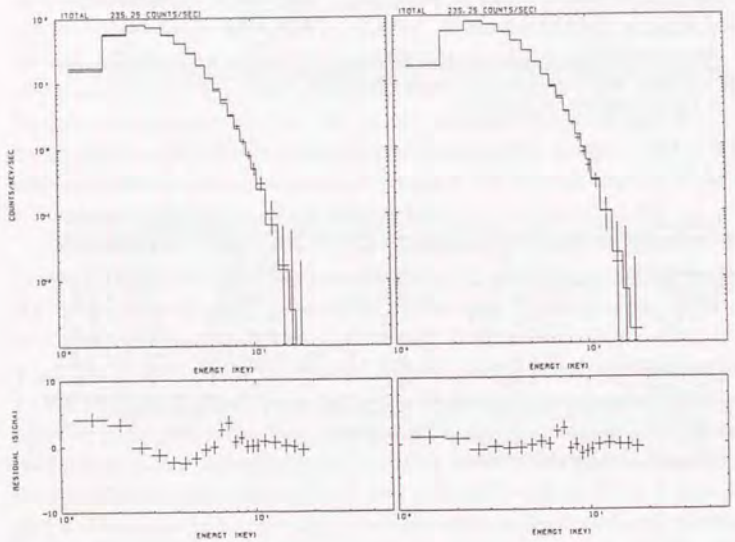

Figure 5.11: Results of spectral fitting for the spectrum in March 1988 (No. 37 in table 4.5) with the multicolor disk model (left) and the GRAD model (right).

The Comptonization model also gives good fits to the four spectra of LMC X-3 (table 5.8). The free parameters are N, kT_e and τ_e. Note that the number of free parameters is larger by one than that of the multicolor disk model and the GRAD model. The best fit values of the parameters are comparable to those by Treves *et al.* (1988b).

Solely from the results of the spectral fitting, it is impossible to give preference for either the GRAD model or the Comptonization model since both of them yield satisfactory fits. As a matter of fact, the spectral shapes of themselves are very similar to each other (Ebisawa, Mitsuda and Hanawa 1991). However, on the following physical bases, I assert that the GRAD model should be favoured.

Firstly, the GRAD model has solid physical grounds; the assumption of the optically thick accretion disk is reasonable and the physical meanings of GRAD parameters are very clear. On the other hand in the Comptonization model, the ad hoc configuration that the soft photon sources are surrounded by or embedded in the plasma is *apriori* assumed without any physical bases. Furthermore, the origin of the soft photons is unknown and the necessary condition for the plasma, that it be Thomson thick ($\tau_{sct} \sim 30$) as well as effectively thin for absorption ($\tau_{eff} \equiv \sqrt{\tau_{sct}\tau_{abs}} \ll 1$), seems artificial.

Secondly, the observed intensity-hardness relation of the soft component (figure 5.9a) is naturally understood in terms of the GRAD model as constancy of the mass of the compact object and variation of the mass accretion rate (table 5.7). This is very reasonable and strongly supports the GRAD interpretation of the spectrum. Note the large mass of the compact object ($\sim 5M_\odot$) obtained from the GRAD model fitting. This is in favor of the argument that the compact object in LMC X-3 is a black hole (cf. appendix A). On the other hand, in the Comptonization model, the color intensity correlation is realized by a complicated correlation among the three free parameters (table 5.8).

One might argue that the mass of the compact object obtained from the GRAD model fitting ($\sim 5M_\odot$) is not consistent with the definite lower limit of the mass ($9 - 10M_\odot$; Cowley *et al.* 1983; Paczyński 1983) which has been established by optical spectroscopy. However, the difference is not serious. This issue is discussed later in section 6.2 together with the masses of the compact objects in other black hole candidates.

5.2.4 The Hard Component

Since the soft component of LMC X-3 was successfully explained by the GRAD model, the next step is to investigate the nature of the hard component.

The residual of an observed spectrum after subtracting the soft component is considered to be the hard component (cf. figure 5.9b). In order to make the subtraction properly, I adopted the following procedure for the analysis: (i) fit the lower energy part (from 1.2 keV to E_S, which is a variable) of an observed spectrum with the GRAD model (i is fixed to 60°); (ii) try several values of E_S within 4 keV $\lesssim E_S \lesssim$ 9 keV and take the residual of the fit for each E_S; (iii) if there is a certain energy, say E_H ($E_S < E_H$), above which the residual does not depend on E_S, the residual above E_H will represents the hard component. Note that the spectral shape of the hard component below E_H is hardly determined since it is more or less overshadowed by the soft component.

I made the above analysis on the spectrum of January 1988 (No. 4 in table 4.3), in which the hard component is most prominent of all the spectra. The residual of the spectrum is shown in figure 5.12 for those E_S which are varied from 4.7 keV to 8.1 keV. The residual above $\sim$ 15 keV, which is represented by the power-law with a photon-index of $\sim$ 2.5, is found to be independent of E_S and thus can be considered to well represent the hard component. Below $\sim$ 15 keV, the spectral shape of the hard component cannot be determined since the residual depends considerably on E_S, but the residual bends and deviates from the power-law always at around 15 keV irrespective of E_S. This suggests that the bending is a real feature of the hard component. It is, however, impossible to further discuss here the possible deviation of the hard component from a power-law because of the limited statistics of LMC X-3. A similar deviation of the hard component from the power-law function will be found again for GS2000+25 more clearly in the next section; its characteristics will be extensively studied there.

The same analysis was applied to other spectra, but I could not obtain significant results because the hard components are too weak and/or the statistics are not sufficiently good.

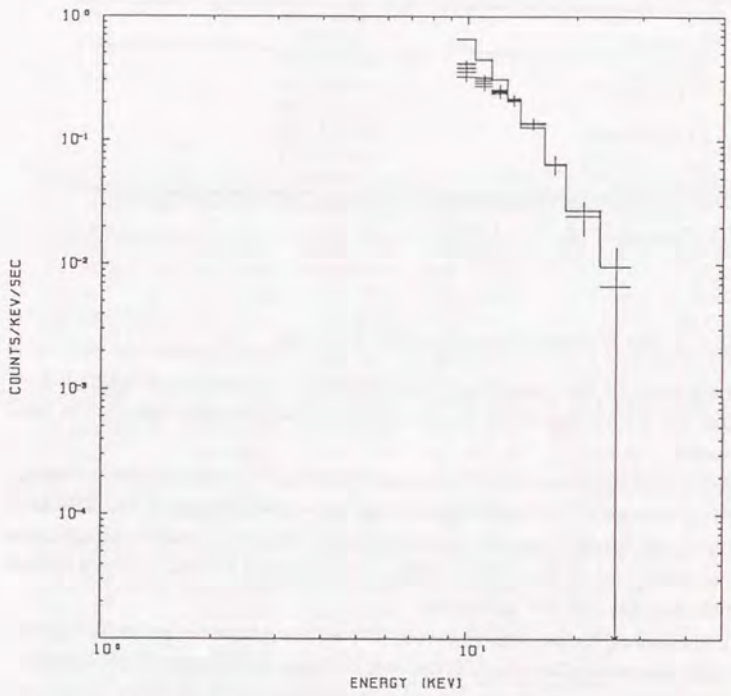

Figure 5.12: Residual of the spectrum in January 1988 (No. 4 in table 4.3) after fitting the lower energy part (1.2 - E_S keV) with the GRAD model. E_S is varied from 4.7 keV to 8.1 keV. The power-law with a photon-index of 2.5 is shown together for comparison.

Table 5.9: LMC X-3: Spectral fitting with the GRAD plus power-law model[a]

Parameter	1988 Jan. (No.4)
M ($M_\odot$)	5.02 ± 0.05
$\dot{M}$ (10^{18}g s^{-1})	4.45 ± 0.04
$N_{\rm power}$ [b]	0.65 ± 0.02
Photon index	2.21 ± 0.09
$\log N_H$(cm^{-2})	21.2 ± 0.1
Reduced χ^2 [c]	0.58

[a] Quoted uncertainties are single-parameter 90 % confidence limit.
[b] Photons s^{-1} keV^{-1} at 10 keV.
[c] For 19 degrees of freedom.

5.2.5 Two Component Model Fitting

Next I performed two component model fitting to the spectra of LMC X-3. I adopted the GRAD model for the soft component and a power-law for the hard component.

Firstly I fitted the spectrum in January 1988 (No. 4 in table 4.3) in the energy range 1.2 – 28 keV. The result is shown in table 5.9 and figure 5.13. The fit is completely acceptable; however, in the residuals of the fit, a small waving feature is recognized around 10 to 15 keV. This may correspond to the bending feature mentioned in the previous subsection.

In the fitting for the other spectra, I fixed the photon index of the power-law component to 2.21, which is the best fit value for January 1988 spectrum, since the hard components are not strong enough for the index to be determined uniquely. The fits were made for all MPC1 spectra in 1.2 – 18.6 keV; the results are tabulated in table 5.10. Among them, the fits for Sep. 1989 (No.6 in table 4.3) and Dec.27 1989 (No.16 in table 4.3) yield unacceptably large χ^2 values. These can be considered to be due to the deviation from the power-law function suggested in the previous subsection. In the residual of the two-component fits (figure 5.14b), these deviations appear as edge-like structures between 7 – 15 keV. If the smeared edge model, which was introduced in section 5.1.1 to explain the broad edge-like structure of Cyg X-1, is included in the hard component, the structures are

Table 5.10: LMC X-3: Spectral fitting with the GRAD plus power-law model[a]

Parameter	1988 Jan. (No.2)	1988 Dec. (No.39)	1989 Sep. (No.6)	1989 Dec. 9 (No.10)	Dec. 14 (No.11)
M ($M_\odot$)	4.98 ± 0.20	5.43 ± 0.34	5.27 ± 0.12	5.00 ± 0.10	4.99 ± 0.15
$\dot{M}$ (10^{18}g s^{-1})	4.25 ± 0.08	2.45 ± 0.09	8.65 ± 0.11	7.06 ± 0.11	7.38 ± 0.16
$N_{\rm power}$ [b]	0.73 ± 0.06	0.16 ± 0.04	0.25 ± 0.06	< 0.04	0.05 ± 0.09
$\log N_H$(cm^{-2})	21.3 ± 0.1	21.3 ± 0.2	21.6 ± 0.1	21.4 ± 0.1	21.4 ± 0.1
Reduced χ^2 [c]	1.01	1.39	2.48	0.84	1.14

Parameter	Dec. 21 (No.13)	Dec. 27 (No.16)	1990 Jan. 12 (No.17)	Jan. 28 (No.18)	Feb. 16 (No.20)
M ($M_\odot$)	4.88 ± 0.06	5.03 ± 0.05	4.96 ± 0.11	5.09 ± 0.17	5.33 ± 0.21
$\dot{M}$ (10^{18}g s^{-1})	7.07 ± 0.07	7.17 ± 0.03	6.69 ± 0.09	5.83 ± 0.11	2.86 ± 0.08
$N_{\rm power}$ [b]	< 0.06	0.04 ± 0.03	0.07 ± 0.05	0.39 ± 0.07	0.18 ± 0.02
$\log N_H$(cm^{-2})	21.5 ± 0.1	21.5 ± 0.1	21.4 ± 0.1	21.5 ± 0.1	21.5 ± 0.1
Reduced χ^2 [c]	1.05	2.66	0.77	1.47	0.98

Parameter	Feb. 26 (No.22)	Mar. 12 (No.23)	Mar. 15 (No.24)	Mar. 18 (No.26)
M ($M_\odot$)	5.07 ± 0.20	5.38 ± 0.23	5.06 ± 0.13	5.16 ± 0.14
$\dot{M}$ (10^{18}g s^{-1})	3.38 ± 0.12	3.01 ± 0.08	2.91 ± 0.05	3.10 ± 0.06
$N_{\rm power}$ [b]	0.25 ± 0.04	0.13 ± 0.04	0.06 ± 0.05	0.10 ± 0.02
$\log N_H$(cm^{-2})	21.5 ± 0.1	21.4 ± 0.1	< 20.6	21.2 ± 0.1
Reduced χ^2 [c]	0.80	0.58	0.84	0.85

[a] Quoted uncertainties are single-parameter 90 % confidence limit.
[b] Photons s^{-1} keV^{-1} at 10 keV.
[c] For 17 degrees of freedom.

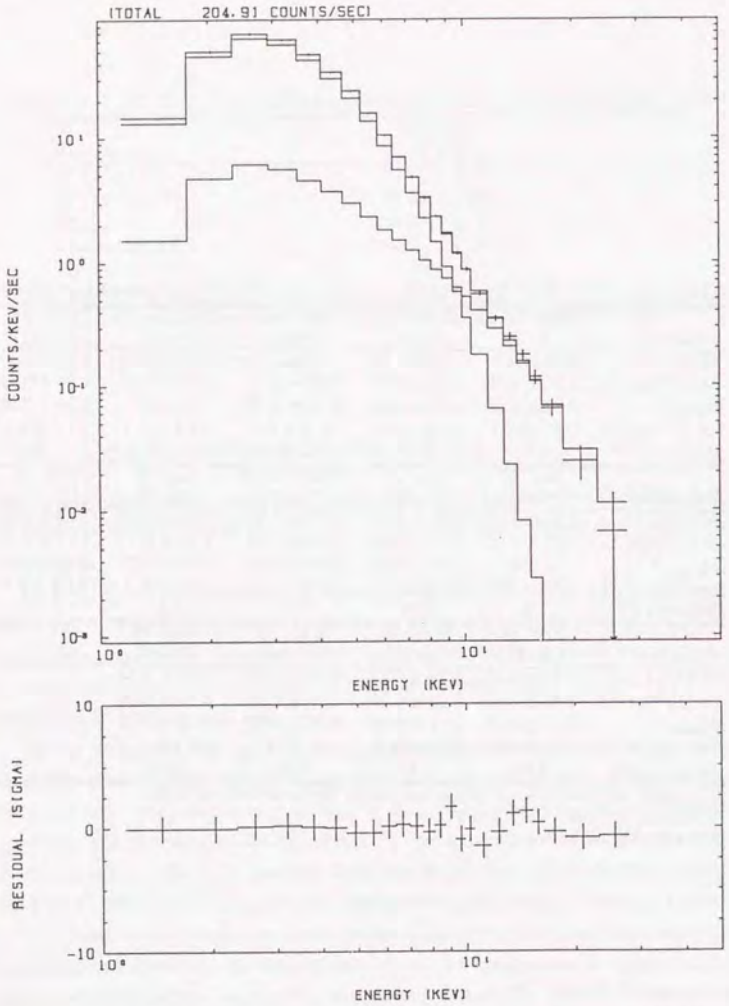

Figure 5.13: The two component fit for the spectrum in January 1988 (No. 4 in table 4.3) with the GRAD plus a power-law model.

Table 5.11: LMC X–3: Spectral fitting with the smeared edge model[a]

Parameter	1989 Sep. (No.6)	1989 Dec. 27 (No.16)
M ($M_\odot$)	5.12 ± 0.06	4.93 ± 0.07
$\dot{M}$ (10^{18}g s^{-1})	8.11 ± 0.09	6.80 ± 0.05
$N_{\rm power}$ [b]	0.95 ± 0.10	0.50 ± 0.07
$\log N_H$(edge) (cm^{-2})	24.77 ± 0.09	24.96 ± 0.12
$E_{\rm edge}$ (keV)	7.0 ± 0.2	7.2 ± 0.2
E_W (keV)	7.8 ± 2.1	6.8 ± 2.6
$\log N_H$(cm^{-2})	21.6 ± 0.1	21.5 ± 0.1
Reduced χ^2 [c]	0.22	0.61

[a] Quoted uncertainties are single-parameter 90 % confidence limit.
[b] Photons s^{-1} keV^{-1} at 10 keV.
[c] For 14 degrees of freedom.

cancelled out and the fits become totally acceptable (figure 5.14c; table 5.11).

The results of the two component fit for LMC X-3 are summarized in figure 5.15. I point out several noticeable facts in this figure. Firstly, the mass of the compact object is remarkably constant; this strongly supports the GRAD interpretation of the soft component of the spectrum. The constant mass of $5.0M_\odot$ is equivalent to the inner radius of the disk being constant at 45 km ($\equiv$ three times the Schwarzschild radius of $5.0M_\odot$ compact object). Secondly, the hard component shows large intensity variations of at least one order of magnitude while the variation in the soft component is at most a factor of four. Thirdly, the luminosity of the soft component and that of the hard component are not correlated. This fact leads to the curious conclusion that the luminosity of the hard component is not related to the mass accretion rates since the luminosity of the soft component is considered to be related to the accretion rate. This issue will be discussed later in section 6.4.

5.2.6 Short Time Spectral Variation

Throughout the observations, LMC X-3 did not show significant intensity nor spectral variations within a day. The typical intensity change within a day is less

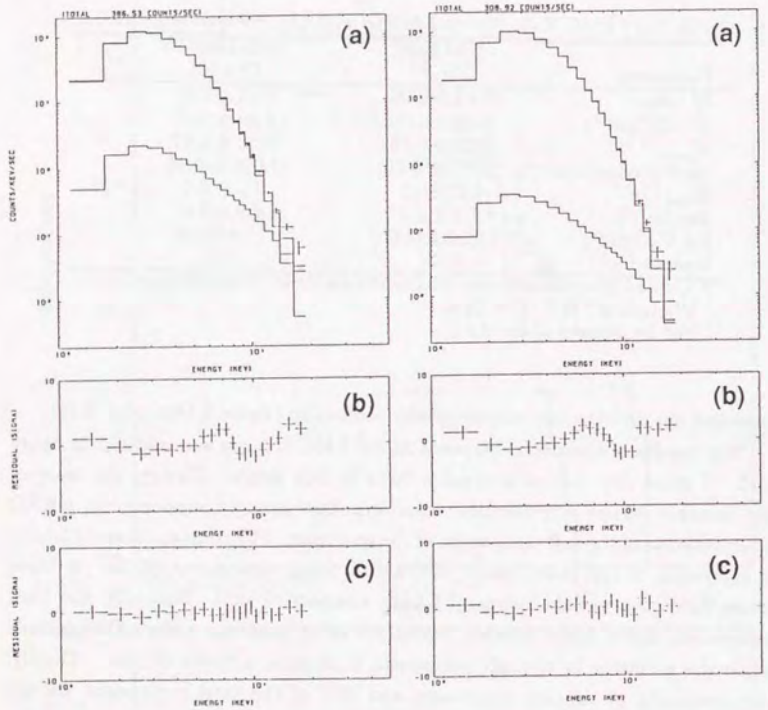

Figure 5.14: The two component fits for the spectra in Sep. 1989 (left; No. 6 in table 4.3) and Dec. 27 1989 (right; No. 16 in table 4.3). (a) Fit with the GRAD plus power-law model and (b) its residual. (c) The residual of the fit with the smeared edge model in the power-law component.

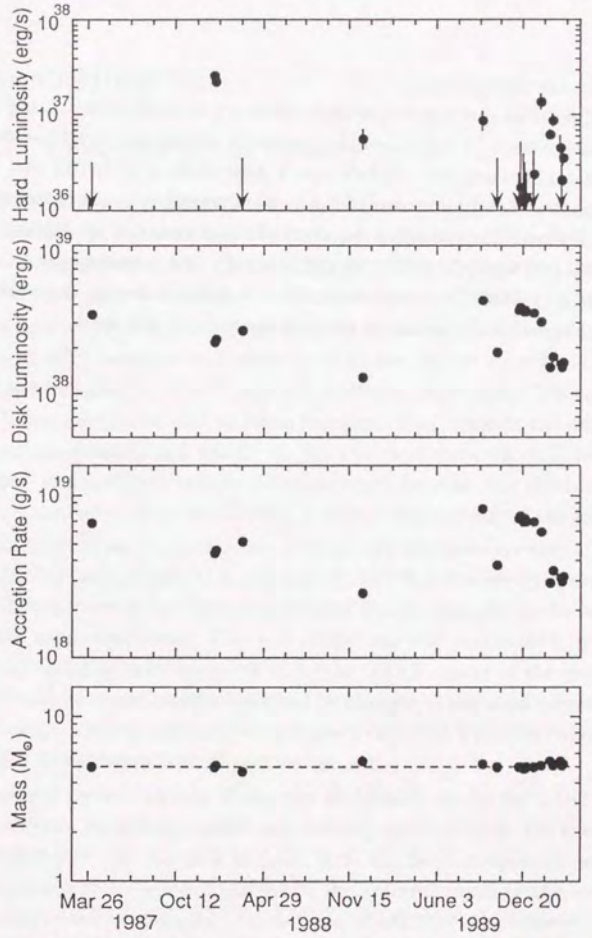

Figure 5.15: Summary of spectral fitting of LMC X-3. The mass of the compact object, the mass accretion rates, the luminosity of the GRAD component (bolometric) and the luminosity of the power-law component (2 – 30 keV) are shown against date. In the calculation of the luminosities, the distance to the source is set to be 50 kpc and isotropic emission is assumed for the hard component. The horizontal dotted line in the bottom panel indicates $M = 5.0 M_\odot$.

than ~ 5 % in any energy range.

I searched possible spectral variations in shorter time scale with making use of the fractional variation. I computed the fractional variations for all the data in table 4.3 and 4.5 between 1.2 – 30 keV over a time scale of 16 to 512 sec. Small intrinsic variations slightly in excess of the Poisson noise level were detected from almost all the data. Representatively, the fractional variation in January 1988 (No. 4 in table 4.3) was 0.96 ± 0.16 % in this energy and frequency range. Other data showed comparable fractional variations. Significant energy dependence of the fractional variation could not be detected from any of the data.

5.3 GS2000+25

5.3.1 Overview of the Spectra

After the outburst of GS2000+25, the LAC observed its spectral evolution over eight months; in the meantime the intensity of the source decreased by more than three orders of magnitude. The energy spectra were reproduced for each of eight observational periods in table 4.6. These are shown altogether in figure 5.16.

In figure 5.16, it is clearly seen that the intensity of GS2000+25 at lower energies ($\lesssim 6$ keV) decreases continuously with time; on the other hand, the intensity at higher energies ($\gtrsim 10$ keV) does not decrease continuously, but rather seems to vary independently of that in lower energies. This suggests the existence of two spectral components in GS2000+25; the soft component which is dominant below ~ 6 keV and probably reflects the mass accretion rate, and the hard component which is dominant above ~ 10 keV and varies independently of the soft component.

Note that these characteristics of the energy spectrum are very similar to those of LMC X-3 (section 5.2.5). In the case of LMC X-3, the energy spectrum was successfully represented by the two component model composed of the soft component and the hard component. The soft component was represented by the emission from an optically thick accretion disk (the GRAD model of the inclination angle of 60°) and its variation was described by changes in the mass accretion rate. The hard component was represented by a power-law with a photon index of ~ 2.2 and it varied independently of the soft component.

Inspired by the success of the two component model for LMC X-3, I adopt the same two component model as a starting point to study the energy spectrum of GS2000+25. In the case of LMC X-3, the hard component was sometimes weak enough to be ignored and hence the spectral shape of the soft component was determined confidently. In the case of GS2000+25, however, a significant hard component exists throughout the observations (figure 5.16), and therefore the precise spectral shape of the soft component is difficult to determine. So in this case I simply assume the multicolor disk model (equivalent to the GRAD model with the inclination angle of 0°) for the soft component of GS2000+25. Such differences between the multicolor disk model and the GRAD model with a

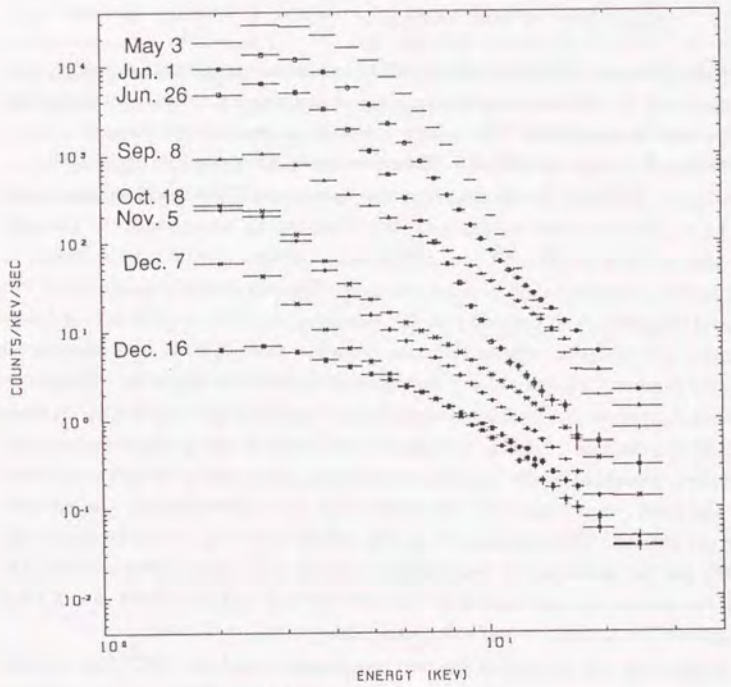

Figure 5.16: Energy spectra of GS2000+25 from May 3 to Dec. 16 in 1988. Note that intensity at lower energies decreases with time constantly whereas that at higher energies does not.

significant inclination angle will be obscured by being overshadowed by the strong hard component (Ebisawa, Mitsuda and Hanawa 1991). If necessary, it is readily possible to convert the parameters of the multicolor disk model to those of the GRAD model (appendix D).

Contrary to the soft component, the spectral shape of the hard component in GS2000+25 is, owing to its relatively high strength, expected to be determined more accurately than that of LMC X-3.

5.3.2 The Hard Component

In this subsection, I investigate spectral shape of the hard component of GS2000+25 using the method applied to the hard component of LMC X-3 in section 5.2.4. To this end, I adopt the spectrum on Oct. 18 (figure 5.17). Since this spectrum has a "kink" around 5 keV, the soft and the hard component, which are respectively dominant below and above $\sim$ 5 keV, are expected to be well separated.

The spectrum was fitted with the multicolor disk model in 1.2 – E_S keV, where E_S is varied from 3.5 keV to 5.8 keV; the residuals of the fits for each E_S are shown together in figure 5.18. It can be seen that the spectral shape of the residuals above 7.6 keV does not depend on E_S, therefore this part of the residuals is certainly identified with the hard component.

In order to investigate its spectral shape, I performed spectral fitting for the hard component. A power-law function was firstly tried; the fit was not good at all and a significant deviation from the power-law was discovered (figure 5.19a). In the residual of the fit, the deviation appears as a broad edge-like structure over 8 to 20 keV. It should be noted this structure is very similar to that in the spectrum of Cyg X-1 (figure 5.2). Since the broad edge-like structure in Cyg X-1 was successfully fitted with the smeared edge model (figure 5.4), it is expected that the structure in GS2000+25 is also represented by this model. Therefore I next tried fitting the hard component with a power-law including the smeared edge model; as expected, this fit was totally successful (figure 5.19b).

5.3.3 Two Component Model Fitting

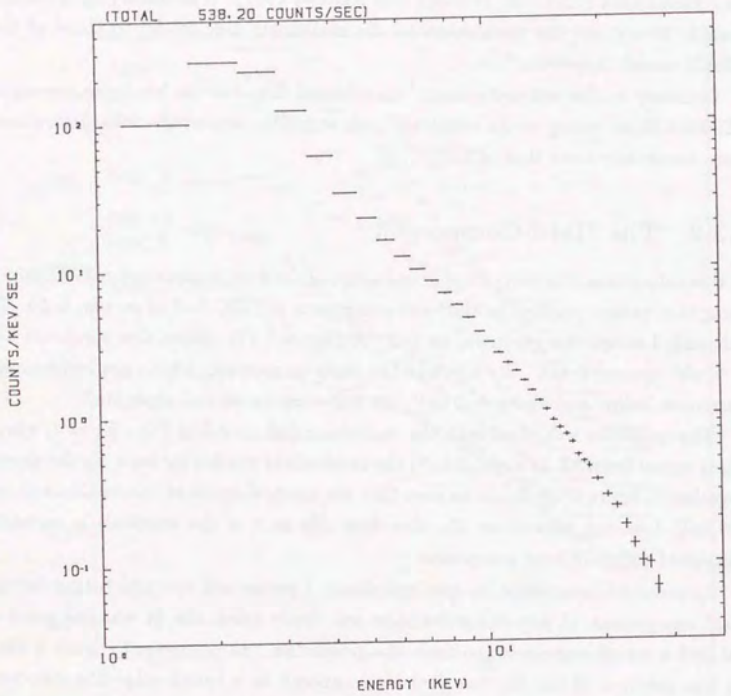

Figure 5.17: Energy spectra of GS2000+25 on Oct. 18, 1988. The vertical scale is different from that in figure 5.16. A "kink" can be recognized around 5 keV.

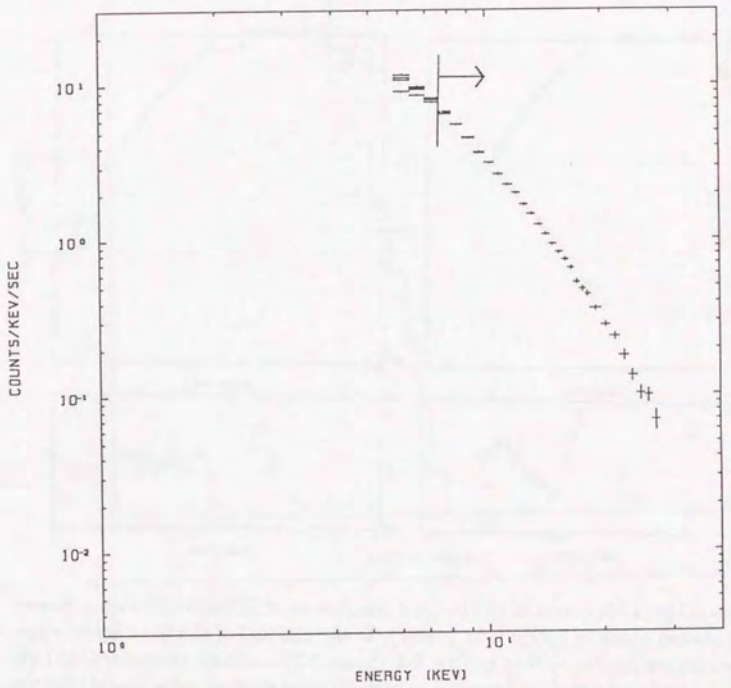

Figure 5.18: Residuals of the spectrum in Oct. 18, 1988 after fitting the lower energy part (1.2 – E_S keV) with the multicolor disk model. E_S is varied from 3.5 to 5.8 keV. It can be seen that the spectral shape above 7.6 keV (indicated with the arrow) does not depend on E_S.

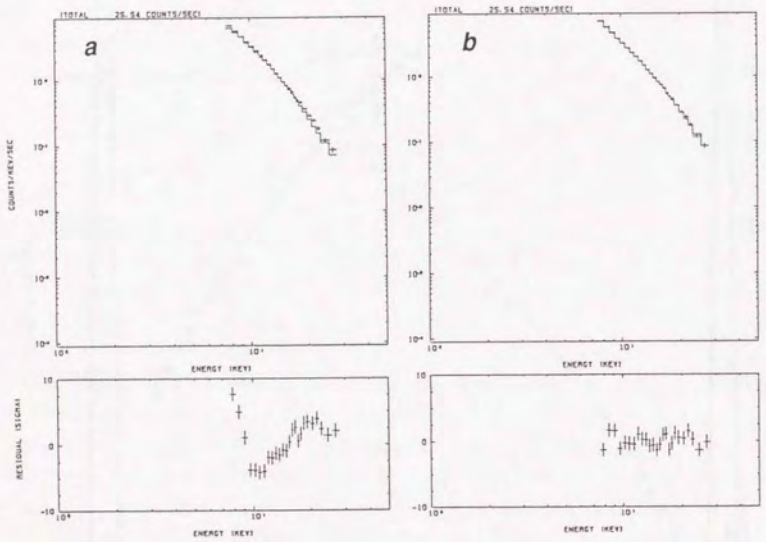

Figure 5.19: (a) Spectral fit to the hard component of GS2000+25 with a power-law (photon index = 1.99; $\chi^2/23 = 10.1$). In the residual of the fit, a broad edge-like structure similar to that in Cyg X-1 (figure 5.2) is clearly recognized. (b) Fit to the same spectrum with a power-law including the smeared edge model (photon index = 1.93, $\log N_H(\mathrm{edge}) = 24.7$, $E_{\mathrm{edge}} = 7.1$ keV (fixed) and $E_W = 34$ keV; $\chi^2/21 = 1.07$). It can be seen that the broad edge-like structure is satisfactorily represented by the smeared edge model.

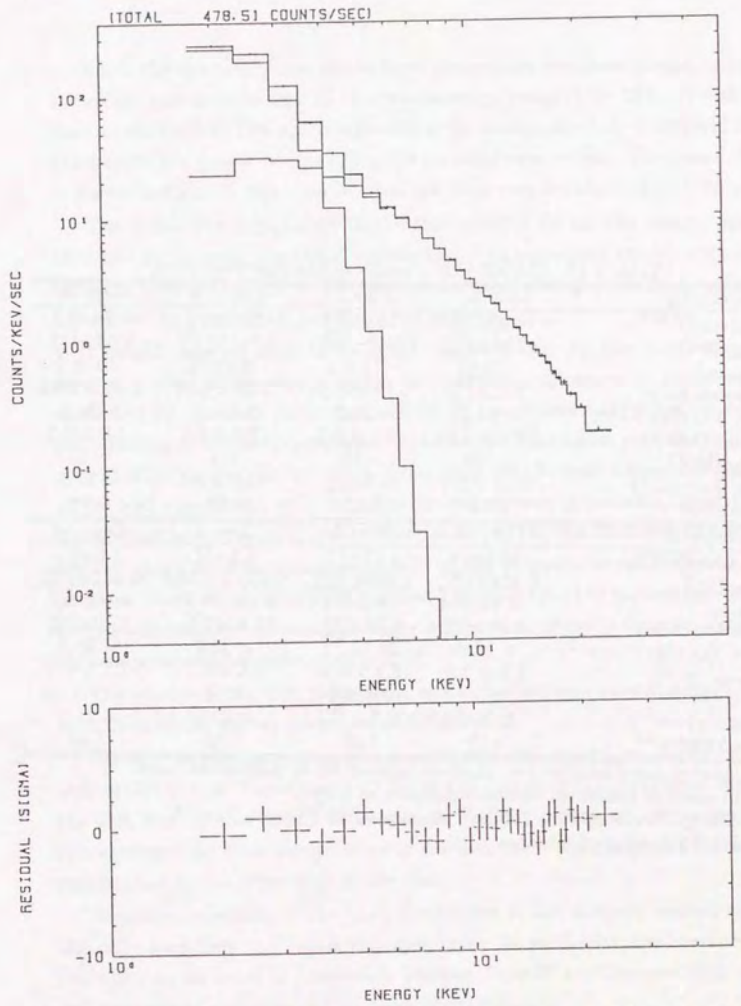

Figure 5.20: Two component model fitting to the spectrum in Oct. 18, 1988. The model is the multicolor disk model (for the soft component) plus a power-law including the smeared edge model (for the hard component).

Table 5.12: GS2000+25: Results of the spectral fitting[a]

Parameter	May 3-7	June 1	June 26	Sep. 8
$r_{in}(\cos\theta)^{1/2}$ [b]	$10.96\pm^{0.20}_{0.17}$	$10.0\pm^{0.6}_{0.4}$	$11.0\pm^{0.7}_{0.6}$	$7.14\pm^{1.3}_{0.8}$
T_{in} (keV)	$1.100\pm^{0.006}_{0.005}$	$0.910\pm^{0.014}_{0.018}$	$0.747\pm^{0.013}_{0.015}$	$0.57\pm^{0.02}_{0.03}$
$F_{\rm power}$ [c]	$21\pm^{3}_{2}$	77 ± 4	$8.8\pm^{3.7}_{2.3}$	51 ± 2
photon index	$2.15\pm^{0.13}_{0.21}$	2.12 ± 0.02	2.52 ± 0.27	1.96 ± 0.03
$\log N_H$(edge) ($\rm cm^{-2}$)	< 24.7	> 24.3	> 24.4	> 24.5
$E_{\rm edge}$ (keV)	9.6 ± 1.9	8.1 ± 0.2	7.8 ± 0.1	7.9 ± 0.1
E_W (keV)	< 106	> 10	> 5	> 20
$\log N_H(\rm cm^{-2})$	21.9 ± 0.1	$21.8\pm^{0.1}_{0.2}$	21.8 ± 0.1	< 21.5
Reduced χ^2 [d]	0.84	1.21	1.22	0.98
Parameter	Oct. 18	Nov. 5	Dec. 7	Dec. 16
$r_{in}(\cos\theta)^{1/2}$ [b]	$10.2\pm^{1.3}_{0.8}$	$14.7\pm^{1.7}_{0.5}$	$8.3\pm^{0.5}_{0.4}$	$1.8\pm^{0.7}_{0.5}$
T_{in} (keV)	$0.424\pm^{0.008}_{0.010}$	$0.385\pm^{0.008}_{0.007}$	0.350 ± 0.005	$0.359\pm^{0.035}_{0.031}$
$F_{\rm power}$ [c]	4.9 ± 0.4	1.5 ± 0.1	0.56 ± 0.06	1.4 ± 0.2
photon index	$1.92\pm^{0.06}_{0.04}$	$2.39\pm^{0.02}_{0.05}$	$2.31\pm^{0.07}_{0.06}$	$1.70\pm^{0.07}_{0.08}$
$\log N_H$(edge) ($\rm cm^{-2}$)	> 23.9	$23.7\pm^{0.2}_{0.1}$	< 23.7	> 23.2
$E_{\rm edge}$ (keV)	7.5 ± 0.2	8.1 ± 0.3	8.1 ± 0.7	7.1 ± 0.5
E_W (keV)	> 4	$2.0\pm^{2.5}_{0.9}$	< 4	> 1
$\log N_H(\rm cm^{-2})$	< 21.6	21.9 ± 0.1	< 21.0	< 21.0
Reduced χ^2 [d]	0.89	1.68	1.55	1.44

[a] Quoted uncertainties are single-parameter 90 % confidence limit.
[b] In units of km at an assumed distance of 1 kpc.
[c] Energy flux over 10 – 100 keV in units of $10^{-10}\,\rm ergs\,s^{-1}\,cm^{-2}$.
[d] For 24 degrees of freedom.

Since the spectral shape of the hard component was determined, next I tried fitting the spectrum on Oct. 18 over whole energy range (1.8 – 25 keV) with the two component model. The soft component is the multicolor disk model and the hard component is a power-law including the smeared edge model. The result of the fits is shown in figure 5.20; it can be seen the fit is very satisfactory ($\chi^2/24 = 0.89$).

The same two component model was applied to all the energy spectra of GS2000+25 taken in the other periods and then successful results were obtained for all of them. The best-fit parameters are tabulated in table 5.12 and the time history of the parameters are displayed in figure 5.21.

I should mention that, in the spectrum from Dec. 16, the hard component is dominant over all the energy range and the soft component is completely overshadowed by the hard component. Even in the lowest energy bin, in which the contribution of the soft component is the largest, the count rate of the soft component is not more than one third of the total one. In such a case, the parameters of the soft component will considerably suffer from systematic uncertainties of the counter response functions at lower energies; i.e., the thickness of the counter window and the lower pulse-height tails of the response to monochrome incident photons. Because of these uncertainties, I suspect that the parameters of the soft component on Dec. 16 contain larger errors than those estimated simply from Poisson errors and quoted in table 5.12.

The results of the two component model fits indicate several noticeable characteristics of the energy spectrum of GS2000+25.

Firstly, the size parameter of the multicolor disk model, $r_{\rm in}\sqrt{\cos\theta}$, is remarkably stable (r.m.s. variation $\simeq$ 20 %) in the course of the significant decrease in the disk flux by two orders of magnitude [7]. This parameter corresponds to the radius where the color temperature of the disk takes the maximum value, i.e. the radius close to the inner edge of the disk.

Secondly, variation of the hard component is not directly related to that of the soft component (i.e., mass accretion rate). In particular, the hard component increased by an order of magnitude between June 26 and September 8, while the soft component decreased by an order of magnitude.

[7] Because of the possible uncertainties mentioned above, I exclude the data on Dec. 16.

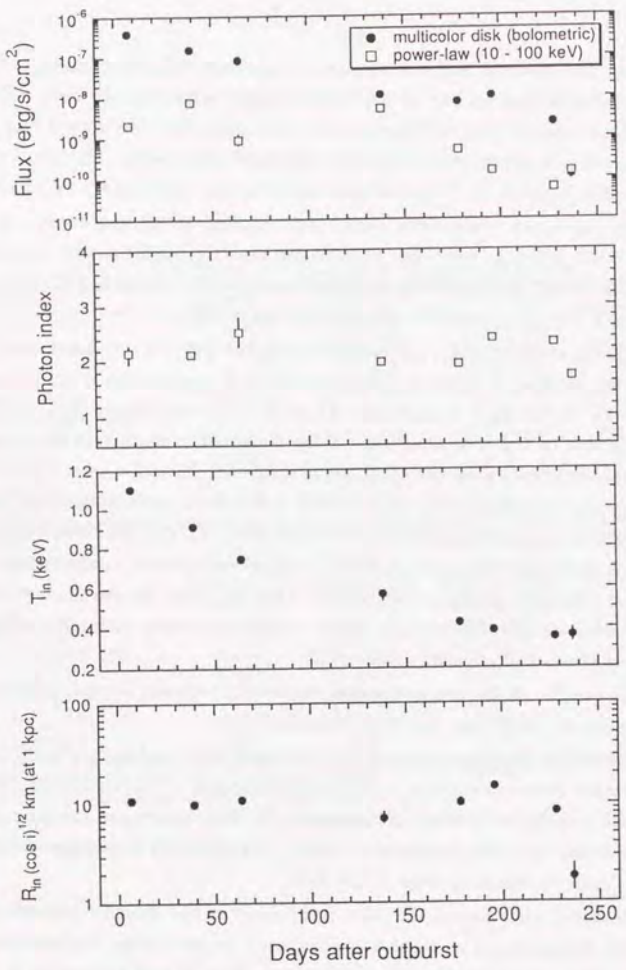

Figure 5.21: Time history of the best-fit parameters in the two component model fitting to GS2000+25. The parameters of the multicolor disk model ($r_{in}\sqrt{\cos\theta}$ and T_{in}), the photon index of the power-law and the energy flux of the two components are indicated. The energy flux of the multicolor disk model is bolometric and that of the power-law component is for 10 – 100 keV.

Table 5.13: GS2000+25: Fractinal Variatons[a,b]

	May 3-7	June 1	June 26[c]	Sep. 8
0.0625 – 256 sec	1.76 ± 0.07	0.90 ± 0.22	1.2 ± 0.4	10.47 ± 0.06
0.5 – 256 sec	1.58 ± 0.04	0.66 ± 0.11	0.98 ± 0.17	4.39 ± 0.06
	Oct. 18	Nov. 5	Dec. 7	Dec. 16
0.0625 – 256 sec	1.0 ± 1.8	4.3 ± 1.2	3.6 ± 3.4	–
0.5 – 256 sec	1.6 ± 0.4	2.3 ± 0.8	2.7 ± 1.5	14.8 ± 2.8

[a] Over 1.2 – 18.6 keV. In a unit of %.
[b] Quoted uncertainties are 1 σ confidence limit.
[c] Over 0.0625 – 32 sec and 0.5 – 32 sec.

Thirdly, the photon index of the power-law component is essentially constant within the range of 1.7 – 2.4 in spite of the large intensity variation of this component over two orders of magnitude.

Finally, the parameters of the smeared edge model, $E_{\rm edge}$ and N_H(edge) are almost always around 8 keV and $> 10^{23.5}{\rm cm}^{-2}$, respectively. The former suggests that the broad edge-like structure is probably related to iron K-edge absorption, since the energy of the iron K-edge lies between 7.1 keV (neutral iron) and 9.3 keV (hydrogen-like iron). The latter implies that absorbing matter which is responsible for the broad edge-like structure persistently exists around the X-ray emitting region over the large luminosity variation of the source.

5.3.4 Short Time Spectral Variation

Intensity variations of GS2000+25 within a day are not significant in any of the observational periods. On a time scale of hours, fluttering intensity variations were occasionally observed, but they were at most $\sim$ 10 % in the whole energy range. Also on this time scale, higher energy parts are more variable, but fractional variations in the $>$ 10 keV range are at most $\sim$ 20 %. It should be noted that large (as much as an order of magnitude) changes of the hard component, such as observed on a time scale of a few months (see the previous subsection), have never been observed during a day.

The fractional variations have been calculated to study variations on timescales

from subseconds to minutes for all the eight observational periods. The calculation was made for the energy range of 1.2 – 18.6 keV and two time ranges of 0.0625 – 256 sec and 0.5 – 256 sec, except for June 26 and Dec. 16 (table 5.13). For the observation on June 26, data trains are shorter than 256 sec, so that the calculation was made for every 32 sec; for Dec. 16, high time resolution data of 0.0625 sec was not available.

Obviously, it is noticeable that the fractional variation on Dec. 16, 14.8±2.8% in 0.5 – 256 sec, is exceptionally large. This might be related to the fact that the hard component is dominant over all the energy range in the energy spectrum on Dec. 16. Among the other observations, large variations on Sep. 8 are remarkable. Note that also on Sep. 8, the hard component was so strong as to become comparable to the soft component (figure 5.21).

The energy dependence of the fractional variations on Sep. 8 is shown in figure 5.22. It can be seen that the fractional variation significantly increases up to ~ 6 keV and it flattens or slightly decreases above this energy. This suggests that the variations of GS2000+25 in this time scale is mainly associated with the hard component than with the soft component.

For the other observational periods, a significant energy dependence of the fractional variations cannot be detected because of small intrinsic variations and/or poor statistics.

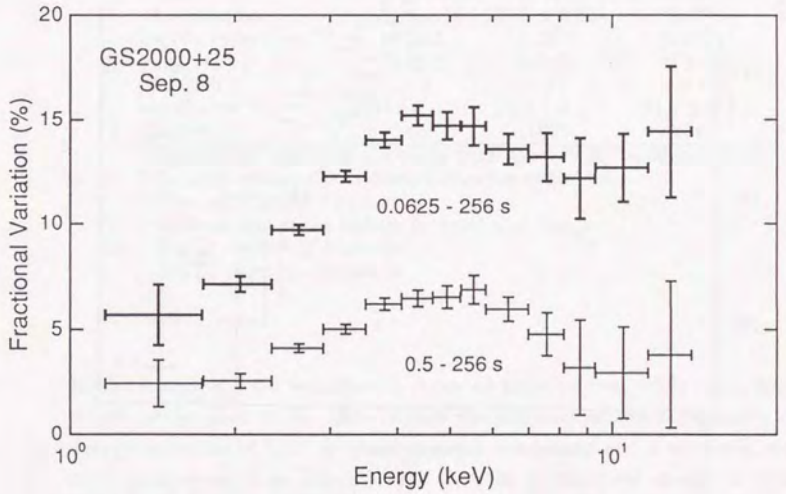

Figure 5.22: Energy dependence of the fractional variations of GS2000+25 in Sep. 8, 1988. The time ranges are 0.0625 – 256 sec (thick lines) and 0.5 – 256 sec (thin lines).

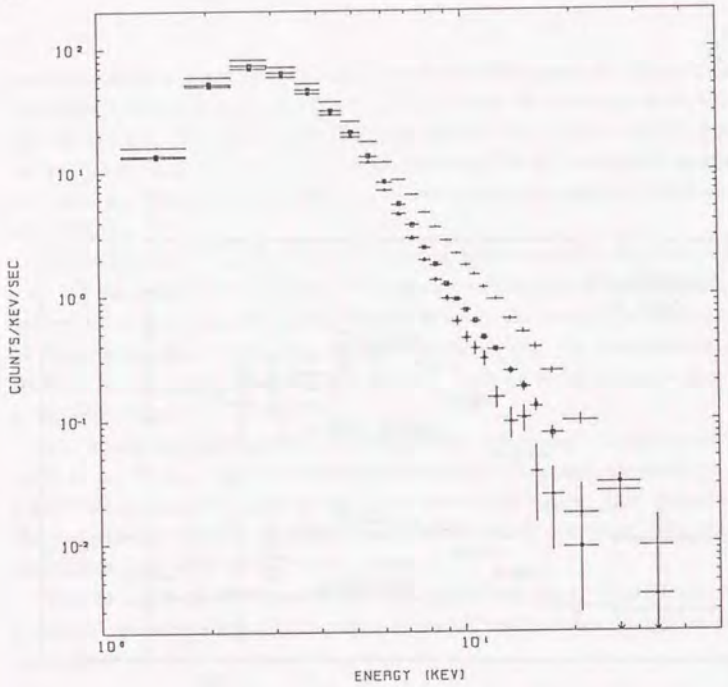

Figure 5.23: Energy spectra of LMC X-1 in April 22 (crosses), July 16 (crosses with squares) and Sep. 30 (crosses with triangles) in 1987.

5.4 LMC X–1

5.4.1 Energy Spectra

In figure 5.23, energy spectra of LMC X-1 in April, July and September, 1987 are shown together; each of them have been averaged over about one day. Although intensity variations between the three periods were at most 25 % in the whole energy range, the energy spectra exhibited larger variations at higher energies.

The large variations at higher energies are clearly seen in the PHA ratios between the three energy spectra (figure 5.24). Above $\sim$ 10 keV, the variations

Table 5.14: LMC X–1: Two Component Model Fiiting[a]

Parameter	1987 Apr.	1987 Jul.	1987 Sep.
$r_{in}(\cos\theta)^{1/2}$ [b]	46 ± 3	44 ± 3	36 ± 2
T_{in} (keV)	0.80 ± 0.03	0.83 ± 0.03	0.90 ± 0.02
$N_{\rm power}$ [c]	0.15 ± 0.03	$0.17^{+0.13}_{-0.07}$	0.040 ± 0.005
photon index	2.31 ± 0.10	2.75 ± 0.22	2.39[d]
$\log N_H$ (edge)($\rm cm^{-2}$)	> 23.9	> 23.6	> 24.4
$E_{\rm edge}$ (keV)	$7.1^{+0.4}_{-0.2}$	$6.9^{+0.5}_{-0.3}$	$8.4^{+0.8}_{-0.7}$
E_W (keV)	> 4	> 1.2	> 5
$\log N_H(\rm cm^{-2})$	21.85 ± 0.07	22.0 ± 0.1	21.7 ± 0.1
Reduced χ^2	0.65[e]	0.82[e]	1.16[f]

[a] Quoted uncertainties are single-parameter 90 % confidence limit.
[b] In units of km at an assumed distance of 50 kpc.
[c] Photons $\rm s^{-1}\,keV^{-1}$ at 1 keV.
[d] The average of the indices in April and July.
[e] For 24 degrees of freedom.
[f] For 25 degrees of freedom.

in the energy spectra are about a factor of three to five, while those below $\sim$ 5 keV are at most 20 %. This implies the existence of two components in the energy spectrum of LMC X-1; a stable soft component and a relatively variable hard component. It is then supposed that the origin of the energy spectrum of LMC X-1 is similar to that of LMC X-3 and GS2000+25.

I have fitted the energy spectra of LMC X-1 with the two component model which was successfully applied to GS2000+25 in the previous section. The model consists of the multicolor disk model (for the soft component) and a power-law including the smeared edge model (for the hard component). In the September spectrum, the hard component was too weak for the photon index of the power-law to be uniquely determined, so the index was fixed to the average of those in April and July. The results of the fits are tabulated in table 5.14; all the three fits are totally successful.

In figure 5.25, an example of the spectral fitting for the April spectrum is shown.

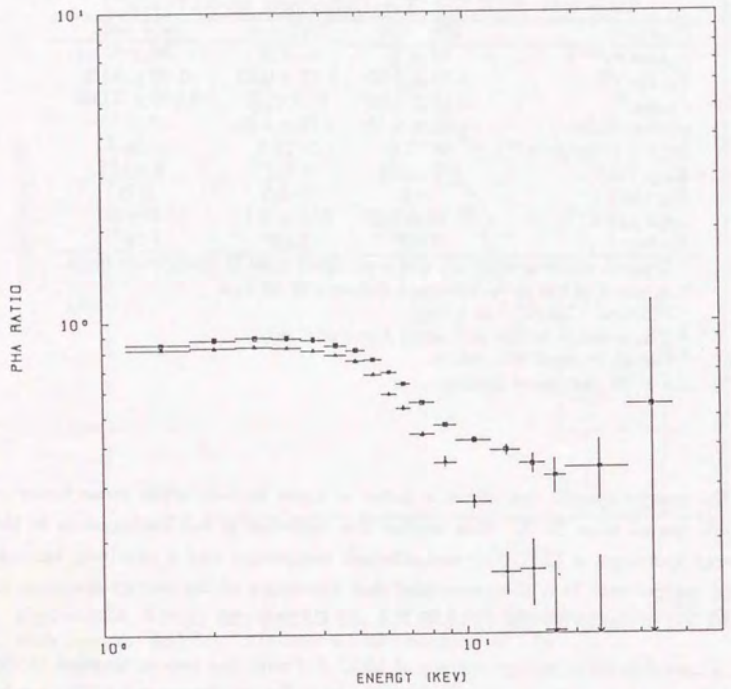

Figure 5.24: PHA ratios of LMC X-1. The ratios of the spectrum in July (crosses with squares) and in September (crosses with triangles) to that in April are shown together.

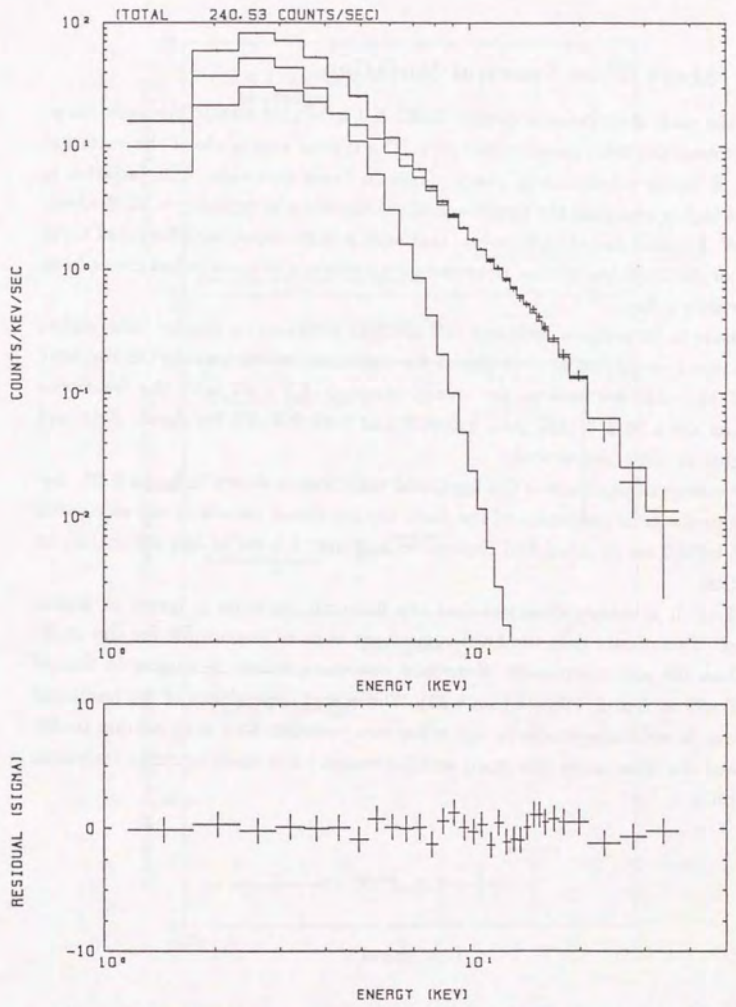

Figure 5.25: The two component fitting for the energy spectrum of LMC X-1 in April 22, 1987. The model is the multicolor disk model (for the soft component) and a power-law including the smeared edge model (for the hard component).

5.4.2 Short Time Spectral Variation

During the each observational period, LMC X-1 exhibited erratic intensity variation on timescales from minutes to hours. The typical amplitude of the variation is $\sim$ 15 % in the whole energy range. Also on these timescales, the variation is larger at higher energies; the amplitude of the variation is typically $\sim$ 30 % above $\sim$ 10 keV. I should mention, however, that such a large variation (a factor of three or five) of the hard component observed on a timescale of months has never been found within a day.

In order to investigate intensity and spectral variation on shorter time scales, the fractional variations are calculated for each observation period. On the time scale of 16 – 256 sec and in the energy range of 1.2 – 23 keV, the fractional variations are $1.56 \pm 0.13\%$, $3.51 \pm 0.09\%$ and $3.43 \pm 0.19\%$ for April, July and September in 1987, respectively.

The energy dependence of the fractional variations is shown in figure 5.26. According to the time resolution of the data, the fractional variations are calculated over 16 to 256 sec in April and September and over 0.5 sec to 256 sec in July in figure 5.26.

In July, it is clearly observed that the factional variation is larger at higher energies. This means that the hard component is more responsible for the variations than the soft component. Note that this characteristic is similar to that of GS2000+25 in Sep. 8, 1988 (figure 5.22). The energy dependence of the fractional variations is not conspicuous in the other two periods. This may be due to difference of the time scales (for April and September) and small intrinsic variations (for April).

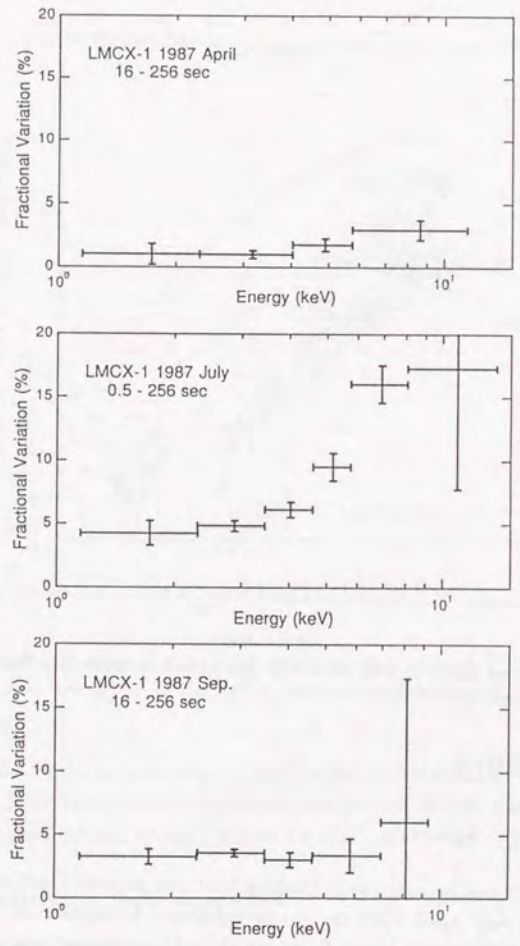

Figure 5.26: Fractional variations of LMC X-1 in April 22, July 16 and Sep. 30 in 1988.

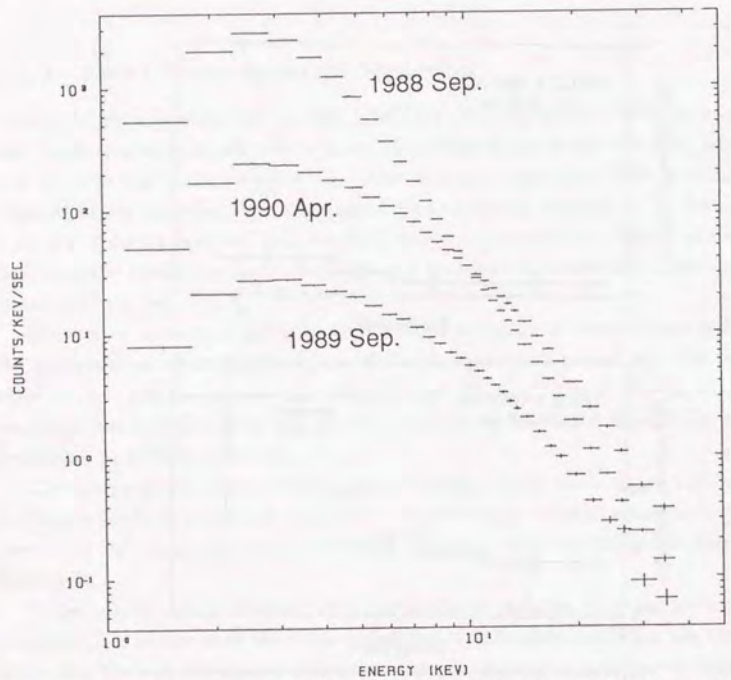

Figure 5.27: Energy spectra of GX339–4 in Sep. 1988 (branch 4 in figure 5.28), Sep. 1989 and April 1990.

5.5 GX339–4

5.5.1 Energy Spectra

In figure 5.27, the energy spectra of GX339–4 for three periods, September 1988, September 1989 and April 1990 are shown together. In September 1988, the intensity of the source was $\sim$ 0.8 Crab, which is the brightest ever observed. The spectrum was one in the typical high state; ultra-soft with a clear hard-tail (see section 2.4.3). On the other hand, both in September 1989 and April 1990, the source showed a relatively hard and power-law like energy spectrum. The

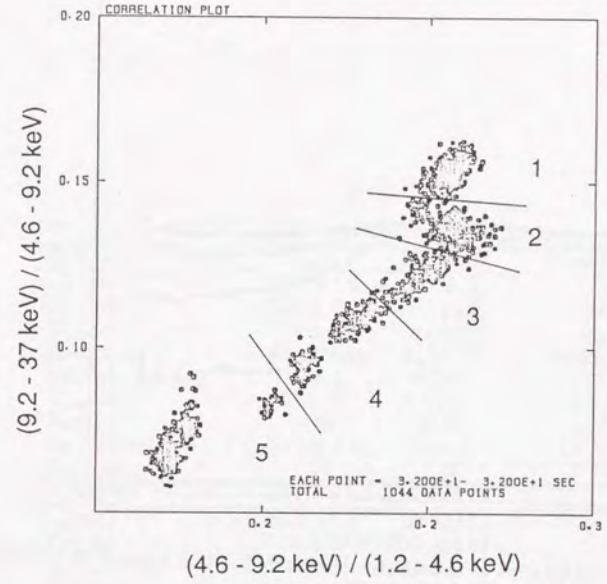

Figure 5.28: A color-color diagram of GX339–4 in September 1988. Note that only MPC2 data are shown in the figure. Data are divided into five parts for spectral study.

intensities of the source were $\sim$ 15 mCrab in the former and $\sim$ 100 mCrab in the latter. These two periods are classified into the low (or off) state according to the general classification system (section 2.4.3).

Observations in September 1988

During the observations in September 1988, GX339–4 showed distinct spectral branches (figure 5.28), which are similar to those of bright LMXBs (section 2.3.2). Power spectra of this period, including $\sim$ 6 Hz QPO (section 2.3.2), are strongly dependent on these spectral branches (Dotani 1989; Kitamoto 1989; Miyamoto,

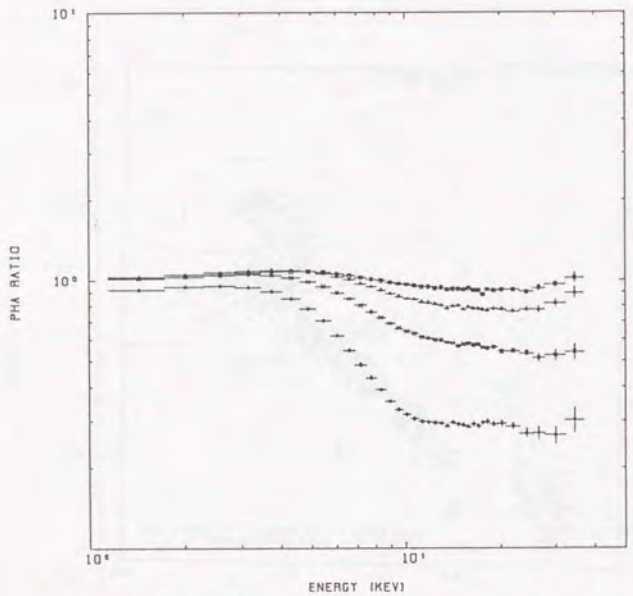

Figure 5.29: PHA ratios of the spectra of branch 2 – 5 in figure 5.28 to that of branch 1.

Kitamoto and Kimura 1989).

I divided these data into five parts, branches 1 – 5, according to the positions on the color-color diagram (figure 5.28). A comparison was made in the PHA ratio between the five spectra (figure 5.29). It is obvious that higher energy parts of the spectrum show large variation, as in the case of LMC X-3, GS2000+25 and LMC X-1. This suggests that the energy spectra of GX339–4 in this period can be represented by the same two component model as was used for the other sources.

I tried fitting those five spectra with that two component model; the multicolor disk model for the soft component and a power-law including the smeared edge model for the hard component. The results are tabulated in table 5.15. It is found that spectra of branch 2 and branch 3 yield large reduced χ^2 values (> 1.9), which are rejected with 99.9 % confidence limit. Since the residuals of those two fits suggested an emission line at around 6.4 keV, I performed fitting again

Table 5.15: GX339–4 (1988): Fit with the two component model[a]

Parameter	Branch 1	Branch 2	Branch 3
$r_{in}(\cos\theta)^{1/2}$ [b]	20.0 ± 1.5	$17.8\pm^{1.1}_{1.9}$	$17.1\pm^{1.6}_{0.5}$
T_{in} (keV)	0.79 ± 0.03	$0.85\pm^{0.05}_{0.02}$	$0.88\pm^{0.02}_{0.03}$
$N_{\rm power}$ [c]	7.4 ± 0.6	$7.0\pm^{0.5}_{1.5}$	$6.0\pm^{0.9}_{0.4}$
photon index	2.52 ± 0.02	$2.53\pm^{0.02}_{0.07}$	$2.54\pm^{0.04}_{0.02}$
$\log N_H$(edge) ($\rm cm^{-2}$)	> 25.1	> 25.0	> 25.1
$E_{\rm edge}$(keV)	7.2 ± 0.1	7.4 ± 0.1	7.5 ± 0.1
E_W (keV)	> 60	> 55	> 60
$\log N_H(\rm cm^{-2})$	21.8 ± 0.1	21.8 ± 0.1	21.7 ± 0.1
Reduced χ^2 [e]	0.95	1.98	2.31
Parameter	Branch 4	Branch 5	
$r_{in}(\cos\theta)^{1/2}$ [b]	19.2 ± 0.8	$21.9\pm^{1.5}_{1.1}$	
T_{in} (keV)	0.84 ± 0.03	0.81 ± 0.02	
$N_{\rm power}$ [c]	$7.2\pm^{1.7}_{0.8}$	3.5 ± 0.8	
photon index	$2.71\pm^{0.06}_{0.04}$	2.67 ± 0.06	
$\log N_H$(edge) ($\rm cm^{-2}$)	> 25.0	> 24.5	
$E_{\rm edge}$(keV)	7.2 ± 0.1	7.0 ± 0.1	
E_W (keV)	> 50	> 13	
$\log N_H(\rm cm^{-2})$	21.8 ± 0.1	21.8 ± 0.1	
Reduced χ^2 [d]	1.03	0.83	

[a] Quoted uncertainties are single parameter 90 % confidence limit.
[b] In units of km at an assumed distance of 4 kpc.
[c] Photons $\rm s^{-1}\,cm^{-2}\,keV^{-1}$ at 1 keV.
[d] For 38 degrees of freedom.

Table 5.16: GX339–4 (1988): Fit with the two component model with an emission line[a]

Parameter	Branch 1	Branch 2	Branch 3
$r_{in}(\cos\theta)^{1/2}$ [b]	19.7 ± 1.5	17.2 ± 1.0	$18.0\pm^{1.0}_{1.2}$
T_{in} (keV)	0.81 ± 0.03	0.885 ± 0.025	$0.88\pm^{0.03}_{0.02}$
$N_{\rm power}$ [c]	6.1 ± 0.7	4.7 ± 0.7	4.9 ± 0.7
photon index	2.46 ± 0.03	2.41 ± 0.03	2.48 ± 0.04
$\log N_H$(edge)	> 24.8	> 25.1	> 25.0
E_{edge}(keV)	7.46 ± 0.18	7.95 ± 0.30	$7.9\pm^{0.4}_{0.2}$
E_W (keV)	> 40	> 75	> 55
Line intensity [d]	6 ± 3	8.3 ± 2.0	7.8 ± 1.6
Line center (keV)	6.15 ± 0.20	6.38 ± 0.12	6.34 ± 0.12
$\log N_H(\mathrm{cm}^{-2})$	21.77 ± 0.06	21.69 ± 0.03	21.73 ± 0.02
Reduced χ^2 [e]	0.72	1.26	1.70

Parameter	Branch 4	Branch 5
$r_{in}(\cos\theta)^{1/2}$ [b]	$19.6\pm^{0.6}_{0.9}$	$21.8\pm^{1.9}_{0.7}$
T_{in} (keV)	$0.85\pm^{0.02}_{0.03}$	$0.82\pm^{0.01}_{0.03}$
$N_{\rm power}$ [c]	5.7 ± 1.4	$2.8\pm^{1.1}_{0.6}$
photon index	2.64 ± 0.06	$2.62\pm^{0.10}_{0.07}$
$\log N_H$(edge)	> 24.7	> 24.2
E_{edge}(keV)	7.50 ± 0.20	$7.2\pm^{0.2}_{0.3}$
E_W (keV)	> 30	> 7
Line intensity [d]	5.3 ± 2.2	2.8 ± 1.0
Line center (keV)	6.23 ± 0.19	6.09 ± 0.21
$\log N_H(\mathrm{cm}^{-2})$	21.8 ± 0.04	21.78 ± 0.06
Reduced χ^2 [e]	0.80	0.80

[a] Quoted uncertainties are single-parameter 90 % confidence limit.
[b] In units of km at an assumed distance of 4 kpc.
[c] Photons $\mathrm{s}^{-1}\,\mathrm{cm}^{-2}\,\mathrm{keV}^{-1}$ at 1 keV.
[d] 10^{-3} photons $\mathrm{s}^{-1}\,\mathrm{cm}^{-2}$.
[e] For 36 degrees of freedom.

Table 5.17: GX339–4 (1989 and 1990): Fit with a power-law

Parameter	1989 Sep.	1990 April
$N_{\rm power}$ [a]	0.0675	0.623
photon index	1.59	1.75
$\log N_H(\mathrm{cm}^{-2})$	< 20	< 20
Reduced χ^2	17.8[b]	9.09[c]

[a] Photons $\mathrm{s}^{-1}\,\mathrm{cm}^{-2}\,\mathrm{keV}^{-1}$ at 1keV.
[b] For 29 degrees of freedom.
[c] For 31 degrees of freedom.

including an emission line with a narrow width ($1\sigma = 0.05$ keV [8]) and free central energy (table 5.16; figure 5.30). Then the fits for the spectra of branch 2 and 3 were improved considerably. I should mention, however, that the intensity of the emission line is strongly dependent on the modelling of the edge structure. The origin of the emission line will be discussed in the next chapter together with the physical interpretation of the smeared edge model.

Observations in September 1989 and in April 1990

The spectra in September 1989 and April 1990 are much harder than that in September 1988 (figure 5.27). Since previous studies suggest that the energy spectrum of GX339–4 in the low and off state is represented with a single power-law (section 2.4.3), I first tried fitting the two spectra with a power-law model (figure 5.31; table 5.17).

In the residual of the fit for the spectrum in April 1990, a broad edge-like structure over $\sim$ 8 to $\sim$ 20 keV is conspicuous as well as a significant emission line. This broad edge-like structure is very similar to those found in Cyg X-1 (figure 5.2) and GS2000+25 (figure 5.18). On the other hand in the residual for September 1989, an emission line and an edge-like structure are less conspicuous; instead, a soft excess below $\sim$ 2 keV, which might be related to an optically thick accretion disk component, is recognized.

I found that both spectra can be fitted successfully with the two component

[8] This is negligibly small compared to the energy resolution of the LAC.

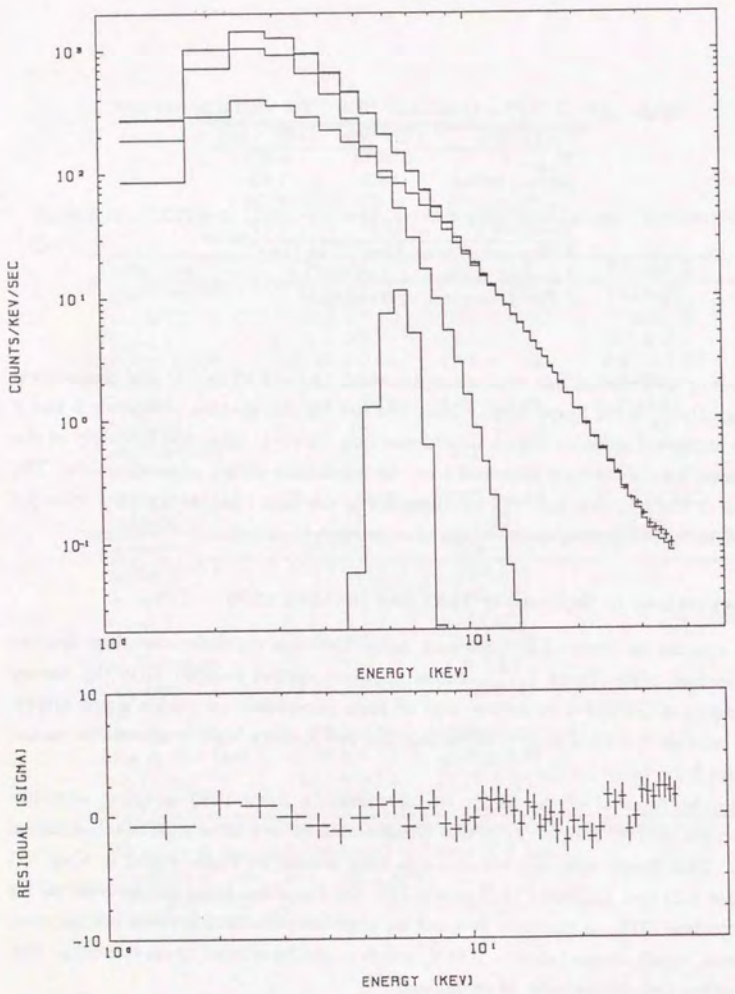

Figure 5.30: An example of the fit for GX339-4 in September 1988 (branch 3 in figure 5.28). The model is the multicolor disk, a power-law including the smeared edge model and an emission line.

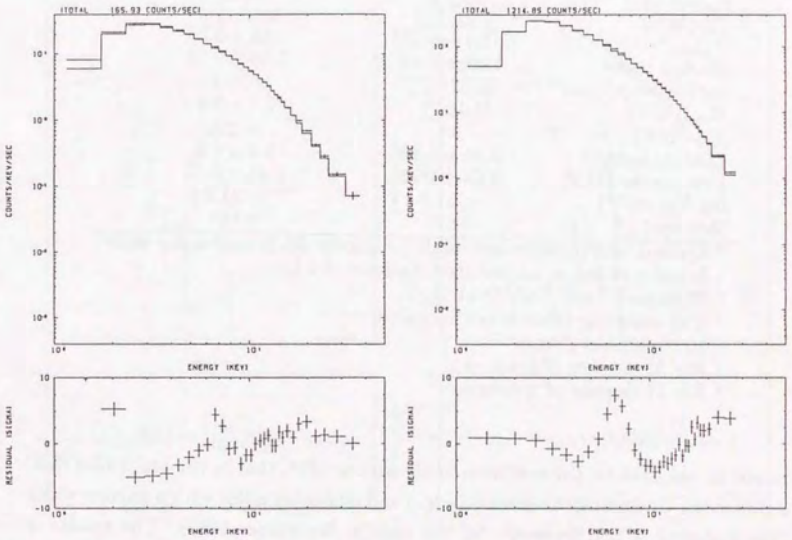

Figure 5.31: Fit with a power-law model for the spectra of GX339–4 in September 1989 and April 1990.

Table 5.18: GX339–4 (1989 and 1990): Fit with the two component model with an emission line[a]

Parameter	1989 Sep.	1990 April
$r_{in}(\cos\theta)^{1/2}$ [b]	$81\pm^{40}_{20}$	$14\pm^{15}_{9}$
T_{in} (keV)	$0.23\pm^{0.02}_{0.03}$	$0.46\pm^{0.19}_{0.07}$
$N_{\rm power}$ [c]	0.060 ± 0.003	0.55 ± 0.03
Photon index	1.53 ± 0.02	1.68 ± 0.02
$\log N_H$(edge) ($\rm cm^{-2}$)	$22.82\pm^{0.04}_{0.12}$	> 23.45
$E_{\rm edge}$(keV)	$8.1\pm^{0.5}_{0.6}$	7.7 ± 0.4
E_W (keV)	$-$[d]	> 2.8
Line intensity [e]	0.25 ± 0.10	2.4 ± 0.6
Line center (keV)	6.64 ± 0.23	6.45 ± 0.13
$\log N_H(\rm cm^{-2})$	< 21.5	< 21.6
Reduced χ^2	0.67[f]	0.64[g]

[a] Quoted uncertainties are single-parameter 90 % confidence limit.
[b] In units of km at an assumed distance of 4 kpc.
[c] Photons $\rm s^{-1}\,cm^{-2}\,keV^{-1}$ at 1keV.
[d] The smearing effect is not included.
[e] 10^{-3} photons $\rm s^{-1}\,cm^{-2}$.
[f] For 23 degrees of freedom.
[g] For 24 degrees of freedom.

model as was used for the spectrum in September 1988, that is, the multicolor disk, a power-law (including the smeared edge) and an emission line with a narrow width (the smearing is not necessary for the edge in September 1989). The results of these fits are shown in figure 5.32 and the best fit parameters are tabulated in table 5.18.

5.5.2 Short Time Spectral Variation

Short time intensity and spectral variations of GX339–4 have been investigated by making use of the fractional variations.

Firstly, in order to compare the short time variations in the three observational periods (i.e. three different luminosity states), the fractional variations were calculated on the same timescale. According to the minimum time resolution of the data in 1990 April, the calculations were made for 4 – 256 sec; the energy range is

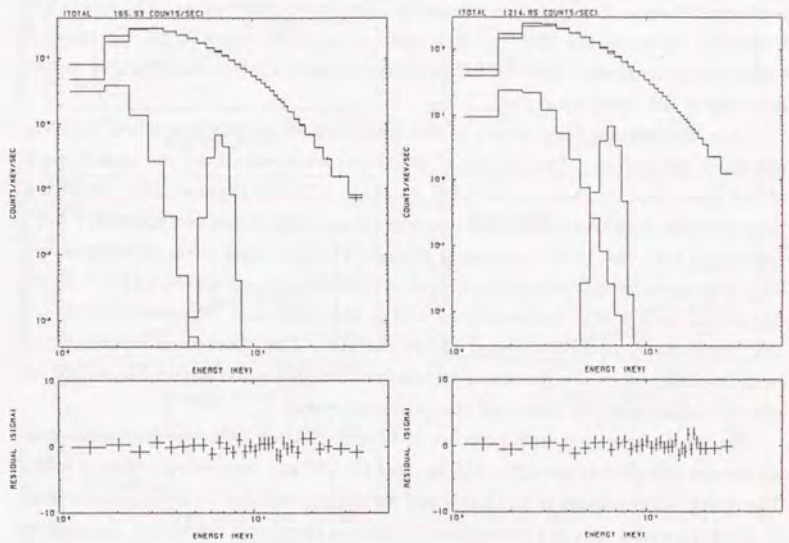

Figure 5.32: The two component model fit for GX339–4 in September 1989 (left) and April 1990 (right). The model is the multicolor disk, a power-law (including the smeared edge) and an emission line of the narrow width (the smearing is not necessary for the edge in September 1989).

set to 1.2 – 37 keV. For the five branches of the observation in September 1988, the fractional variations with this time and energy range are as follows; $1.66 \pm 0.02\%$, $4.98 \pm 0.02\%$, $2.01 \pm 0.02\%$, $0.70 \pm 0.02\%$ and $0.73 \pm 0.03\%$. It can be seen that the fractional variations are smaller for branches 4 and 5 in which the hard component is relatively weak. For the observations in 1989 September and in 1990 April, the fractional variations are $25.04 \pm 0.20\%$ and $8.56 \pm 0.10\%$, respectively. Comparing the three observational periods, the fractional variation increases according to the decrease of the intensity.

Next, the energy dependence of the fractional variations is studied for each observational period. The fractional variations were calculated for each branch of the observation in September 1988 over 0.5 – 256 sec (figure 5.33). In all the branches, the fractional variations increase toward higher energies up to ~ 7 keV, indicating that the hard component is more variable than the soft component. This is a characteristic which is common to GS2000+25 and also to LMC X-1 (see figure 5.22 and 5.26). In branches 1 and 2, the fractional variations above ~ 7 keV significantly decrease toward higher energies. This characteristic, which has been implied also in the fractional variation of GS2000+25 (figure 5.22), might be related to the intrinsic nature of the hard component.

For the observations in September 1989 and in April 1990, the fractional variations are calculated over 0.5 – 256 sec and 4 – 256 sec, respectively (figure 5.34). The energy dependence of the fractional variation is smaller in both periods than in the high state; this is most probably because the single power-law component is dominant over all energies. In September 1989, a decrease of the fractional variation in the lowest energy channel is notable. This is probably due to the small intrinsic variation of the soft component.

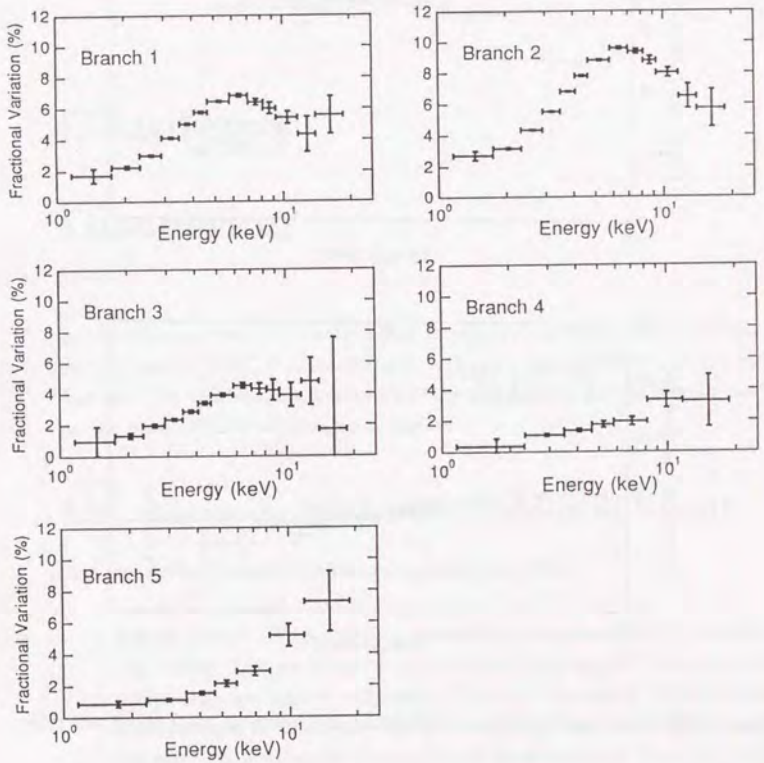

Figure 5.33: Fractional variations of GX339-4 in September 1988 for each branch.

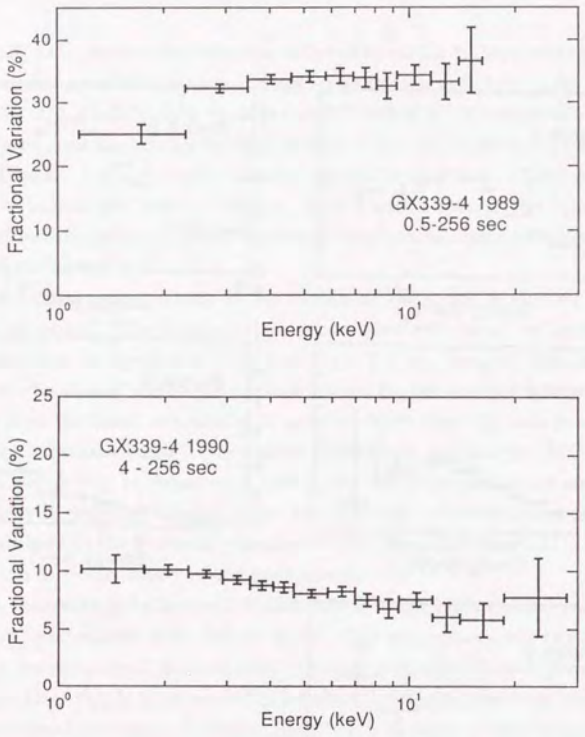

Figure 5.34: Fractional variations of GX339-4 in September 1989 and April 1990.

Chapter 6

Discussion

In the previous chapter, I investigated the energy spectra of five black hole candidates Cyg X-1, LMC X-3, GS2000+25, LMC X-1 and GX339–4. In this chapter, I discuss X-ray emission mechanisms and the physical conditions around black holes on the basis of these observational results.

6.1 Summary of the Observational Results

The main observational results are summarized below.

1. All the spectra of the observed sources can be represented by a unified spectral model. The model consists of a sum of two spectral components; a soft component and a hard component. The soft component is represented by a superposition of blackbody spectra of different temperatures with a weighting function expected from an optically thick accretion disk. The maximum of the blackbody color temperature is in the range of 0.4 – 1.2 keV. On the other hand, the hard component is approximated by a power-law with a photon index of 1.7 – 2.5 modified by a broad edge-like structure over 7 – 20 keV.

2. The observed energy spectra can be classified into two types; hard spectra or soft spectra. Cyg X-1 and GX339–4 in the low state exhibit hard spectra,

while LMC X-3, GS2000+25, LMC X-1 and GX339–4 in the high state exhibit soft spectra [1].

In terms of the unified model, the spectral state is determined by the ratio of the intensities of the two components. In the hard state, the soft component is nearly or totally invisible in the observed energy range (1 – 30 or 2 – 60 keV), while in the soft state the soft component dominates the spectra in the energy range of 1 – 10 keV. In some cases, the hard component becomes almost invisible in the soft state.

3. The soft component is stable on timescales shorter than about a day. For LMC X-3 and GS2000+25, the intensity of the soft component varied by a factor of four and two orders of magnitude respectively on timescales longer than a few days. The variations are mostly due to changes in the color temperature of the accretion disk, with the area of the emission region remaining virtually constant.

4. The hard component is variable on a wide range of timescales. In the soft state, the hard component exhibits larger variations than the soft component does. The long term variations show no correlations with those of the soft component. In particular, for GS2000+25, the intensity (or the temperature) of the soft component decreased monotonically after the outburst, whereas the intensity of the hard component appeared to vary erratically.

   The hard component in the hard state is also variable on a wide range of timescales. The r.m.s. variation amplitude is about 20 – 30 % on a timescale of 0.5 – 256 sec. The short-term variations are larger than those of the hard component in the soft state.

5. The photon index of the hard component in the hard state is 1.5 – 1.7, whereas in the soft state, the slope slightly steepens to 2.0 – 2.5.

Below in this chapter, firstly I discuss the nature of the soft component in terms of the optically thick accretion disk model. Next I discuss some physical

[1] In this chapter, I shall use the terms the "hard state" and the "soft state" to designate the two spectral states in which the sources exhibit hard and soft spectra respectively.

mechanisms which yield the broad edge-like structure in the hard component. Possible origins of the hard component and mechanisms of its temporal variation are then conjectured.

6.2 Origin of the Soft Component

The soft components of LMC X-3, GS2000+25, LMC X-1 and GX339–4 can all be represented by a multicolor disk model (referred to as MCD model in the following), an approximation of an emergent spectrum from optically thick accretion disks. Among these sources, the hard component of LMC X-3 occasionally became very weak; thus it was possible to study the detailed spectral shape of its soft component independently of the hard component. The soft component of LMC X-3 was then found to be better fitted by the model in which effects of general relativity are additionally considered (the GRAD model).

In the mass accretion onto a blackhole, an accretion disk is expected to be formed around the blackhole (e.g., Shakura and Sunyaev 1973). The MCD and GRAD model provide us with a natural interpretation of the soft component in terms of the emission from accretion disks. The soft component can also be represented by the Comptonization model by Sunyaev and Titarchuk (1980). However, this model contains several difficulties in the physical interpretation; for example the source of the copious soft photons is unknown. Therefore I consider the MCD or GRAD model to be a more appropriate model than the Comptonization model to represent the soft component of the black hole candidates.

Significant variations of the intensity of the soft component were observed for LMC X-3 by a factor of four and for GS2000+25 by two orders of magnitudes. In these variations, the derived size of the emission region, i.e. the radius of the inner edges of the disks was found to remain remarkably constant.

Makishima *et al.* (1986) observed GX339–4 in the high state with *Tenma* and applied the MCD model to the soft component of the spectrum. During the *Tenma* observation, the intensity of the source was about 400 mCrab, which is about half the intensity of the present high state observation with *Ginga*. In spite of significant change in the luminosity and the disk temperature ($T_{\rm in} \simeq 0.77 \pm 0.01$ keV with *Tenma* and 0.82 – 0.89 keV with *Ginga*), the inner radius of the

accretion disk has varied little between the *Tenma* and the present observations ($r_{in}\sqrt{\cos i} \simeq 20.7 \pm 0.5$ km with *Tenma* and 17 - 21 km with *Ginga*, at 4 kpc).

It is very plausible that the gradual decrease of intensity in GS2000+25 after the outburst is due to decrease of the mass accretion rate onto the compact object. The significant intensity changes in LMC X-3 and GX339–4 are also most likely to be due to changes of the mass accretion rate. Therefore in these sources, it is considered that the optically thick accretion disks with the constant inner radii are maintained stably in the course of large changes of the mass accretion rate.

In the standard α-disk model (Shakura and Sunyaev 1973), the inner region of accretion disks, where radiation pressure dominates gas pressure, is considered to be thermally unstable (Shibazaki and Hoshi 1975; Shakura and Sunyaev 1976; Pringle 1976). It has thus been suggested that the inner region inside a critical radius switches from an optically-thick, geometrically-thin disk to an optically-thin, geometrically-thick disk (e.g. Hoshi 1984). The critical radius, r_c, depends on the mass accretion rate as (Hoshi 1984),

$$r_c = 53\,\alpha^{2/21}\left(\frac{\dot{M}}{10^{17}\mathrm{g\,s^{-1}}}\right)^{16/21}\left(\frac{M}{M_\odot}\right)^{1/3}\ \mathrm{km}. \tag{6.1}$$

Such a dependence of the inner radius of the optically thick disk on the mass accretion rate must have been detected if it were to occur. Furthermore, the observed constant radius of LMC X-3, $\sim$ 45 km, (notice the inclination angle is limited to be $< 70°$ from optical observations) is much smaller than r_c ($\sim$ 2000 km; for $\alpha \sim 1$, $\dot{M} \sim 5 \times 10^{18}\,\mathrm{g\,s^{-1}}$ and $M \sim 10 M_\odot$) except when α is extremely small ($\sim 10^{-18}$). I thus conclude that the inner radius of the optically thick disk is not determined by the thermal instability referred to above.

I point out that the thermal instability does not necessarily occur in some accretion disk models with different models of viscosity. For example, if the viscous stress is proportional to only the gas pressure, not as in the standard α-disk model in which it is proportional to the total pressure, the thermal instability does not occur (Hoshi 1985; Kakubari, Hoshi and Asaoka 1989). Even if the standard prescription of the viscosity is adopted, taking account of horizontal pressure and entropy gradient in accretion disks, the instability disappears for a high enough accretion rate (Abramowicz *et al.* 1988). Alternatively, it could be possible that

the instability actually occurs in the inner region of an accretion disk but the optically thick disk still remains. The resultant disk would be like a two stream structure such as that proposed by Hoshi (1985) where the optically thin disk is sandwiching the optically thick disk.

Then what determines the inner radius ? Because of the remarkable stability, I consider that it is very plausible that the inner radius is determined by the last stable Keplerian orbit around the compact object, i.e. 3 r_g, where r_g is the Schwarzschild radius. Around a Schwarzschild black hole, 3 r_g is the minimum circular orbit of stable Keplerian motions. Except when a black hole is rotating with nearly the light velocity (a Kerr black hole), this radius can be taken as the minimum radius that the inner edge of an accretion disk around the black hole can hold.

In this scheme, the observed constant radii of the accretion disks can be related to the mass of the compact objects. It is not correct to substitute the value of r_{in} obtained from the MCD model into 3 r_g, since in the MCD model the boundary condition at 3 r_g is not precisely considered and effects of general relativity, such as the gravitational red-shift and doppler shift due to the Keplerian motion, are neglected. Instead, we need to convert the parameters of the MCD model into those of the GRAD model (appendix D). In the GRAD model, it is assumed that the optically thick accretion disk ends at 3 r_g and there is no friction at that point. The GRAD model has five parameters; the mass of the compact object, the mass accretion rate, the inclination angle of the disk, the distance to the source and the ratio of the color to the effective temperature at a local surface of the disk.

For LMC X-3, I applied the GRAD model directly to the spectra, in which the mass and the mass accretion rate were allowed to be free and the other parameters were fixed at plausible values. From the fits, the mass of the compact object in LMC X-3 was estimated to be

$$M \simeq 5.0\left(\frac{d}{50\ \mathrm{kpc}}\right)\left(\frac{T_{col}/T_{eff}}{1.5}\right)^2 f(60°)\,M_\odot. \tag{6.2}$$

The function $f(i)$ ($\equiv g_1(i)^{-1/2}\,g_2(i)^2$ in equation [D.6]), which should be determined by numerical calculations, describes dependence on the inclination angle. This function increases with i; it is normalized to unity at $i = 60°$, and it takes a minimum value of 0.46 at $i = 0°$.

Since the distance to the LMC is well determined ($d = 50$ kpc, Stothers 1983, 1987), ambiguity of the mass in equation (6.2) arises mainly from the values of i and T_{col}/T_{eff}.

The inclination angle is limited to be $i < 70°$ owing to the absence of an X-ray eclipse (Cowley *et al.* 1983); then $f(i)$ in equation (6.2) should be between $f(0°) = 0.46$ and $f(70°) = 1.16$. When $i \simeq 0°$, the spectral shape of the GRAD model approaches that of the MCD model. Since we obtained better fits to the spectrum of LMC X-3 by the GRAD model with $i = 60°$ than by the MCD model, I consider that the inclination of this source is rather close to 60°.

In the inner region of an accretion disk, where most of the X-ray photons are emitted, the color temperature of the emission is larger than the effective temperature since electron-scattering opacity is dominant over the true absorption opacities (e.g. Shakura and Sunyaev 1973). The ratio of the color to the effective temperature, T_{col}/T_{eff}, depends on the structure of the emission region. Extensive studies have been performed for the atmosphere of bursting neutron stars, in which case electron-scattering opacity is also dominant (cf. Ebisuzaki, Hanawa and Sugimoto 1984; London, Taam and Howard 1986). The calculations by Ebisuzaki, Hanawa and Sugimoto (1984) and London, Taam and Howard (1986) have shown that the values of T_{col}/T_{eff} lie between 1.4 – 1.6 in the bursting neutron star atmosphere. The value quoted in equation (6.2), $T_{col}/T_{eff} = 1.5$, is an average of these values. For the emission from optically thick accretion disks, no reliable values are given so far, but two simple cases were discussed by Shakura and Sunyaev (1973). According to them, T_{col}/T_{eff} is ~ 1.6 when the density is decreasing exponentially toward the direction perpendicular to the disk surface, and it is ~ 2.3 for homogeneous medium with a sharp boundary. The exact value of T_{col}/T_{eff} in an accretion disk has to be determined as a function of the radius (or the effective temperature) by solving vertical radiative transfer; this is still an open question. However, from the values for X-ray bursts and the above simple models, I consider T_{col}/T_{eff} is in a range between 1 and 3.

Taking into account these ambiguities in the inclination angle and in T_{col}/T_{eff}, the present mass estimation in equation (6.2) has an uncertainty of a factor of about 2. Thus our result is consistent with the fiducial lower limit of the mass ($9 - 10\ M_\odot$; Cowley *et al.* 1983; Paczyński 1983) obtained from the optical

spectroscopic observations.

For GS2000+25, GX339–4 and LMC X-1, the masses of the compact objects are estimated by converting the best fit MCD model parameters to those of the GRAD model (see equation [D.6]).

For LMC X-1, the distance is well determined at 50 kpc. Substituting $r_{in}\sqrt{\cos i}/d \simeq$ (40 km / 50 kpc), which is the average over three observations in 1987, into equation (D.6), we have

$$M \simeq 8.6 \left(\frac{d}{50\ \mathrm{kpc}}\right) \left(\frac{T_{col}/T_{eff}}{1.5}\right)^2 f(i)\ M_\odot. \tag{6.3}$$

The distance to GS2000+25 is estimated to be ~ 2 kpc from optical photometry (Chevalier and Ilovaisky 1990). The inner radius of the disk was virtually constant at $r_{in}\sqrt{\cos i}\ /\ d \simeq$ (20 km / 2 kpc). Then the mass is estimated to be

$$M \simeq 4.3 \left(\frac{d}{2\ \mathrm{kpc}}\right) \left(\frac{T_{col}/T_{eff}}{1.5}\right)^2 f(i)\ M_\odot. \tag{6.4}$$

For GX339–4, the distance is estimated as ~ 4 kpc from X-ray (Doxsey *et al.* 1979) and optical (Makishima *et al.* 1986) observations. Then using the observed value $r_{in}\sqrt{\cos i}\ /\ d \simeq$ (20 km /4 kpc), one will have

$$M \simeq 4.3 \left(\frac{d}{4\ \mathrm{kpc}}\right) \left(\frac{T_{col}/T_{eff}}{1.5}\right)^2 f(i)\ M_\odot. \tag{6.5}$$

Ebisawa, Mitsuda and Hanawa (1991) applied the above method of the mass estimation to the soft component of two neutron star sources, X1608–522 and X1636–536; the distances to these sources are estimated from observations of the X-ray bursts with mass ejection, whose peak luminosity is considered to be the Eddington limit. From the observed bolometric flux f and the temperature of the MCD model T_{in}, the masses are expressed as

$$M = 1.4 \left(\frac{f}{1.4 \times 10^{-8}\ \mathrm{ergs\,s^{-1}\,cm^{-2}}}\right) \left(\frac{T_{in}}{1.26\ \mathrm{keV}}\right)^{-4}$$

$$\left(\frac{T_{col}/T_{eff}}{1.5}\right)^4 f(i)^2\ M_\odot \qquad (\text{for X1608}-522), \tag{6.6}$$

and

$$M = 2.1 \left(\frac{f}{2.27 \times 10^{-9}\,\mathrm{ergs\,s^{-1}\,cm^{-2}}}\right)\left(\frac{T_{in}}{0.94\,\mathrm{keV}}\right)^{-4} \left(\frac{T_{col}/T_{eff}}{1.5}\right)^{4} f(i)^2\, M_{\odot} \quad \text{(for X1636}-\text{536)}. \qquad (6.7)$$

Note that these masses are systematically smaller than those obtained from the black hole candidates. This is because the observed maximum color temperature T_{in} is systematically higher and the inner radius of the disk $r_{in}\sqrt{\cos i}$ is systematically smaller for the neutron star sources than for black hole candidates. The so-called "ultra-soft" energy spectra of black hole candidates (see section 2.2.4; White and Marshall 1984; White, Kaluzienski and Swank 1984), in comparison with the energy spectra of LMXBs, has been considered to be due to (i) lack of the neutron star components, which are dominant in the higher energy parts, and (ii) lower temperature of the accretion disk components (Makishima 1984; Inoue 1985; Makishima *et al.* 1986). The latter can further considered to be due to the larger masses of the central objects of black hole candidates than those of LMXBs, if the optically thick accretion disks of LMXBs also extend down to 3 r_g.

6.3 The Broad Edge-like Structure in the Hard Component

A broad edge-like absorption structure was commonly observed in the hard component of the blackhole candidates studied in this thesis. In order to illustrate the shape of the broad edge-like structure in the hard component, I made PHA ratios of the observed spectra of GS2000+25, LMC X-1 and GX339–4 to the model spectra without the edge structure, as has been done for Cyg X-1 in figure 5.3. The model spectrum is the multicolor disk plus a power-law with the free parameters determined by fitting the observed spectra while masking the 6 – 20 keV range. In figure 6.1, the PHA ratios for a typical spectrum of GS2000+25, LMC X-1, LMC X-3 and GX339–4 are shown. The deviation from the model is seen for all the spectra including LMC X-3, although the deviation for this source is not statistically very significant (see section 5.2.4).

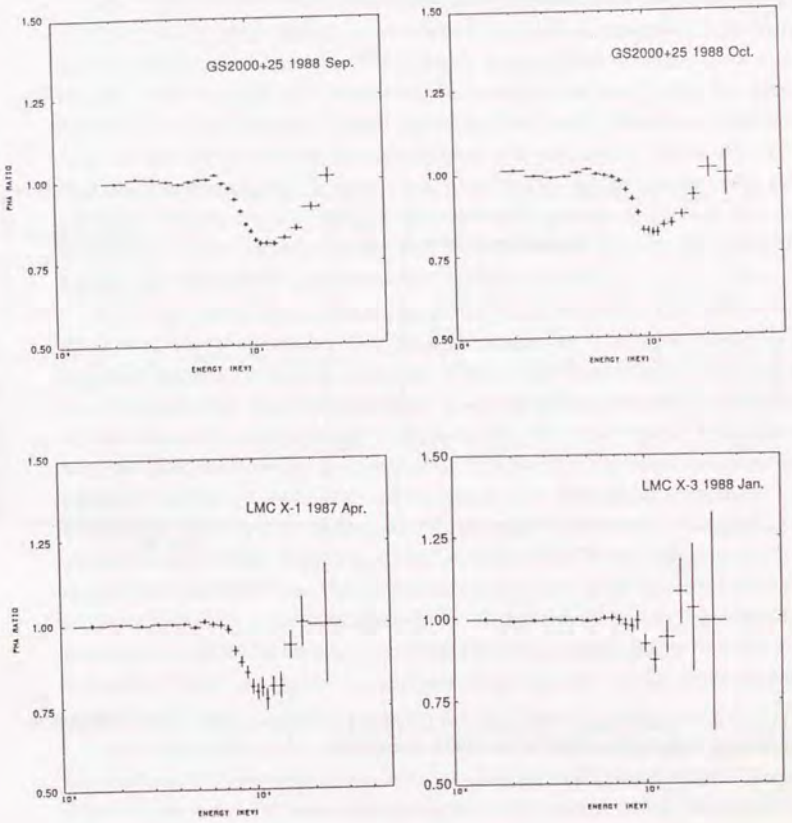

Figure 6.1: PHA ratios of the observed spectra of GS2000+25 (in September and October, 1988), LMC X-1 (in April 1987) and LMC X-3 (in Jan. 1988) to the model spectra without the smeared edge. The model spectrum is the multicolor disk plus a power-law.

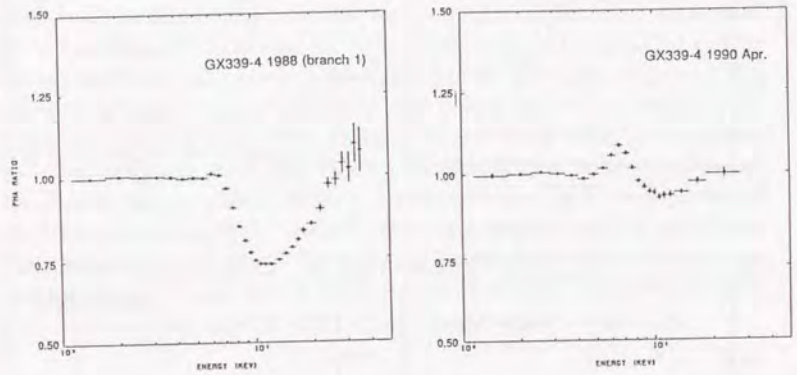

Figure 6.1: (*continued*) PHA ratios of GX339–4 in the soft state (1988 September, branch 1) and in the hard state (1990 April).

It is important that the lower-end energy of the broad edge-like structure (E_{edge} of the smeared edge model) is always around 7 to 8 keV irrespective of the sources, spectral states, and intensities. This strongly suggests that the structure is related to the K-shell absorption of iron, since the energy of the iron K-edge lies between 7.1 keV (neutral iron) and 9.3 keV (hydrogen like iron). Therefore I discuss the origin of the broad edge-like structure assuming it is related to the K-edge of iron. It should be remembered, however, that values of E_{edge} of the smeared edge model obtained from the spectral fitting do not necessarily correspond to the exact energy of the iron K-edge because the shape of the observed broad edge-like structure is significantly distorted from the ordinary K-edge structure.

A problem is how to create the observed broad structure from the ordinary, sharp iron K-edge structure. One possible mechanism is a superposition of two spectral components, one of which has a sharp and deep K-edge structure, and the other does not have the structure. Then the absorption structure of the resultant composite spectrum will be apparently shallow and broad. Two cases can be considered specifically; a superposition of a direct component of the emission (without the K-edge structure) and its reflection or absorption component (with the K-edge structure) by circumstantial optically thick matter. Hereafter, I call above two models the "reflection model" and the "partial absorption model". The ideas of the reflection and the partial absorption are widely applied to the similar broad edge-like structures observed in the spectra of Seyfert I galaxies (e.g., Pounds *et al.* 1989; Matsuoka *et al.* 1990; Piro *et al.* 1990). Below in this section, I examine these two models by applying them directly to the observed energy spectra.

In the reflection model, most photons of the reflected component pass through the reflecting matter with a scattering optical depth of about unity. Thus, the reflected spectrum will have a shape similar to a spectrum after passing through the absorbing matter with a column density of about $N_H \sim 10^{24}$ cm^{-2}, and a large depth of the iron K-edge is expected in the reflected component. A fluorescence iron K-line should accompany the K-shell absorption; hence the intensities of the emission line and of the continuum of the reflected component should be strongly correlated. The spectral shape of the reflected component below $\sim$ 10 keV is mostly determined by the ionization state of elements in the reflector. The

ionization state determines bound-free absorption opacities, as well as the iron K-edge energy, then the ratio of scattering to absorption opacities determines the reflection fraction at a given energy. At higher energies, energy shift due to Comptonization, which does not depend on the ionization state, mainly affects the reflection fraction. For a given ionization state, the overall spectral shape of the composite spectrum is determined by the ratio between the intensities of the direct and reflected components.

Lightman and White (1988) computed reflection spectra from a semi-infinite, plane-parallel, cold medium of cosmic abundance, with an incident spectrum having a power-law shape. The ionization state of the reflecting matter is described by the differential ionization parameter, $d\xi\,/\,dE$, where $\xi\ (\equiv L\,/\,n\,R^2)$ is the conventional ionization parameter. When the incident radiation is a power-law with a photon index of α, the differential ionization parameter is related to the ionization parameter as

$$\frac{d\xi}{dE} = 4\,\pi\,\xi_0\,\left(\frac{h\nu}{\mathrm{eV}}\right)^{-(1+\alpha)}\ \mathrm{ergs\ cm\ s^{-1}\ eV^{-1}}. \tag{6.8}$$

Lightman and White (1988) performed calculations for the reflection matter with $\xi_0 = 0$ (not ionized), 0.02, and 2, and for an incident spectrum with $\alpha = 1.7$ and an upper cutoff energy of 3 MeV. When ξ_0 =0, all the atoms are not ionized and the energy of the iron K-edge is 7.1 keV. For $\xi_0 = 0.02$ and 2.0, iron atoms of different ionization states coexist, so that the iron K-edge structure becomes a blend of different edge structures. The resultant average edge energy is $\sim$ 7.7 keV and $\sim$ 8.5 keV for $\xi_0 = 0.02$ and 2.0, respectively.

In order to study the reflection of incident spectra of different power-law indices, and to estimate the intensity of the iron K-emission line, I made a Montecarlo simulation independently of Lightman and White (1988). The reflector was assumed to be a cold, semi-infinite, plane-parallel slab with cosmic abundance. A power-law spectrum was injected normally to the slab; the energy range of 1 – 100 keV was divided into 1000 bins with an equal width and a total of 10^8 photons were injected into these bins according to the incident power-law spectrum. The Klein-Nishina electron cross section was adopted and the possible energy shifts of input photons through the Comptonization process were taken into account. Incident power-law spectra of photon indices 1.8, 2.0, 2.5 and 2.7 were separately

simulated. The emergent reflected continuum photons and florescence iron emission line photons were counted. In 1 – 60 keV, the "reflection coefficient", that is the ratio of the reflected spectrum to the incident one, was found to be totally independent of the photon index assumed within the statistics of the simulations. The reflection coefficient thus determined and that of Lightman and White (1988) in the case of $\xi_0 = 0$ are in good agreement over 1 – 60 keV.

I selected typical energy spectra for each of the sources to be fitted with the reflection model. I adopted, for hard-state spectra, Cyg X-1 in 1987 (1.2 – 37 keV) and in 1990 (2 – 60 keV), GX339-4 in 1990; for the soft-state spectra, GS2000+25 in 1988 October, LMC X-1 in 1987 April, GX339–4 in 1988 in branch 1. Except for Cyg X-1, the multicolor disk model was necessary in the fits to represent an additional soft component. Since our Montecarlo calculation is not available for an ionized reflector, I have used calculations by Lightman and White (1988) as the reflection model. I derived reflection coefficients from their calculations and then the reflected spectra were made by multiplying the coefficients with the incident power-law spectra. Since an iron line emission is not included in their calculations, I have added an emission line at 6.4 keV with an infinitesimal width. This energy of the line is expected for a K-fluoresence line from neutral, or moderately ionized iron (up to $\sim$ FeXIX). Thus the free parameters of the fits are the normalization and the photon index of the power-law, the fraction of the reflected component in the total spectrum ($\equiv f$), the intensity of the emission line, and the parameters for the multicolor disk and the interstellar absorption. I tried reflection models with the three different ionization states. In table 6.1, the results of the fits with the model which gives the smallest χ^2 value among three are tabulated. In this table, only the parameters related to the hard component are shown. The examples of the fits for Cyg X-1 and LMC X-1 are found in figure 6.2. The intensities of the iron emission lines are shown in two forms of the equivalent widths; equivalent widths to the total and to the reflected spectra. As shown in the table 6.1, the fits for Cyg X-1 in 1990 and GX339–4 in 1988 branch 1 are not accepted. I suspect, however, that these spectra can be also fitted well if ξ_0 can be adjusted with smaller trial intervals. Errors of the parameters are estimated for the spectra which yielded good fits.

For the spectra which have been fitted well by the reflection model, I further

Table 6.1: Application of the reflection model to the hard component[a]

•Hard state spectra	Cyg X-1	Cyg X-1	GX339–4
Parameter	(1987)	(1990)	(1990)
ξ_0	0.02	2	2
Photon index	1.68 ± 0.02	1.58	1.777 ± 0.004
f[b]	0.40 ± 0.05	0.24	0.27 ± 0.02
E. W. of the line (eV) to the continuum	62 ± 20	76	109 ± 19
E. W. of the line (eV) to the reflected component	745 ± 240	1700	1060 ± 180
Reduced χ^2	1.22	2.99	0.85
d.o.f.	41	24	27
•Soft state spectra	GS2000+25	LMC X-1	GX339–4
Parameter	(1988 Oct.)	(1987 Apr.)	(1988 branch 1)
ξ_0	0.02	2	2
Photon index	2.46 ± 0.03	2.44 ± 0.08	2.55
f[b]	0.67 ± 0.10	0.40 ± 0.12	0.38
E. W. of the line (eV) to the continuum	< 17	77 ± 30	94
E. W. of the line (eV) to the reflected component	< 77	630 ± 250	860
Reduced χ^2	1.72	0.88	2.41
d.o.f.	25	25	39

[a] Quoted uncertainties are single-parameter 90 % confidence limit.
[b] Fraction of the reflected component in the total spectrum.

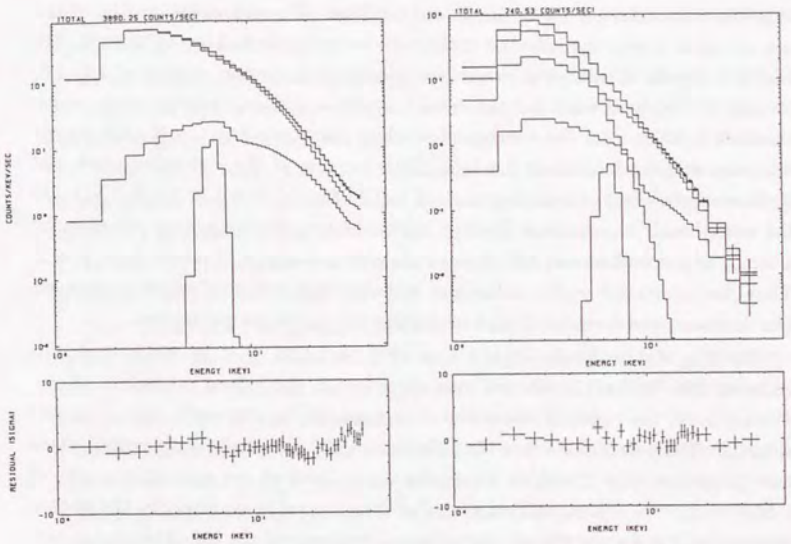

Figure 6.2: Examples of the fits with the reflection model to the hard state spectrum (left; Cyg X-1, 1987) and to the soft state spectrum (right; LMC X-1, 1987 April). Iron emission lines are included at 6.4 keV in the both fits. In the fit for LMC X-1, the multicolor disk model is included to represent the the soft component.

examine consistency of the iron emission line intensities. The expected intensities of the K-fluorescence iron line in the reflection model have been obtained from the Montecarlo simulations for an unionized reflector. The equivalent widths of the iron emission line to the reflected component are estimated to be, 1170, 1120, 910 and 810 eV, for the incident power-law spectra with photon indices of 1.8, 2.0, 2.5 and 2.7, respectively. For the steeper incident spectra, the equivalent width becomes smaller, since the number of incident photons above the K-edge energy decreases relative to that at 6.4 keV. With increase of the ionization state, the K-fluorescence yield of iron increases; it is 0.34 for FeI and 0.49 for FeXXII. On the other hand the reflection fraction below the iron K-edge energy increases by a factor of three when the differential ionization parameter increases from 0 to 2. Thus, the equivalent width of the iron emission line to the reflection component can decrease by a factor of 2 with increasing the ionization parameter.

For Cyg X-1 in 1987, GX339–4 in 1990 and LMC X-1 in 1987 April, the emission line intensities are not inconsistent with the values mentioned above. Furthermore, the ratios of the reflected components to the totals are all smaller than 0.5. Thus, I conclude that the reflection model can consistently explain these energy spectra. On the other hand, the upper limit of the equivalent width of GS2000+25, 77 eV, is significantly smaller than the value expected for the photon index of $\sim$ 2.5, i.e., $\sim$ 910 eV. In addition, the ratio of the reflected component to the total is larger than 0.5. Therefore one needs to consider a more complex situation for GS2000+25 to explain the spectrum with the reflection model. The too large fraction of the reflected component may be explained if the emission of the power-law spectrum is not isotropic and the flux incident on the reflector is larger than that coming toward us directly. As to the lack of the iron emission line, I cannot conjecture any consistent explanations.

Next I examine the partial absorption model. In this model, a part of the emission is absorbed by an optically thick absorber in the line of sight, while the other part is not absorbed but directly observed. Such a situation may be expected, for example, when the optically thick absorbing matter exists in the form of small blobs. The spectral shape of the absorbed component is determined by the optical depth and ionization state of the absorbing matter. The overall spectral shape of the composite spectrum is determined by the ratio of the absorbed component

to the direct one. In the absorbing matter, a fluorescence iron K-line is emitted accompanying the K-absorption. However, a small equivalent width of the emission line is expected because the line emission is isotropic and most photons will escape out of the line of sight.

I tried to fit the six observed energy spectra with the partial absorption model. As in the case for the reflection model, the multicolor disk model, which represents the soft component, and an iron emission line at 6.4 keV are included in the fits.

I first tried a cold, non-ionized absorber and found that this model cannot fit the spectra at all. This is because low energy photons below the iron K-edge energy are considerably absorbed by the lighter elements, and thereby the depth of the iron K-edge relative to the lower energy part cannot become large enough to explain the observed broad edge-like structure.

Then I next tried an ionized absorber. I considered an extreme case in which He-like and H-like iron atoms exist. In such a high ionization state, absorption by most other lighter elements can be neglected. Therefore I modeled absorption only due to iron atoms of three representative ionization states; they are, He-like and H-like ones, whose K-edge energies are 8.8 keV and 9.3 keV respectively, and less ionized ones whose K-edge energy is between 7.1 – 8.8 keV. I made the edge energy of the last ones as a free parameter in the fits. The L-shell absorption was also considered for the iron atoms at this state; the L-edge energy was fixed because it is far below the observational energy range. In the fits with the ionized absorber, the free parameters relevant to the hard components are the photon index of the power-law, the fraction of the absorbed component ($\equiv f$), the K-edge energy of the weakly ionized iron and the column densities of iron atoms for three different ionization states. Results of the fits are tabulated in table 6.2 and examples of the fits are shown in figure 6.3. In table 6.2, the column densities of iron atoms are expressed by the corresponding hydrogen column densities assuming the cosmic abundance. As shown in the table, all the fits are statistically acceptable.

Although the partial absorption model yields good fits to all the observed spectra, this model seems to be physically unrealistic because of the following reason. The total hydrogen column density obtained from the fits (6×10^{24} – 10^{25} cm^{-2}) correspond to an electron scattering optical depth of $\sim$ 4 to $\sim$ 7.5, if cosmic abundance of the iron is assumed. Then few photons are expected to come

Table 6.2: Application of the partial absorption model to the hard component[a]

•Hard state spectra	Cyg X-1	Cyg X-1	GX339–4
Parameter	(1987)	(1990)	(1990)
Photon index	1.601 ± 0.003	1.608 ± 0.003	1.780 ± 0.004
f^b	0.23 ± 0.01	0.19 ± 0.01	0.21 ± 0.03
$E_{\rm edge}$ (keV)	7.1 ± 0.2	7.2 ± 0.2	7.4 ± 0.1
$\log N_H$ ($\rm cm^{-2}$) for low ionized iron	24.72 ± 0.05	24.58 ± 0.06	24.65 ± 0.08
$\log N_H$ ($\rm cm^{-2}$) for He-like iron	23.84 ± 0.67	24.41 ± 0.19	< 24.82
$\log N_H$ ($\rm cm^{-2}$) for H-like iron	24.21 ± 0.26	23.87 ± 0.62	24.57 ± 0.22
$E.\,W.$ of the line (eV) to the continuum	< 30	< 30	48 ± 30
$E.\,W.$ of the line (eV) to the absorbed component	< 400	< 380	630 ± 400
Reduced χ^2	0.58	1.03	0.87
d.o.f.	37	20	23
•Soft state spectra	GS2000+25	LMC X-1	GX339–4
Paramter	(1988 Oct.)	(1987 Apr.)	(1988 branch 1)
Photon index	1.92 ± 0.02	2.39 ± 0.01	2.56 ± 0.05
f^b	0.25 ± 0.02	0.30 ± 0.03	0.31 ± 0.08
$E_{\rm edge}$ (keV)	7.2 ± 0.3	7.4 ± 0.3	7.4 ± 0.2
$\log N_H$ ($\rm cm^{-2}$) for low ionized iron	23.72 ± 0.13	23.95 ± 0.09	24.05 ± 0.09
$\log N_H$ ($\rm cm^{-2}$) for He-like iron	24.78 ± 0.71	23.94 ± 0.55	24.21 ± 0.39
$\log N_H$ ($\rm cm^{-2}$) for H-like iron	24.39 ± 0.45	24.65 ± 0.17	24.93 ± 0.09
$E.\,W.$ of the line (eV) to the continuum	< 20	< 40	< 50
$E.\,W.$ of the line (eV) to the absorbed component	< 80	< 180	< 250
Reduced χ^2	0.77	0.58	0.68
d.o.f.	21	21	35

[a] Quoted uncertainties are single-parameter 90 % confidence limit.
[b] Fraction of the absorbed component in the total spectrum.

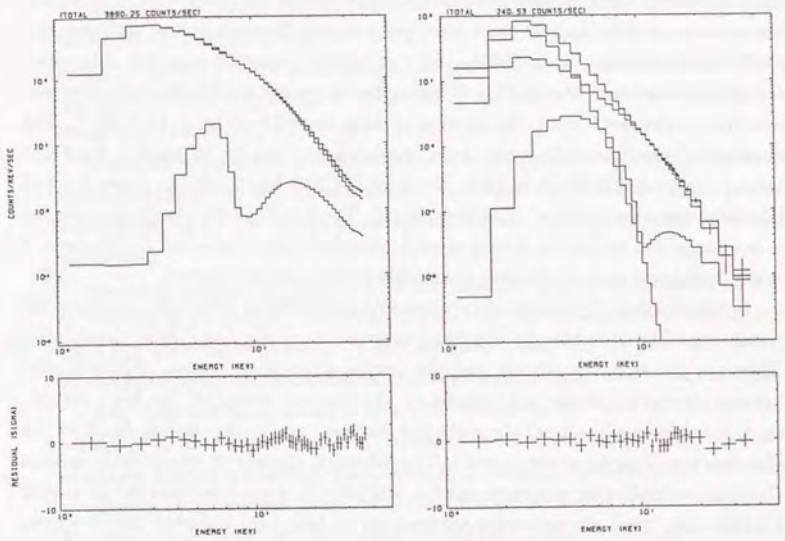

Figure 6.3: Examples of the fits with the partial absorption model (with the ionized absorber, see text) to the hard state spectrum (left; Cyg X-1, 1987) and to the soft state spectrum (right; LMC X-1, 1987 April). In the fit for LMC X-1, the multicolor disk model is included to represent the soft component.

directly through such optically thick absorbers, whereas the ratio of the absorbed component to the total is 0.2 – 0.3. In order to explain the large fraction of the absorbed component, patchy absorbers of such optical thickness have to surround the emission region. In this case, however, a strong florescence iron emission line has to be observed. Inoue (1985, 1989) estimated expected iron line intensities for such a situation. According to him, the equivalent width of the fluorescent iron line to the scattered component is as large as ~ 2 keV for $> 10^{24}$ cm^{-2}. The observed upper limits of possible iron line intensities are by far smaller than this value except for GX 339–4 in 1990. Even for GX 339–4 in 1990, the upper limit of line intensity is only half of what is expected. The fact that the electron scattering is too large can be solved if iron is over abundant by a factor of 5. However, I doubt that such over abundance commonly exist in all the sources.

In this section, I considered two possible mechanisms which may explain the broad edge-like structure in the hard component of the black hole candidates. They are the reflection model and the partial absorption model. Although the partial absorption model can reproduce the spectral shape of the hard component, it is physically unrealistic since the resultant scattering optical depth of the absorber significantly exceeds unity. The reflection model can consistently explain the broad edge-like structure except for GS2000+25. I consider that in the case of GS2000+25, there are unknown mechanisms to hide iron emission line from our view.

6.4 Origin of the Hard Component

In the present study, it has been shown that the intensity of the hard component varies with a large amplitude on various timescales from seconds to several days. It is well known from previous studies that the X-ray intensity of Cyg X-1 and GX339–4 in the hard state exhibits significant variations on a timescale down to milliseconds (see section 2.4). The intensity of the soft component varies on only relatively long timescales of days; it is considered to reflect the mass accretion rate onto the compact object. On the long timescales, the hard component is found to vary independently of the soft component, thus independently of the mass accretion rate.

It was also shown in the present study that the photon index of the hard component is stable at around 2 irrespective of sources and significant changes of intensities, although the photon index may become slightly greater in the soft state (2.0 – 2.5) than in the hard state (~ 1.7). The power-law spectra have been found to extend toward high energies at least up to ~ 300 keV for GS2000+25 (Sunyaev *et al.* 1988; Efremov *et al.* 1989) and to ~ 1 MeV for Cyg X-1 (e.g., Nolan and Matteson 1983).

These three features, i.e. variations on a wide range of timescales, independence of the intensity and the mass accretion rate, and the stability of the power-law index, seem to be key facts for understanding the hard component of black hole candidates.

Mechanisms thus far proposed for the hard X-ray emission from black hole X-ray sources (e.g., Shapiro, Lightman and Eardley 1976) cannot successfully explain these key observational facts. In this section, I shall discuss possible constraints on the hard X-ray emission mechanism imposed by these observational facts.

Two different origins for the fast time variations can be considered. The first possibility is that the variation is caused by small absorbers (blobs) circulating at relatively distant orbits from the black hole. For example, blobs of 10^6 cm diameter circulating at 10^9 cm can cause variations of a millisecond timescale, assuming a 10 $M_\odot$ black hole. However this cannot be relevant to the present case, because the energy dependence of the variation amplitude is not consistent with absorption. The other possibility is that the variations originate from the region close to the black hole where the dynamical timescale is close to or shorter than a millisecond. Assuming a 10 $M_\odot$ black hole, radii smaller than 10^7 cm satisfy this condition. Thus I consider it is probable that the hard component originates in the region close to the black hole. The fact that the power-law emission extends up to 300 keV or 1 MeV supports this idea.

As discussed in section 6.2, in the soft state of black hole candidates, an optically thick accretion disk is considered to extend down to the inner most radius for stable Keplerian orbits. I notice that there are several similarities between the characteristics of black hole candidates in the soft state and those of LMXBs in the normal branch. Firstly, the spectra comprise two components; a soft component and a hard component. The soft component can be represented by the emission

from optically thick accretion disks and the inner most radius of the accretion disk is consistent with the inner most Keplerian orbit (see section 6.2). Secondly, on timescales shorter than about a few hundred seconds, the hard component is highly variable whereas the soft component is relatively stable (compare figure 5.22, 5.26 and 5.33 with figure 2.4). Finally, quasi-periodic oscillations of the centroid frequency of $\sim$ 6 Hz are occasionally observed (see section 2.3.2).

The difference between black hole candidates in the soft state and LMXBs in the normal branch seems to reside only in the spectrum of the hard component; a power-law with a photon index $\sim$ 2 for black hole candidates and a blackbody with a temperature of $\sim$ 2 keV for LMXBs (see section 2.3.1).

In both the cases of LMXBs and black hole candidates, matter circulating along Keplerian orbits in the accretion disk gradually falls inward and the released gravitational energy is eventually converted to thermal and rotational energy. If the accretion disk is optically thick, the thermal energy is radiated away from the disk surface. This corresponds to the soft, multicolor disk component in LMXBs and black hole candidates. In the case of LMXBs, most of the rotational energy of the accreting matter is released when the matter lands on the neutron star surface. The released energy is considered to emerge as the hard, 2 keV blackbody component of LMXBs. A straightforward analogy from LMXBs to black hole candidates leads to the idea that the 2 keV blackbody component in LMXBs is replaced by the power-law component in black hole candidates. From this idea, I consider it is likely that the hard component in the soft state is emitted inside or near the inner boundary of the optically thick accretion disk, i.e., three times the Schwarzschild radius. The essential difference between the accretion flow to a black hole and that to a neutron star is the absence of the solid surface in the former. This may be the reason why the power-law component is emitted inside the optically thick accretion disks in black hole candidates instead of the 2 keV blackbody component in LMXBs.

If the hard component originates just at the vicinity of a black hole, the short-term variation may be explained by the instability of accretion matter in this region. On the contrary, the long-term variations seem to be difficult to be produced in this region. If the intensity of the hard component changes when the same amount of the mass (i.e. fuel of the hard component) is supplied to the

emission region, the missing energy, the energy which was not observed while the intensity was low, has to be explained one of the following three; (1) because of the anisotropy of emission, the energy was emitted in a direction different from toward the earth, (2) the fuel was not consumed and kept in some reservoir, (3) the energy was not converted to X-rays. I do not consider any of the three to be reasonable because of the reasons shown below. (1) The emission of the hard component may be collimated toward the direction of the angular momentum of the accreting matter. However, it is not plausible that the direction of the angular momentum varies randomly. It may vary, but periodically, if it does. (2) The accreted matter corresponding to 10^{38} erg/sec $\times$ 10 days amounts to 10^{23} g. This is close to the mass contained in the whole accretion disk of a radius 10^{11} cm. It is not plausible that such a large amount of mass is kept somewhere. (3) A putative controller which changes the rate of conversion from gravitational energy to X-rays may not have long timescales of a few days if it resides in the vicinity of a black hole.

Thus, I finally consider that the long-term variations of the hard component originate from a different region which is located much further from the black hole. Two possible ways to create long time variations can be considered. First, the short-term variations are created first, then the long-term variations are superposed afterwards. For example, if there is a reflector far from the black hole, the configuration of the reflector, and thus the reflected X-rays, can vary with long time scales. Or, there may be mass flow from the black hole (i.e. jet); the mass flow rate at the vicinity of the black hole varies on short timescales while the X-rays can be emitted from the region relatively far from the black hole. However, in such cases, short time variations will be smeared out by the mechanism which causes the long-term variations. The remaining possibility is, thus, to create long term variations first. A natural explanation is that at outer parts of the accretion disk, the supply rate of the fuel, i.e. mass accretion rate to the hard component, is controlled.

However, the independence between the variations of the soft and the hard components imposes serious difficulty on this model. I would like to conjecture a possible mechanism to overcome this difficulty. Ichimaru (1977) argued that the thermal condition of accretion matter at the outer boundary of accretion disk de-

termines whether the disk becomes totally optically thin and geometrically thick, or totally optically thick and geometrically thin. At the outer boundary of accretion disks around a white dwarf, a hot spot is observed (e.g., Robinson 1976). The hot spot is believed to be a place where the mass from the companion star first collides with the accretion disk and the matter around the spot is heated up. I consider that in the case of the accretion disk around the black hole, at least some part of the matter accreted from the companion star is heated up near the outer boundary and satisfies the condition for formulating the optically thin accretion disk. I thus conjecture that the optically thin flow of matter is formulated together with the optically thick accretion disk and such an optically thin flow supplies fuel for the hard component. The mass flow rate of the optically thin disk can vary independently of the mass flow rate of the optically thick disk. When the matter is heated up to too a high temperature, it will escape from the binary system instead of accreting and the intensity of the hard component decreases. In terms of this two stream model, a transition between the two spectral states is explained by dominance of one of the two flows.

Elementary processes to yield X-ray photons of the hard component with power-law spectra have not been elucidated. I would like to point out here that the power-law energy spectra observed from active galactic nuclei (AGN) and very faint LMXBs have a similar power-law index, although the mass of the central objects, the mass accretion rate, and thus the luminosity is by many orders of magnitude different. This universality of the power-law index is a key observational fact for the understanding of the elementary processes for the power-law X-ray spectra.

6.5 Concluding Remarks

In this thesis, I have studied energy spectra of five black hole candidates Cyg X-1, LMC X-3, GS2000+25, LMC X-1 and GX339–4. The most important results are summarized as follows.

1. I have shown that all the observed energy spectra of these sources can be represented by a unified two component model, which is composed of a soft component and a hard component. The soft component is represented by a model spectrum expected from optically thick accretion disks which have a radially dependent multicolor structure. The derived maximum color temperature of the accretion disks was in the range of 0.4 – 1.2 keV. The hard component is represented by a power-law with a photon index of 1.7 – 2.5, modified by a broad edge-like structure over 7 – 20 keV.

2. The relative intensity of the two spectral components was significantly variable. In some cases, the soft component disappeared; thus the resultant spectrum became hard, like a power-law one. While in other cases the hard component became too weak to be detected; thus the composite spectrum became (ultra-)soft with a power-law like hard-tail. The well-known two spectral states of black hole candidates, the hard (low) state and the soft (high) state, can be understood in this manner in terms of the present two component model.

3. The intensity of the soft component is considered to reflect the mass accretion rate. For LMC X-3 and GS2000+25, the intensity of the soft component varied by a factor of four and two orders of magnitude respectively during the observational periods. The inner radius of the accretion disk determined by the fitting of the model spectrum was nearly constant for each source regardless of the mass accretion rate. I proposed that the constant inner radius of the accretion disk corresponds to the inner most radius of stable Keplerian orbits around a black hole, i.e., three times that of the Schwarzschild radius. In this context, I related the inner radii of the accretion disks obtained by the model fitting of the observed energy spectra to the masses of the compact objects of the sources. I showed that, for LMC X-3, the mass of the compact object thus estimated is consistent with the lower limit of the mass determined from the binary period; for LMC X-1, GS2000+25 and GX339–4, the estimated masses are systematically greater than those of neutron star sources obtained with the same method. This method of the mass estimation includes uncertainties from the distance to the source, the inclination angle of the accretion disk and the ratio between the color and the effective temperature of the emission at the surface of the accretion

disk. This method is, in the near future, expected to be a powerful tool to determine the mass of the compact object in binary X-ray sources and therefore discriminate black holes from neutron stars by X-ray observations.

4. The broad edge-like structure in the hard component was commonly found in all the sources. It should be noted that the same spectral structure has been observed in X-rays from Seyfert I galaxies. The lower end of this structure is always between 7 – 8 keV, which strongly suggests that the structure is related to the K-edge absorption of iron. A partial absorption model can reproduce the spectral shape of the broad edge-like structure, but this model is physically unrealistic since the resultant scattering optical depth of the absorbing matter significantly exceeds unity. Reflection of X-rays by optically thick matter is likely to explain the observed structure. However, for GS2000+25, lack of the expected fluorescence iron emission line still remains as a problem. This problem will have to be worked out by future observations with higher energy resolution. The next Japanese X-ray mission, Astro-D, is expected to play a crucial role in this issue.

5. On a wide range of timescales from seconds to months, the hard component exhibited larger variations than the soft component did. The photon index of the hard component was stable at around ~ 2 in a wide range of variations. A clear correlation was not found between the two components. Absence of a correlation suggests that the hard component is not directly related to the mass accretion rate. The emission mechanism to yield power-law spectra of the stable index irrespective of the mass accretion rate has not been elucidated yet. Investigating the origin of the hard component in black hole candidates will be an important issue in X-ray astronomy in the 1990's.

Appendix A

The Maximum Mass of Neutron Stars

In this appendix, I briefly review the theoretical method of constructing neutron star models and determining an upper limit of neutron star masses.

Neutron stars are compact objects composed mainly of neutrons. The structure of neutron stars is determined by balancing forces due to self-gravitation with the repulsive forces due to neutron degenerate pressure and the nuclear force. The equations which describe the balance, taking account of general relativity, are

$$\frac{dP}{dr} = -\frac{G\rho m}{r^2}\left(1+\frac{P}{\rho c^2}\right)\left(1+\frac{4\pi P r^3}{m c^2}\right)\left(1-\frac{2Gm}{c^2 r}\right)^{-1}, \quad \text{(A.1)}$$

$$m = \int_0^r 4\pi r^2 \rho \, dr, \quad \text{(A.2)}$$

where P and ρ are pressure and density of the star, which are to be functions of radial coordinate r, the function m has the interpretation of the mass inside r. The equation (A.1) is called the Oppenheimer and Volkoff equation (Oppenheimer and Volkoff 1939; referred to as the OV equation in the following). The well-known formula in the Newtonian limit can be recovered from the OV equation by setting c to infinity.

In order to construct models of neutron stars, besides the above equations, an equation of state, which connects P and ρ, is necessary. In fact the main difficulty in studying neutron star models is the uncertainty in the equation of state. Central densities of neutron stars are considered to exceed nucleon density,

$\sim 2.8 \times 10^{14}\,\mathrm{g\,cm^{-3}}$. The state of nuclear matter of such high density is still under current research. Thus, at present there are several possible choices for the equation of state and as many neutron star models as them.

Once the equation of state is fixed, we can construct the model of a neutron star by integrating the OV equation numerically. The boundary condition of the integral at the center is $P(0) = P(\rho_c)$, which is determined by the equation of state for an arbitrary value of central density ρ_c, and $m(0) = 0$. Integrating the OV equation outward, the radius of the star R is given as the radial coordinate where pressure becomes 0 and the mass M is given by $M = m(R)$. Thus both the mass and the radius of a neutron star are determined by the parameter ρ_c.

The mass of a neutron star thus obtained does not increase with ρ_c monotonically. With increasing density the equations of state of degenerate matter become relativistic. The adiabatic index Γ ($P \propto \rho^{\Gamma}$) then approaches to 4/3 from the non-relativistic value of 5/3. On the other hand the condition for the dynamical stability of stars in general relativity is

$$\Gamma > \frac{4}{3} + O\Big(\frac{GM}{c^2 R}\Big). \tag{A.3}$$

In the case of neutron stars, as the second term of the equation (A.3) is not negligible, neutron stars with large enough ρ_c, and thus with $\Gamma \approx 4/3$ is dynamically unstable. Above a certain critical value of ρ_c, say ρ_c^{crit}, the instability causes $dM/d\rho_c$ to become negative. The maximum mass of a neutron star, therefore, is attained with the ρ_c^{crit}.

The original work on modelling a neutron star (Oppenheimer and Volkoff 1939) assumed the neutron star to be an ideal gas composed of free neutrons. This is an obviously incorrect assumption, therefore their value of an upper limit of $0.71\,M_\odot$ is not correct. Models with more realistic equations of state yield larger upper limits because nuclear interactions work as a repulsive force. The upper limits depend on the adopted equations of state; stiffer equations of state give larger upper limits, softer equations of state give smaller ones.

It is worth noting, however, that irrespective of the uncertainty of equations of state, an upper limit can be obtained from simple assumptions (Rhoads and Ruffini 1974). The assumptions are (i) general relativity is correct; (ii) causality holds (in other words, sound velocity does not exceed light velocity, *i.e.*, $dP/d\rho \leq c^2$), (iii) pressure is a monotonically nondecreasing function of the density, *i.e.*, $dP/d\rho \geq 0$ and (iv) the equation of state below a certain matching density is known. Rhoads and Ruffini (1974) concluded that the upper limit is 3.2 $M_\odot$, adopting the conservative matching density and the equation of state below it. As these assumptions are reasonably sound, this value should be a reliable upper limit of neutron star masses.

Table A.1: Neutron star maximum masses from selected equations of state

Equation of state	$M_{\max}/M_\odot$	$\rho_c(\mathrm{g\,cm^{-3}})$
A	1.66	$4. \times 10^{15}$
B	1.41	$6. \times 10^{15}$
C	1.85	$3. \times 10^{15}$
D	1.65	$4. \times 10^{15}$
E	1.73	$3. \times 10^{15}$
F	1.46	$5. \times 10^{15}$
G	1.36	$6. \times 10^{15}$
H	0.71	$4. \times 10^{15}$
I	2.45	$2. \times 10^{15}$
J	2.70	$1. \times 10^{15}$
K	1.96	$2. \times 10^{15}$
L	2.58	$2. \times 10^{15}$
M	2.39	$2. \times 10^{15}$

Maximum masses of neutron stars calculated from 12 different equations of state are tabulated in table A.1 from Hartle (1978). In table A.1, H is the free neutron gas equation of state adopted in Oppenheimer and Volkoff (1939). See Hartle (1978) for the other equations of state and Arnett and Bowyes (1977) for the discussion and references to the original literature. The maximum masses range from 1.36 $M_\odot$ to 2.70 $M_\odot$, most of them are within the range 1.6 $M_\odot$ to 2.5 $M_\odot$.

Appendix B

Masses of Compact Stars in X-ray Binaries

When stars are in binaries, their masses can be determined using Kepler's Third Law. Suppose that the mass of a compact object (a neutron star or a black hole) in a binary we are interested in to be M_X, mass of the companion M_C, and the inclination angle of the orbital plane i. The mass functions for M_X and M_C are respectively defined as

$$f_X \equiv \frac{(M_C \sin i)^3}{(M_X + M_C)^2}, \tag{B.1}$$

and

$$f_C \equiv \frac{(M_X \sin i)^3}{(M_X + M_C)^2}. \tag{B.2}$$

Using Kepler's Third Law, $(2\pi/P_{orb})^2 = G(M_X + M_C)/a^3$, where P_{orb} is the orbital period and a is the semimajor axis of the orbit of the relative motion, f_X and f_C are rewritten as,

$$f_X = \frac{4\pi^2 (a_X \sin i)^3}{G P_{orb}^2} = \frac{K_X^3 \, P_{orb} \, (1-e^2)^{3/2}}{2\pi G}, \tag{B.3}$$

$$f_C = \frac{4\pi^2 (a_C \sin i)^3}{G P_{orb}^2} = \frac{K_C^3 \, P_{orb} \, (1-e^2)^{3/2}}{2\pi G}. \tag{B.4}$$

Where, $a_X(= M_C \, a/\,(M_X + M_C)\,)$ is the semimajor axis of the orbit of the compact object in the center of mass frame, K_X is the semiamplitude of the radial velocity

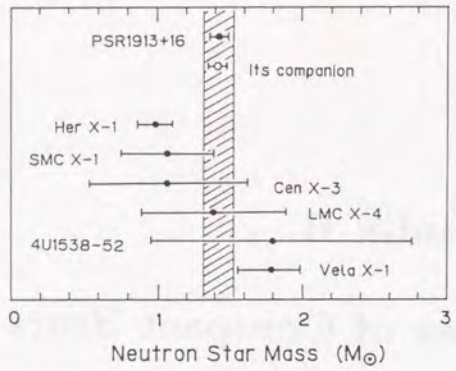

Figure B.1: Empirically determined neutron star masses of binary X-ray pulsars. The masses of PSR 1913+16, a binary radio pulsar, and its companion are shown together. The hatched region represents the range $1.42 \pm 0.10 M_\odot$. The figure is adopted from Nagase (1989)

of the compact object, $a_C(= M_X\, a/(M_X + M_C))$ and K_C have the same meaning for the companion star and e is the eccentricity of the orbit.

If the compact object is an X-ray pulsar, from pulse arrival time analysis (see Nagase 1989, for a review), the intrinsic pulse period, its time derivatives and the orbital parameters of the binary are obtained. The orbital parameters include $a_X \sin i$, P_{orb} and e, which readily give f_X through the equation (B.3). Spectroscopic observations of the companion star yields K_C, then the mass ratio,

$$q \equiv \frac{M_X}{M_C} = \frac{K_C\, P_{orb} \sqrt{1-e^2}}{2\pi\, a_X \sin i} \tag{B.5}$$

is obtained. From the equations (B.1) and (B.5), one has

$$M_X = \frac{f_X\, q\, (1+q)^2}{\sin^3 i}. \tag{B.6}$$

It is possible to estimate $\sin i$ using the information of X-ray eclipse (e.g., see Nagase 1989), thus M_X is determined from the equation (B.6). Masses of the neutron stars in six X-ray pulsars thus determined are shown in figure B.1.

In the case of black hole candidates, because the compact objects provides scarcer information than in the case of X-ray pulsars, the masses of the compact objects cannot be uniquely determined. However, in some cases, it is possible to determine the lower limits of the masses of the compact objects from observations of the companion stars.

Spectroscopic observations of the companion star supply K_C, P_{orb} and e (usually too small to be determined), thus one has f_C through equation (B.4). In the remarkable case of A0620–00 (McClintook and Remillard 1986), f_C thus obtained was $3.18 \pm 0.16 M_\odot$. Then the lower limit of the compact star is readily determined to be $3.2 M_\odot$ independent of the distance to the source and insensitive to the assumed mass of the companion star. Except such a lucky case, the mass M_C, and the radius in some cases, of the companion star are constrained by its observational characteristics such as luminosity and spectral type. A reasonable assumption that the companion star does not exceed its Roche lobe can also constrain the radius. Lack of an X-ray eclipse, combined with the radius of the companion star, provides information of the inclination, $\sin i$. From f_C, M_C and $\sin i$, one can impose lower limits on M_X through equation (B.2).

Appendix C

The Smeared Edge Model

When an X-ray spectrum, expressed as a function $f(E)$, is affected by absorption of neutral iron including the K-edge structure, the emergent spectrum $f'(E)$ is written as,

$$f'(E) = f(E)\, e^{-\sigma(E)\, N_{Fe}} \tag{C.1}$$

$$= f(E)\, \exp\left(-C_0(E)\, N_H\, 10^{-4.4-24}\right) \tag{C.2}$$

where,

$\sigma(E)$ = Cross section of iron (cm^2),

N_{Fe} = Iron column density (cm^{-2}),

N_H = Hydrogen column density converted from N_{Fe} assuming the solar abundance (cm^{-2})

and

$$\log_e C_0(E) = \begin{cases} 13.6696 - 2.39195 \log_e E - 0.137348 (\log_e E)^2 & (E < E_{\mathrm{edge}}) \\ 14.3456 - 1.23491 \log_e E - 0.418785 (\log_e E)^2 & \\ \quad +0.0321662 (\log_e E)^3 & (E > E_{\mathrm{edge}}). \end{cases} \tag{C.3}$$

The iron cross section was adopted from McMaster *et al.* (1970).

In chapter 5, I used "the smeared edge model" to reproduce the spectral shape of the broad edge-like structure found in the hard components of the black hole cadidates. This is a modification of the above normal edge model taking account of a smearing effect. In this model, instead of $C_0(E)$ in equation (C.2), the following

$C_1(E)$ is adopted.

$$C_1(E) = \begin{cases} 0 & (E < E_{\rm edge}) \\ C_0(E)\left\{1 - \exp(-\frac{E-E_{\rm edge}}{E_W})\right\} & (E > E_{\rm edge}). \end{cases} \quad \text{(C.4)}$$

In equation (C.4), absorption by L-electrons is not considered thus $C_1 = 0$ for $E < E_{\rm edge}$ and E_W describes the effect of the smearing for $E > E_{\rm edge}$. In practical use of the smeared edge model, N_H, $E_{\rm edge}$ and E_W are made free parameters. These parameters should not be taken as real physical quantities, since the mathematical form of equation (C.4) is a mere invention to reproduce the observed spectral shape and therefore has no physical bases. Discussion concerning the physical meaning and interpretation of the smeared edge can be found in section 6.3.

In figure C.1, the effects of the smeared edge model are illustrated for the case that the model is applied to a power-law spectrum.

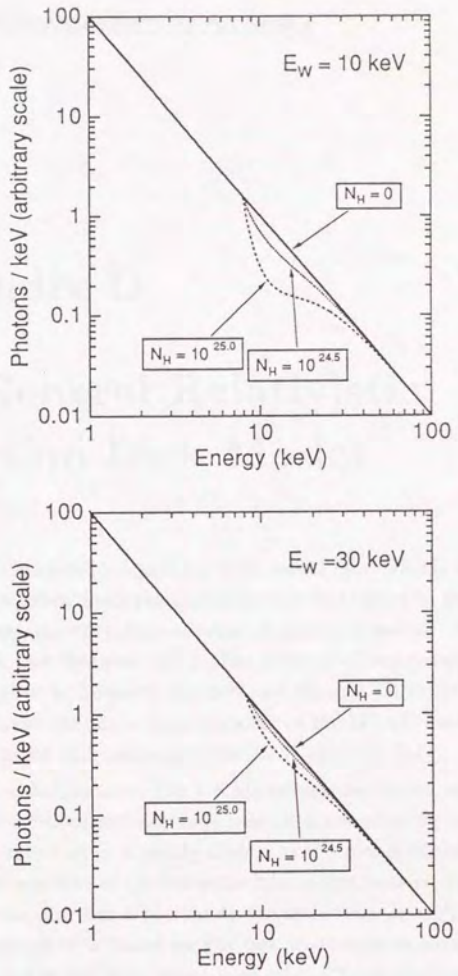

Figure C.1: Resultant spectra when the smeared edge model is applied to a power-law spectrum. E_W is 10 keV in the upper panel and 30 keV in the lower. In both panels, the photon-index is 2.0 and $E_{\rm edge}$ is 8.0 keV. The cases that N_H is $10^{24.5}$ and $10^{25.0}$ cm^{-2} are shown together with the case of no absorption ($N_H = 0$) for comparison.

Appendix D

The General Relativistic Accretion Disk Model

The General Relativistic Accretion Disk model (the GRAD model) is a model of the X-ray emission from geometrically thin and optically thick accretion disks around compact objects taking account of general relativity (Hanawa 1989; Ebisawa, Mitsuda and Hanawa 1991). The method of computations of the GRAD model is described in Ebisawa, Mitsuda and Hanawa (1991) in detail. In this appendix, I describe the main characteristics of the GRAD model and compare it with the multicolor disk model (section 2.3.1; equation [2.7]).

The main assumptions of the GRAD model are (i) the accretion disk is rotating around a Schwarzschild black hole or a non-rotating neutron star and is geometrically thin and in a steady state, (ii) the radius of the inner edge of the disk is three times that of the Schwarzschild radius, that is, $6\,GM\,/\,c^2$ and (iii) a local part of the disk has a blackbody-like spectrum, $I_\nu = (T_{eff}/T_{col})^4\ B_\nu(T_{col})$. The final assumption is based on the fact that electron scattering is dominant in the inner part of the disk, where most of the X-ray photons are emitted (see, e.g., Hayakawa 1985). From the computations of bursting neutron star atmospheres, it is well-known that the color temperature of the emission, T_{col}, becomes higher than the effective temperature, T_{eff}, when electron scattering dominates (cf. Ebisuzaki, Hanawa and Sugimoto 1984; London, Taam and Howard 1986). The value of T_{col}/T_{eff} used in section 5.2.3, 1.5, is based on these computations.

The GRAD model has five parameters; the mass of the compact object, M, the mass accretion rate, $\dot{M}$ the distance to the source, d, the inclination angle of the disk to the line of sight, i, and the ratio of the color to the effective temperature of the optically thick emission at the disk surface, T_{col}/T_{eff}. Among them, $\dot{M}$ and d are uniquely related to each other, hence the number of free parameters is effectively four. The integrated energy flux of the GRAD model spectrum is expressed as

$$f \equiv \int h\nu\, f_\nu(M, \dot{M}, d, i, T_{col}/T_{eff})\, d\nu \quad \text{(D.1)}$$

$$= \frac{(1-2\sqrt{2}/3)\dot{M}c^2}{4\pi d^2}\, g_1(i) \quad \text{(D.2)}$$

$$= 6.74\times10^{-9}\left(\frac{\dot{M}}{10^{18}\mathrm{g\ s^{-1}}}\right)\left(\frac{d}{8\,\mathrm{kpc}}\right)^{-2} g_1(i)\ \mathrm{ergs\ cm^{-2}\ s^{-1}}, \quad \text{(D.3)}$$

where c, h, ν, and $g_1(i)$ are the speed of light, the Planck constant, the frequency of the X-ray photon and a function of i respectively. The value of $g_1(i)$ is 1.01 for $i = 60°$ and larger for smaller i as shown in figure D.1. The average X-ray energy is,

$$\langle h\nu\rangle \equiv \frac{\int h\nu\, f_\nu(M, \dot{M}, d, i, T_{col}/T_{eff})\, d\nu}{\int f_\nu(M, \dot{M}, d, i, T_{col}/T_{eff})\, d\nu} \propto \dot{M}^{1/4}\, M^{-1/2}\, T_{col}/T_{eff}, \quad \text{(D.4)}$$

since the luminosity is proportional to the accretion rate and the area is proportional to the square of the mass.

Comparison of the GRAD model with the blackbody, the multicolor disk and the Sunyaev-Titarchuk Comptonization model (Sunyaev and Titarchuk 1980; equation [2.10]) was made by Ebisawa, Mitsuda and Hanawa (1991). In that work, computing a convolution of the GRAD model, hypothetical interstellar absorption and the response function of the LAC, we created simulation spectra of the GRAD model for various values of M, $\dot{M}$ and i. We fitted these simulation spectra with the blackbody, the multicolor disk and the Sunyaev and Titarchuk Comptonization model and then obtained best fit parameters. Furthermore, we derived conversion formulae which connects these best fit parameters and the GRAD parameters.

It was shown that the blackbody does not fit the GRAD model spectra at all. The multicolor disk gives almost the same spectral shape as the GRAD model

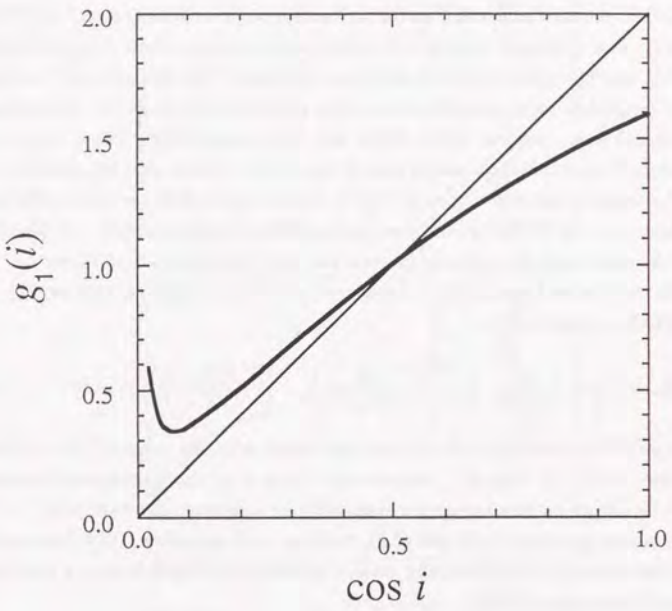

Figure D.1: The thick curve denotes $g_1(i)$ in the equation (D.2) as a function of $\cos i$. The thin curve denotes $2\cos i$, which is the value of $g_1(i)$ in the Newtonian limit. The difference between the thin and thick curves are due to the effects of the general relativity. The figure is adopted from Ebisawa, Mitsuda and Hanawa (1991)

spectra when the inclination angle is nearly 0°, however, difference between the two models becomes noticeable as the inclination angle becomes larger ($i \gtrsim 30°$; figure D.2). The difference should be ascribed to relativistic effects such as Doppler boosting and the gravitational bending of the light. The deviation of the emission of relativistic accretion disks from that of Newtonian disks has been already pointed out (e.g., Luminet 1979; Fukue and Yokoyama 1989)[1]. The Sunyaev and Titarchuk Comptonization model can fit the GRAD model spectra satisfactorily even for large inclination angles ($i \approx 60°$); this is mainly because this model have the same number of free parameters as the GRAD model spectra; on the other hand the disk black body model has one less free parameters than those.

The conversion formula which connects the multicolor disk parameter, T_{in}, and the GRAD parameters is

$$T_{\rm in} = 1.47 \left(\frac{M}{1.4M_\odot}\right)^{-1/2} \left(\frac{\dot{M}}{10^{18}\,{\rm g\,s^{-1}}}\right)^{1/4} \left(\frac{T_{col}/T_{eff}}{1.5}\right) g_2(i)\,{\rm keV}, \qquad \text{(D.5)}$$

where $g_2(i)$ is a function to be determined empirically. Its value is 0.76, 0.85 and 1.00 for $i = 0°$, 30° and 60°, respectively. Note that the temperature becomes higher for larger inclination angles even with the constant accretion rate.

Equating equation (D.2) and (2.9), together with equation (D.5), leads to the important formula to estimate the mass of the compact object from the multicolor disk parameter, $r_{in}\sqrt{\cos i}$;

$$M = 2.15 \left(\frac{r_{in}\sqrt{\cos i}}{10\,{\rm km}}\right) \left(\frac{T_{col}/T_{eff}}{1.5}\right)^2 g_1(i)^{-1/2}\, g_2(i)^2\, M_\odot. \qquad \text{(D.6)}$$

The function $g_1(i)^{-1/2}\ g_2(i)^2$ is 1.00 at $i = 60°$ and has its minimum, 0.46, at $i = 0°$.

[1]The relativistic effects are visually illustrated in the simulated monochrome (Luminet 1979) or color (Fukue and Yokoyama 1989) photographs of the accretion disks.

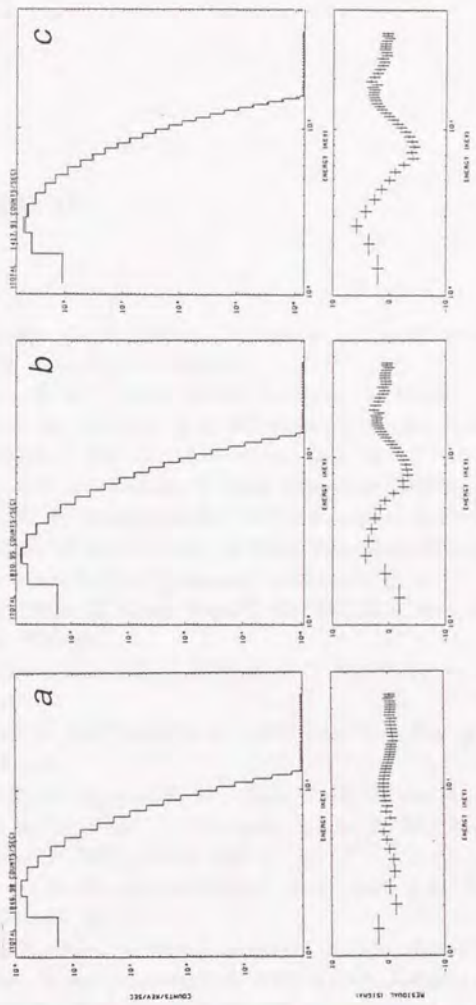

Figure D.2: Comparison between the GRAD model and the multicolor disk model. Simulation spectra of the GRAD model were fitted with the multicolor disk model. The parameters of the GRAD model spectra are, $M = 3.0M_\odot$, $\dot{M} = 10^{18}\,{\rm g\,s^{-1}}$, $T_{col}/T_{eff} = 1.5$ and $i = 0°$ (a), 30° (b) and 60° (c).

Reference

Abramowicz, M. A., Czerny, B., Lasota, J. P. and Szuszkiewicz, E. 1988, *Astrophys. J.*, **332**, 646.

Apparao, K. M. V. 1984, *Astron. Astrophys.*, **375**, 139.

Argue, A. N., Jauncey, D. L., Morabito. D. D. and Preston, R. A. 1984, *Mon. Not. Roy. Astron. Soc.*, **209**, 11.

Argue, A. N. and Sullivan, C. 1982, *Observatory*, **102**, 4.

Arnett, W. D. and Bowers, R. L. 1977, *Astrophys. J. Suppl.*, **33**, 415.

Balucinska, M. and Hasinger, G. 1989, *Proc. 23rd ESLAB Symp. on two topics in X-ray astronomy*, vol.1,p.269, ESA.

Barr, P.,White ,N. E. and Page, C. G. 1985, *Mon. Not. Roy. Astron. Soc.*, **216**, 65p.

Bisnovatyi-Kogan, G. S. and Blinnikov, S. I. 1977, *Astron. Astrophys.*, **59**, 111.

Blair, D. G. and Candy, B. N. 1985, *Mon. Not. Roy. Astron. Soc.*, **212**, 219.

Bradt, H. V., Apparao, K. M., Clark, G. W., Dower, R., Mayer, W., Doxsey, R., Hearn, D., Jernigan, J., Joss, P., McClintock, J. and Walter, F. 1977, *Nature*, **269**, 21.

Bradt, H. V. D. and McClintock, J. E. 1983, *Ann. Rev. Astron. Astrophys.*, **21**, 13.

Coe, M. J., Engel, A. R. and Quenby, J. J. 1976, *Nature*, **259**, 544.

Chevalier, C. and Ilovaisky, S. A. 1990, *Astron. Astrophys.*, **238**, 163.

Clerk, G. W., Woo, J. W., Nagase, F., Makishima, K. and Sakao, T. 1990, *Astrophys. J.*, **353**, 374.

Cowley, A. P., Crampton, D., Huchtings, J. B., Remillard, R. and Penfold, J. E. 1983, *Astrophys. J.*, **272**, 118.

Dotani, T. 1988, Ph. D. Thesis, University of Tokyo (*ISAS Research Note* **418**, The Institute of Space and Astronautical Science, Japan).

Doxsey, R., Grindlay, J., Griffiths, R., Bradt, H., Johnston, M., Leach, R., Schwartz, D. and Schwartz, J. 1979, *Astrophys. J. Lett.*, **228**, L67.

Ebisawa, K., Mitsuda, K. and Hanawa, T. 1991, *Astrophys. J.*, **367**, 213.

Ebisawa, K., Mitsuda, K. and Inoue, H. 1989, *Publ. Astron. Soc. Japan*, **41**, 59.

Ebisuzaki, T., Hanawa, T. and Sugimoto, D. 1984, *Publ. Astron. Soc. Japan*, **36**, 551.

Efremov, V. V., Grebenev, S. A., Kaniovsky, A. S.,Kuznetson, A. V.,Lapshov, I. Yu., Sunyaev, R. A., Smith, A., Parmar, A., Doebereiner, S., Englhauser, J., Reppin, C., Pietch, W., Trümper, J., Voges, W., Kendziorra, E., Maisack, M., Mony, B. and Staubert, R. 1989, *Proc. 23rd ESLAB Symp. on two topics in X-ray astronomy*, vol.1,p.15, ESA.

Elvis, M., Page, C. G., Pounds, K. A., Ricketts, M. J. and Turner, M. J. L. 1975, *Nature*, **257**, 656.

Fabian, A, C. 1988, in *Physics of Neutron Stars and Black Holes*, p.191, ed. Y. Tanaka, Univ. Acad. Press. , Tokyo, Japan.

Fabian, A. C., Guilbert, P. W., Motch, C., Ricketts, M., Ilovaisky, S. A. and Chevalier,C. 1982, *Astron. Astrophys.*, **111**, L9.

Fukue, J. and Yokoyama, T. 1988, *Publ. Astron. Soc. Japan*, **40**, 15.

Galeev, A. A., Rosner, R. and Vaiana, G. S. 1979, *Astrophys. J.*, **229**, 318.

Giacconi, R., Gursky. H., Paolini, F. R. and Rossi, B. B. 1962, *Phys. Rev. Lett.* , **9**, 439.

Gold, T. 1968, *Nature*, **218**, 731.

Grindlay, J., Gursky, H., Schnopper, H.,Parsignault, D. R., Heise, J., Brinkman, A. C. and Schrijver, J. 1976, *Astrophys. J. Lett.*, **205**, L127.

Gursky, H., Bradt, H., Doxsey, R., Schwartz, D. A., Schwarz, J., Dower, R., Fabbiano, G.,Griffiths, R. E., Johnston, M., Leach, R., Ramsey, A. and Spada, G. 1978, *Astrophys. J.*, **223**, 973.

Hanawa, T. 1989, *Astrophys. J.*, **341**, 948.

Hansen, C. J and Van Horn, H. M. 1975, *Astrophys. J.*, **195**, 735.

Hartle, J. B. 1978, *Phys. Rep.*, **46**, 201.

Hasinger, G. 1988, in *Physics of Neutron Stars and Black Holes*, p. 97, ed. Y. Tanaka, Univ. Acad. Press. , Tokyo, Japan.

Hayakawa, S. 1985, *Phys. Rep.*, **121**, 317.

Hayashida, K. 1989, Ph. D. Thesis, University of Tokyo.

Hayashida, K., Inoue, H., Koyama, K., Awaki, H., Takano, S., Tawara, Y., Williams, O. R., Denby, M., Stewart, G. C., Turner, M. J. L., Makishima K. and Ohashi, T. 1989, *Publ. Astron. Soc. Japan*, **41**, 373.

Hewish, A.,Bell, S. J., Pilkington, J. D. H., Scott, P. H. and Collins, R. A. 1968, *Nature*, **217**, 709.

Hjellming, R. M., Calovini, T. A. and Córdova, F. A. 1988, *IAU circ.*, No.4607.

Hoffman, J. A., Marshall, H. L. and Lewin, W. H. G. 1978, *Nature*, **271**, 709.

Hoshi, R. 1984, *Publ. Astron. Soc. Japan*, **36**, 785.

Hoshi, R. 1985, in *Galactic and Extragalactic Compact X-ray sources*, p. 143, ed. Y. Tanaka and W. H. G. Lewin, Institue of Space and Astronautical Science, Tokyo, Japan

Hutchings, J. B., Crampton, D. and Cowley, A. P. 1983, *Astrophys. J. Lett.*, **275**, L43.

Ichimaru, S. 1977, *Astrophys. J.*, **214**, 840.

Ilovaisky, S. A., Chevalier, C., Motch, C. and Chiappetti, L. 1986, *Astron. Astrophys.*, **164**, 67.

Inoue, H. 1985, *Space Sci. Rev.* , **40**, 317.

Inoue, H. 1989, *Proc. 23rd ESLAB Symp. on two topics in X-ray*

astronomy, vol.2,p.783, ESA.

Johnston, M. D., Bradt, H. V. and Doxsey, R. E. 1979, *Astrophys. J.*, **233**, 514.

Jones, C. 1977, *Astrophys. J.*, **214**, 856.

Joss, P. C. and Rappaport, S. A. 1984, *Ann. Rev. Astron. Astrophys.*, **22**, 537.

Kakubari, K., Hoshi, R. and Asaoka, I. 1989, *Publ. Astron. Soc. Japan*, **41**, 1035.

Kaluzienski, L. J., Holt, S. S., Boldt, E. A. and Serlemitsos, P. J. 1977, *Astrophys. J.*, **212**, 203.

Kawai, N., Matsuoka, M., Pan, H. C. and Stewart, G. C. 1989, *Publ. Astron. Soc. Japan*, **41**, 491.

Kitamoto, S. 1989, *Proc. 23rd ESLAB Symp. on two topics in X-ray astronomy*, vol.1,p.231, ESA.

Kitamoto, S.,Takahashi, K.,Yamashita, K., Tanaka, Y. and Nagase, F. 1990, *Publ. Astron. Soc. Japan*, **42**, 85.

Leibowitz, E. M. 1984, *Mon. Not. Roy. Astron. Soc.*, **210**, 279.

Lewin, W. H. G., Penninx, P., van Paradijs, J., Damen, E., Sztajno, M., Trümper, J. and van der Klis, M. 1987, *Astrophys. J.*, **319**, 893.

Lewin, W. H. G., van Paradijs, J. and van der Klis, M. 1988, *Space Sci. Rev.* , **46**, 273.

Li, F. K. and Clark, G. W. 1974, *Astrophys. J. Lett.*, **191**, L27.

Liang, E. P. and Nolan, P. L. 1984, *Space Sci. Rev.* , **38**, 353.

Liang, E. P. T. and Thompson, A. 1979, *Mon. Not. Roy. Astron. Soc.*, **189**, 421.

Liang, E. P. T. and Price, R. H. 1977, *Astrophys. J.*, **218**, 247.

Lightman, A. P. and White, T. R. 1988, *Astrophys. J.*, **335**, 57.

Ling, J. C., Mahoney, W. A., Wheaton, WM. A. and Jacobson, A. S. 1987, *Astrophys. J.*, **321**, L117.

London, R. A., Taam, R. E. and Howard, W. M. 1986, *Astrophys. J.*, **306**, 170.

Luminet, J. P. 1979, *Astron. Astrophys.*, **75**, 228.

Lyne, A. G., Manchester, R. N. and Taylor, J. H. 1985, *Mon. Not. Roy. Astron. Soc.*, **215**, 613.

Maejima, Y., Makishima, K., Matsuoka, M., Ogawara, Y., Oda, M., Tawara, Y. and Doi, K. 1984, *Astrophys. J.*, **285**, 712.

Makino, F. 1988, *IAU Circ.*, No. 4587.

Makino, F. and Astro-C team, 1987, *Astrophys. Letters Commun.*, **25**, 223.

Makishima, K. 1984, in *X-ray Astronomy '84*, p.165, ed. M. Oda and R. Giacconi, Intitute of Space and Astronautical Science, Tokyo, Japan.

Makishima, K. 1988, in *Physics of Neutron Stars and Black Holes*, p.175, ed. Y. Tanaka, Univ. Acad. Press. , Tokyo, Japan.

Makishima, K., Ishida, M., Ohashi, T., Dotani, T., Inoue, H., Mitsuda, K., Tanaka, Y., Turner, M. J. L. and Hoshi, R. 1989, *Publ. Astron. Soc. Japan*, **41**, 531.

Makishima, K., Maejima, Y., Mitsuda, K., Bradt, H. V., Remillard, R. A., Tuohy, I. R., Hoshi, R. and Nakagawa, M. 1986, *Astrophys. J.*, **308**, 635.

Makishima, K., Mihara, T., Ishida, M., Ohashi, T., Sakao, T., Tashiro, M., Tsuru, T., Kii, T., Makino, F., Murakami, T., Nagase, F., Tanaka, Y., Kunieda, H., Tawara, Y., Kitamoto, S., Miyamoto, S., Yoshida, A. and Turner, M. J. L. 1990a, *Astrophys. J. Lett.*, **365**, L59.

Makishima, K. and Mitsuda, K. 1985, in *Galactic and Extragalactic Compact X-ray sources*, p. 127, ed. Y. Tanaka and W. H. G. Lewin, Institue of Space and Astronautical Science, Tokyo, Japan

Makishima, K. and Miyamoto, S. 1988, *IAU Circ.*, No. 4653.

Makishima, K., Ohashi, T., Kawai, N., Matsuoka, M., Koyama, K., Kunieda, H., Tawara, Y., Ushimaru, N., Corbet, R. H. D., Inoue, H., Kii, T., Makino, F., Mitsuda, K., Murakami, T., Nagase, F., Ogawara, Y., Tanaka, Y., Kitamoto, S., Miyamoto, S., Tunemi, H. and Yamashita, K. 1990b, *Publ. Astron. Soc. Japan*, **42**, 295.

Market, T. H., Canizares, C. R., Clark, G., W., Lewin, W. H. G.,

Schnopper, H. W. and Sprott, F. 1973, *Astrophys. J. Lett.*, **184**, L67.

Markert, T. H. and Clark, G. W. 1975, *Astrophys. J. Lett.*, **196**, L55.

McMaster, W. H., Grande, N. K. D., Mallet, J. H. and Hubbell, J. H., 1970, *Compilation of X-ray Cross Sections, UCRL-50174.*

Matsuoka, M., Piro., L., Yamauchi, M. and Murakami, T. 1990, *Astrophys. J.*, **361**, 440.

McClintock, J. E. and Remillard, R. A. 1986, *Astrophys. J.*, **308**, 110.

Mihara, T., Makishima, K., Ohashi, T., Sakao, T., Tashiro, M., Nagase, F., Tanaka, Y., Kitamoto, S., Miyamoto, S., Deeter, J. E. and Boynton, P. E. 1990, *Nature*, **346**, 250.,

Mitsuda, K., Inoue, H., Koyama, K., Makishima, K., Matsuoka, M. Ogawara, Y., Shibazaki, N., Suzuki, K., Tanaka, Y. and Hirano, T. 1984, *Publ. Astron. Soc. Japan*, **36**, 741.

Mitsuda, K., Inoue, H., Nakamura, N. and Tanaka, Y. 1989, *Publ. Astron. Soc. Japan*, **41**, 97.

Mitsuda, K. and Tanaka, Y. 1985, in *The evolution of Galactic X-ray Binaries*, ed. J. Trümper, W. H. G. Lewin and W. Brinkmann, NATO ASI Series C, vol./ 167, D. Reidel, p.195.

Miyamoto, S. and Kitamoto, S. 1989, *Nature*, **342**, 773.

Miyamoto, S., Kitamoto, S. and Kimura, K. 1989, *Proc. 23rd ESLAB Symp. on two topics in X-ray astronomy*, vol.1,p.531, ESA.

Morrison, R. and McCammon, D. 1983, *Astrophys. J.*, **270**, 119.

Motch, C., Ilovaisky, S. A. and Chevalier, C. 1982, *Astron. Astrophys.*, **109**, L1.

Motch, C., Ricketts, M. J., Page, C. G., Ilovaisky, S. A. and Chevalier, C. 1983, *Astron. Astrophys.*, **119**, 171.

Nagase, F. 1989, *Publ. Astron. Soc. Japan*, **41**, 1.

Nagase, F., Dotani, T., Makishima, K., Mihara, T., Sakao, T., Tsunemi, H., Kitamoto, S., Yoshida, A. and Nakamura, H. 1991, *Astrophys. J.*, submitted.

Nishimura, J., Mitsuda, K. and Itoh, M. 1986, *Publ. Astron. Soc. Japan*, **38**, 819.

Nolan, P. L. and Matteson, J. L. 1983, *Astrophys. J.*, **265**, 389.

Novikov, I. D. and Thorne, K. S. 1973, in *Black Holes*, p. 343, ed. C.DeWitt and B. S. DeWitt, Gordon and Breach, New York.

Oda, M. 1977, *Space Sci. Rev.* , **20**, 757.

Oda, M., Doi, K., Ogawara, K., Takagishi, K. and Wada, M. 1976, *Astrophys. Space Sci.* , **42**, 223.

Oda, M., Gorenstein, P., Gursky, H., Kellogg, E., Schreier, E., Tananbaum, H. and Giacconi, R. 1971, *Astrophys. J. Lett.*, **166**, L1.

Ohashi, T., Inoue, H., Koyama, K., Makishima, K., Matsuoka, M., Murakami, M., Oda, M., Ogawara, Y., Shibazaki, N., Tanaka, Y., Kondo, I., Hayakawa, S., Kunieda, H., Makino, F., Masai, K., Nagase, F., Tanaka, Y., Miyamoto, S., Tsunemi, H. and Yamashita, K. 1982, *Astrophys. J.*, **258**, 254.

Oke, J. B. 1977, *Astrophys. J.*, **217**, 181.

Okamura, S. and Noguchi, T. 1988, *IAU circ.*, No.4606.

Oppenheimer, J. R. and Volkoff, G. M. 1939, *Phys. Rev.*, **55**, 374.

Paczyński, S. 1974, *Astron. Astrophys.*, **34**, 161.

Paczyński, B. 1983, *Astrophys. J. Lett.*, **273**, L81.

Pakull, M. W. and Angebault, L. P. 1986, *Nature*, **322**, 511.

Pounds, K. A., Nandra, K., Stewart, G. C., George, I. M. and Fabian, A. C. 1990, *Nature*, **344**, 132.

Piro, L., Yamauchi, M. and Matsuoka, M. 1990, *Astrophys. J. Lett.*, **360**, L35.

Pringle, J. E. 1976, *Mon. Not. Roy. Astron. Soc.*, **177**, 65.

Rappaport, S. A. and Joss, P. C. 1983, in *Accretion driven Stellar X-ray Sources*, ed. W. H. G. Lewin and E. P. J. van der Heuvel (Cambridge University Press, Cambridge), p.1.

Rhoades, C. E. and Ruffini, R. 1974, *Phys, Rev. Lett.*, **32**, 324.

Ricketts, M. 1983, *Astron. Astrophys.*, **118**, L3.

Ricketts, M. J., Pounds, K. A. and Turner, M. J. L. 1975, *Nature*, **257**, 657.

Robinson,E. L. 1976, *Ann. Rev. Astron. Astrophys.*, **14**, 119.

Samimi, J., Share, G. H., Wood, K., Yentis, D., Meekins, J., Evans,

W. D., Shulman, S., Byram, E. T., Chubb, T. A. and Friedman, H. 1979, *Nature*, **278**, 434.

Sanford, P. W., Ives, J. C., Burnell, S. J. B. and Mason, K. O. 1975, *Nature*, **256**, 109.

Shakura, N. I. and Sunyaev, R. A. 1973, *Astron. Astrophys.*, **24**, 337.

Shakura, N. I. and Sunyaev, R. A. 1976, *Mon. Not. Roy. Astron. Soc.*, **175**, 613.

Shapiro, S. L., Lightman, A. P. and Eardley, D. M. 1976, *Astrophys. J.*, **204**, 187.

Shibazaki, N. and Hoshi, R. 1975, *Prog. Thor. Phys.* , **54**, 1706.

Shklovskii, I. S. 1967, *Astron. Zhur.*, **44**, 930 (English trans. in *Sov. Astron.-AJ*, **11** 749).

Stella, L, Kahn, S. M. and Grindlay, J. 1984, *Astrophys. J.*, **282**, 713.

Stella, L., White, N. E., Davelaar, J., Parmar, A., Blissett and van der Klis, M. 1985, *Astrophys. J. Lett.*, **288**, L45.

Stothers, R. B. 1983, *Astrophys. J.*, **274**, 20.

Stothers, R. B. 1987, *Astrophys. J.*, **329**, 712.

Sunyaev, R.,Lapshov, I.,Grebenev, S., Efremov, V. V., Kaniovskii, A A., Stepanov, D. K., Yunin, S. N., Gavrilova, E. A., Loznikov, V. M., Prudkoglyad, A. V., Rodin, V. G., Babushkina, O. P., Kiselev, S. V., Kuznetsov, A. V. and Melioranskii, A. S. 1988, *Soviet Astr. Lett.*,**14**, 771.

Sunyaev, R. A. and Titarchuk, L. G. 1980, *Astron. Astrophys.*, **86**, 121.

Sunyaev, R. A. and Trümper, J., 1979, *Nature*, **279**, 506.

Swank, J. H., Becker, R. H., Boldt, E. A., Holt, S. S., Pravdo, S. H. and Serlemitsos, P. J. 1977, *Astrophys. J. Lett.*, **212**, L73.

Tanaka, Y. 1989, *Proc. 23rd ESLAB Symp. on two topics in X-ray astronomy*, vol.1,p.3, ESA.

Tennant, A. F. *et al.* 1986, *Mon. Not. Roy. Astron. Soc.*, **219**, 871.

Thorne, K. S. and Price, R. H. 1975, *Astrophys. J. Lett.*, **195**, L101.

Thorstensen, J. R., Charles, P. A. and Bowyer, S. 1978, *Astrophys. J. Lett.*, **220**, L131.

Treves, A., Belloni, T., Bouchet, P., Falomo, R., Chiappetti, L., Maraschi, L. and Tanzi, E.G. 1988a, *Astrophys. J.*, **335**, 142.

Treves, A., Belloni, T., Chiappetti, L., Maraschi, L., Stella, L., Tanzi, E.G. and van der Klis, M. 1988b, *Astrophys. J.*, **325**, 119.

Treves, A., Belloni, T., Corbet, R. H. D., Ebisawa, K., Falomo, R., Makino, F., Makishima, K., Maraschi, L., Miyamoto, S. and Tanzi, E. G. 1990, *Astrophys. J.*, **364**, 266.

Trümper, J., Pietsch, W., Reppin, C., Voges, W., Staubert, R. and Kendziorra, E. 1978, *Astrophys. J. Lett.*, **219**, L105.

Tsunemi, H., Kitamoto, S., Manabe, M., Miyamoto, S. and Yamashita, K. 1989a, *Publ. Astron. Soc. Japan*, **41**, 391.

Tsunemi, H., Kitamoto, S., Okamura, S. and D. Roussel-Dupré 1989b, *Astrophys. J. Lett.*, **337**, L81.

Turner, M. J. L., Thomas, H. D., Patchett, B. E., Reading, D. H., Makishima, K., Ohashi, T., Dotani, T., Hayashida, K., Inoue, H., Kondo, H., Koyama, K., Mitsuda, K., Ogawara, Y., Takano, S., Awaki, H., Tawara, Y. and Nakamura, N. 1989, *Publ. Astron. Soc. Japan*, **41**, 345.

van der Klis, M. 1989, *Ann. Rev. Astron. Astrophys.*, **27**, 517.

van Paradijs, J. 1978, *Astrophys. J.*, **274**, 650.

van Paradijs, J., Joss, P. C., Cominsky, L. and Lewin, W. H. G. 1979, *Nature*, **280**, 375.

van Paradijs, J., Verbunt, F., van der Linden T., Pedersen, H. and Wamstecker, W. 1980, *Astrophys. J. Lett.*, **241**, L161.

Webster, B. L. and Murdin, P. 1972, *Nature*, **235**, 37.

Wheaton, W. A., Doty, J. P., Primini, F. A., Cooke, B. A., Dobson, B. A., Goldman, A., Hecht, M., Hoffman, J. A., Howe, S. K., Scheepmaker, A., Tsiang, E. Y., Lewin, W. H. G., Matteson, J. L., Gruber, D. E., Baity, W. A., Rothschild, R., Knight, F. K., Nolan, P. and Peterson, L. E. 1979, *Nature*, **282**, 240.

Whelan, J. A. J., Mayo, S. K., Wickramasinghe, D. T., Murdin, P. G., Peterson, B, A., Hawarden, T. G., Longmore, A. J., Haynes, R. F., Goss, W. M., Simons, L. W., Caswell, J. L., Little, A. G. and

McAdam, W. B. 1977, *Mon. Not. Roy. Astron. Soc.*, **181**, 259.

White, N. E., Kaluzienski, J. L. and Swank, J. H. 1984, in *High Energy Transients in Astrophysics* (AIP Conference Proceedings No.115), p.31, ed. S. E. Woosley (New York:AIP)

White, N. E. and Marshall F. E. 1984, *Astrophys. J.*, **281**, 354.

White, N. E., Peacock, A., Hasinger, G., Mason, K. O., Manzo, G., Taylor, B. G. and Branduardi-Raymont, G. 1986, *Mon. Not. Roy. Astron. Soc.*, **218**, 129.

White, N. E., Peacock, A. and Taylor, B. G. 1985, *Astrophys. J.*, **296**, 475.

White, N. E., Stella, L. and Parmar, A. N. 1988, *Astrophys. J.*, **324**, 363.

Acknowledgement

I am grateful to Prof. F. Makino for his continuous guidance and encouragement throughout the five years of my career in this field. I have respect for his important role in the development of X-ray astronomy as the chief manager of the *Ginga* satellite. I also thank Prof. Y. Tanaka for helpful discussions. His boundless enthusiasm toward a black hole has been a source of constant inspiration to me. Stimulating discussions with Prof. H. Inoue are gratefully acknowledged. I wish to thank to Dr. K. Mitsuda for his valuable advice in data analysis and interpretation of the results. He also made invaluable comments on the early manuscipt of the thesis. I am grateful for many interesting discussions with Prof. R. Hoshi, Prof. N. Shibazaki and Prof. K. Makishima.

I wish to thank Dr. T. Hanawa for supplying the code of General Relativistic Accretion Disk model.

I am much indebted to Prof. S. Miyamoto for allowing me to use GX339-4 data and to Prof. A. Treves and Prof. A. P. Cowley for allowing me to use LMC X-3 data.

Thanks are due to Dr. T. Belloni for helping with analysis of LMC X-3 during his stay in ISAS. I thank students in ISAS for helping with data analysis; Mr. M. Takizawa, Mr. K. Yoshida and Mr. T. Aoki.

I would like to acknowledge Dr. T. Yaqoob for carefully reading the manuscript and critical comments.

Routine operations of *Ginga* are mainly made by graduate students in the X-ray group. I would like to thank them all for their labour in the operations as well as for the enjoyable time I have had in ISAS.

Finally I would like to express my hearty thanks to my wife Mika Miyawaki for her continuous support, encouragement and understanding.